

T-3716

**Four-Component Rotation of
3-D Shear Wave Data,
Silo Field, Wyoming**

by

Michael L. Gurch

T-3716

A thesis submitted to the Faculty and the Board of Trustees of the Colorado School of Mines in partial fulfillment of the requirements for the degree of Master of Science (Geophysics).

Golden, Colorado

Date 3/28/89

Signed: Michael L. Gurch
Michael L. Gurch

Approved: Thomas L. Davis
Thomas L. Davis
Thesis Advisor

Golden, Colorado

Date 29 March 1989

Phillip R. Romig
Phillip R. Romig,
Head, Department of
Geophysics

ABSTRACT

A 3-D shear wave survey was acquired over a two-square-mile area of the Silo Field in Wyoming. Two orthogonal source and receiver orientations (x- and y-components) enabled a four-component rotation analysis of these data. A statistical energy minimization algorithm derived by Murtha (1988) was applied to the four recorded shear wave components to determine the principal polarization directions of the fast (S1) and slow (S2) split shear waves. The S1 polarization direction is parallel to the strike of subsurface vertical fractures; the S2 polarization direction is orthogonal to the fracture strike. Results indicated that the S1 and S2 polarization directions, within the 3-D survey area, are N 58° W and N 32° E, respectively. Once the S1 and S2 polarization directions were determined, the shear wave data were rotated into the (S1, S2) coordinate system wherein the S1 and S2 split shear waves become distinct, interpretable events.

The effect of random noise, different x- and y-component source radiation patterns, or different x- and y-component geophone coupling on four-component rotation analysis is minimal. However, groundroll and other coherent noise can significantly influence rotation analysis. An advantage of recording 3-D shear wave data is the different source-receiver azimuths recorded. Sorting of selected azimuth "pie-slices" permits the selection of those azimuths with low groundroll content as input to the four-component rotation analysis.

TABLE OF CONTENTS

ABSTRACT	iii
LIST OF FIGURES	vi
LIST OF TABLES	ix
ACKNOWLEDGEMENTS	x
INTRODUCTION	1
PREVIOUS WORK	6
GEOLOGY	9
DATA ACQUISITION	14
DATA PROCESSING	20
ROTATION ANALYSIS	26
Four-Component rotation	26
Analysis of Silo Field synthetic data	30
Analysis of Silo Field data	57
FUTURE WORK	83
CONCLUSIONS	85
REFERENCES CITED	87
APPENDIX A: Derivation of Energy Minimization Algorithm	89
APPENDIX B: Rotation Analysis Results	92

T-3716

APPENDIX C: Program Listings 98

LIST OF FIGURES

1.)	Shear-wave splitting	2
2.)	Polarization patterns for transversely isotropic media	3
3.)	Survey location map	10
4.)	Stratigraphic section	11
5.)	Niobrara isopach map	12
6.)	Fracture orientation and frequency	13
7.)	3-D shear wave survey layout	15
8.)	Geophone array	16
9.)	Source array	17
10.)	Vertically stacked V.P.	22
11.)	CDP stack with residual statics	24
12.)	Rotation into the natural coordinate system	27
13.)	Recording line geometry for Silo Field modelling	32
14.)	Shot profiles for 36 degree azimuth with agc	34
15.)	Shot profiles for 36 degree azimuth with t cubed gain	35
16.)	Windowed 36 degree azimuth data	36
17.)	Rotated 36 degree azimuth data	37
18.)	Shot profiles for 306 degree azimuth with agc	38

19.) Shot profiles for 306 degree azimuth with t cubed gain	39
20.) Windowed 306 degree azimuth data	40
21.) Rotated 306 degree azimuth data	41
22.) Polarization pattern for orthorhombic anisotropy	43
23.) Zero-offset data with t squared gain	45
24.) Unrotated data with signal-to-noise ratio of 6	46
25.) Rotated data with signal-to-noise ratio of 6	47
26.) Unrotated data with signal-to-noise ratio of 3	48
27.) Rotated data with signal-to-noise ratio of 3	49
28.) Unrotated data with signal-to-noise ratio of 2	50
29.) Rotated data with signal-to-noise ratio of 2	51
30.) Energy ratio curves for noisy synthetic data	54
31.) Rotation angle errors	56
32.) Sectors for geophone azimuth stacks	58
33.) yy-component rotations for sector 3 of line 6	60
34.) Vertical stacks of xx-component rotations for line 6	61
35.) Vertical stacks of yy-component rotations for line 6	62
36.) Vertical stacks of xy-component rotations for line 6	63
37.) Vertical stacks of yx-component rotations for line 6	64

38.) S1 polarization plots for Kp using total energy minimization algorithm	67
39.) S1 polarization plots for Kp using trace-by-trace energy minimization algorithm	68
40.) S1 polarization plots for Kn using trace-by-trace energy minimization algorithm	70
41.) Unrotated geophone azimuth stacks for line 4	71
42.) Rotated geophone azimuth stacks for line 4	72
43.) Unrotated geophone azimuth stacks for line 5	73
44.) Rotated geophone azimuth stacks for line 5	74
45.) Unrotated geophone azimuth stacks for line 6	75
46.) Rotated geophone azimuth stacks for line 6	76
47.) Energy ratio curves for line 6	77
48.) Hodograms for line 4	79
49.) More Hodograms for line 4	80
50.) S1- and S2-component CDP stacks	82

LIST OF TABLES

1.)	Acquisition Parameters	19
2.)	Source-Receiver Configurations	23
3.)	Preliminary Processing Steps	25
4.)	Silo Field Eight Layer Offset Model	31
5.)	Silo Field Eight Layer Zero-Offset Model	44
6.)	Rotation Analysis Results for Noisy Data	52

ACKNOWLEDGEMENTS

I would like to thank my advisor, Dr. Thomas L. Davis, for his invaluable guidance. I also thank the other members of my committee: Dr. Walter Whitman, Dr. Alfred Balch, and Mr. Claude Vuillermoz. They each contributed greatly to my education at Mines and to my research.

I would also like to thank Sebastian Geoltrain, Norman Bleistein, Jack Cohen, John Stockwell, and the other staff at Center for Wave Phenomena (CWP) for their guidance and computer support. I used the SU (Seismic Unix) Processing System at CWP for the processing of the synthetic data in this thesis.

Many companies helped support my graduate studies at Mines. Their generous support is greatly appreciated. Mobil and Amoco both provided scholarships. CGG personnel assisted me greatly by providing me with both data and guidance. I would particularly like to thank Bill Bailey and Don Chitwood for their support. In addition, I would also like to thank the other companies involved with the Reservoir Characterization Project. Patricia Murtha of ARCO and Dale Cox of Conoco both provided excellent technical advice. Also, Mark Brown and Don Loomis of Union Pacific Resources were very supportive of my research while I worked there as a summer hire.

In addition, I would like to thank Anne Marie Butler of AMB, Ink for her high quality drafting work.

T-3716

Finally, I would like to express my deep appreciation to my parents, Michael Gurch and Ellen Johnson, and to Phyllis Gurch.

INTRODUCTION

Recently, geophysicists have a renewed interest in seismic shear wave exploration because shear waves provide information on the location, orientation, and density of fractures in reservoir rock (Martin and Davis, 1987). For example, vertically or nearly vertically propagating shear waves, incident upon a vertically fractured rock, decompose vectorially into components which are parallel and perpendicular to the strike of the fractures (Figure 1). The parallel component, S1, travels with a velocity equal to that of the uncracked rock. The perpendicular component, S2, travels with a slower velocity because cracked rocks are less rigid in the S2 direction. Multiple splitting of the S1 and S2 modes will occur if the fracture strike changes with depth. Traveltime and amplitude differences between the S1 and S2 modes can be used to map the orientation and density of fractures.

Vertically fractured rock is transversely isotropic with a horizontal axis of hexagonal symmetry. Laminated rock sequences are transversely isotropic with a vertical axis of hexagonal symmetry. Stuart Crampin (1988) modelled the anisotropy effects of both vertical fractures and horizontal laminations as a function of source-receiver azimuth and offset. Figure 2 is a plan view of the projections, onto a hemisphere, of the faster S1 shear wave polarization directions, for both east-west striking vertical fractures and horizontal laminations. The radial direction on these polarization plots corresponds to angle of incidence; the polar

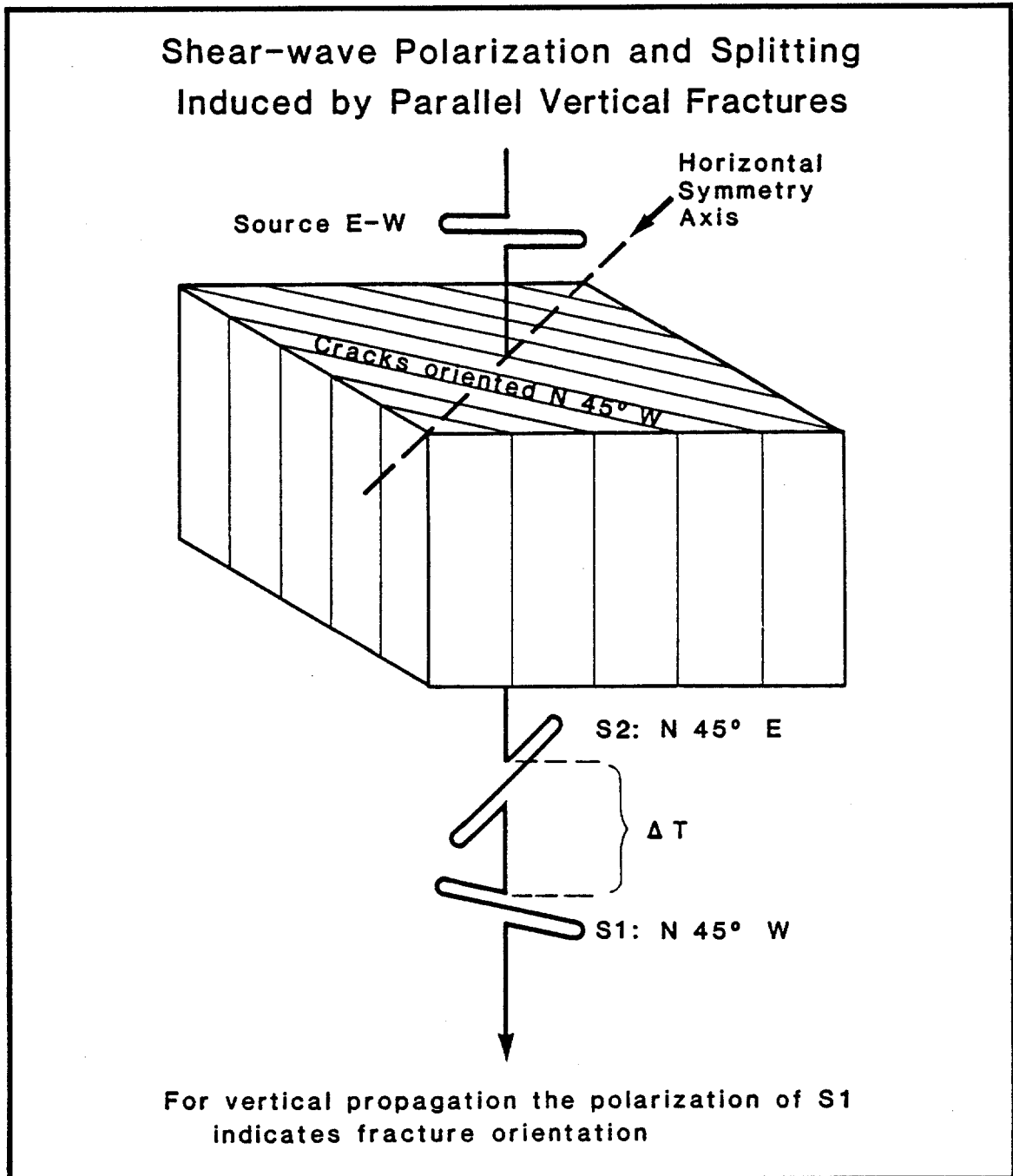


Figure 1. Shear-wave splitting (modified from Martin, 1987, after Naville, 1986 and Crampin).

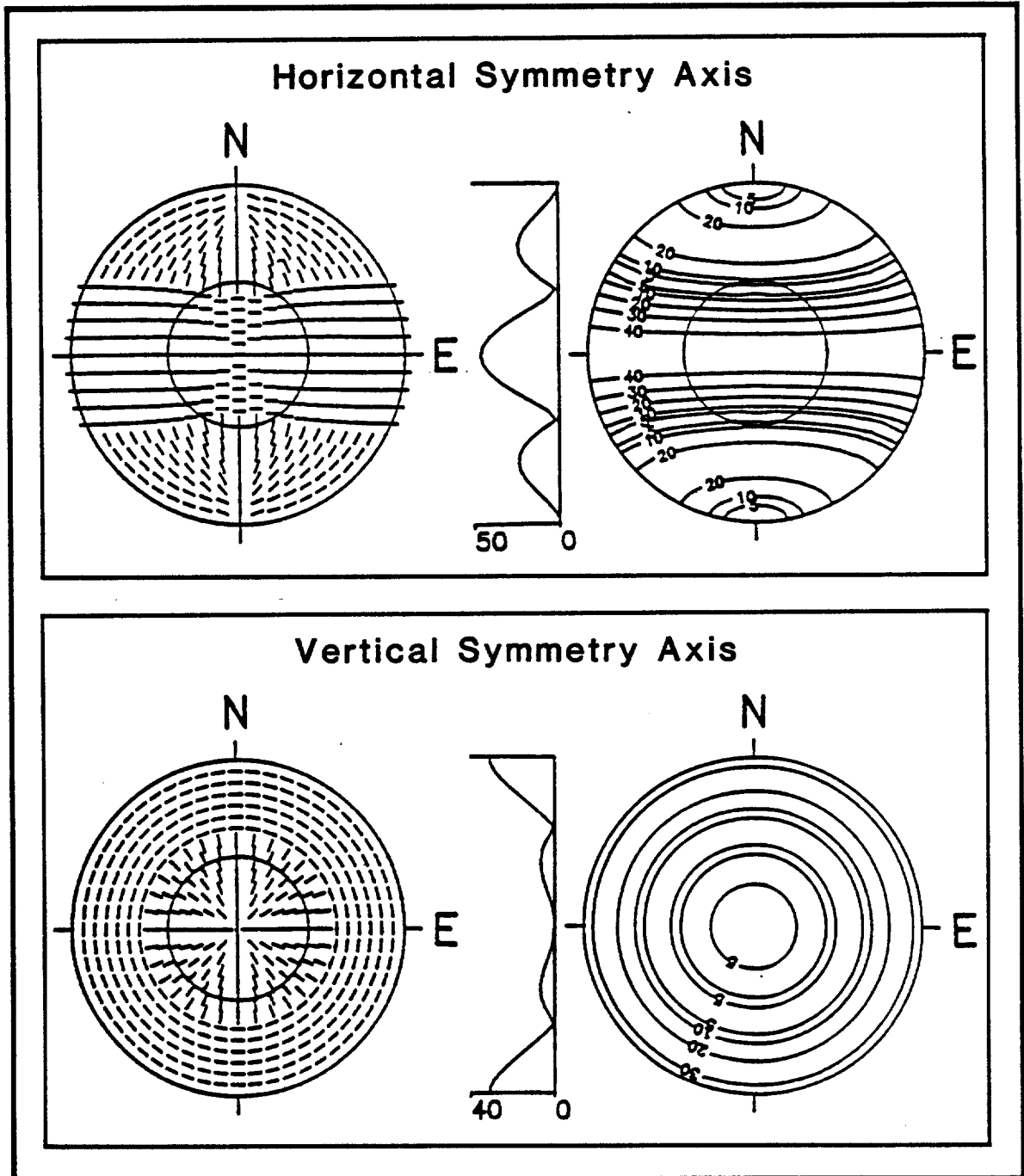


Figure 2. Plan view of the projection onto a hemisphere of the fast shear wave polarization direction, for transversely isotropic media. Also shown are the contoured time delays (msec.) between the fast and slow polarization modes. The inner circles correspond to the shear wave window (from Crampin, 1988).

direction corresponds to the source-receiver azimuth.

One of the objectives of the Colorado School of Mines Silo II Reservoir Characterization Project is to characterize reservoir heterogeneity by the 3-D imaging of shear waves. In December, 1987, compressional, shear, and converted wave 3-D surveys were recorded over a two-square-mile area of the Silo Field in Wyoming. Three Colorado School of Mines graduate students are analyzing the data. Catherine Lewis is interpreting the 3-D data sets. Peter Schipperijn is applying a 1-D inversion algorithm to the shear wave data. My own involvement with the project centers on the rotation analysis of the shear wave data.

If shear wave data recorded over a transversely isotropic medium is not recorded along the principal axes of the fractures (S1 and S2 polarization directions), the S1 and S2 modes will interfere with each other. This interference will make an interpretation of the S1 and S2 traveltime and amplitude differences difficult, if not impossible. Therefore a rotation analysis must be performed to determine the S1 and S2 polarization directions. Once these directions are determined, the recorded shear wave data can be rotated into the (S1, S2) or natural coordinate system. The S1 and S2 modes are distinct, interpretable events only in the natural, or principal axes, coordinate system.

In order to determine the orientation of the principle axes I applied a statistical algorithm to different time-space windows of the shear wave data.

Additionally, I investigated the effects of noise, different x- and y-component source radiation patterns, and different x- and y-component geophone coupling, on the rotation analysis.

PREVIOUS WORK

The theory for the propagation of shear waves in elastic, anisotropic media has been discussed by Love (1944), Stoneley (1949), and White et al (1955). However, the application of this theory to the mapping of fractures in transversely isotropic media didn't occur until Crampin (1978, 1985) modelled shear wave propagation in fractured media. Crampin used particle displacement diagrams (hodograms) to determine polarization directions.

To determine if the surface seismic recording of shear waves can be used to identify fractures, in the subsurface at 8000 feet in Silo Field, Wyoming, the Colorado School of Mines acquired five miles of three-component seismic data. The survey was conducted in September, 1985, using both P- and SH- wave vibrator sources. Martin et al (1986), Martin and Davis (1987), and Martin (1987) showed that shear waves recorded along this seismic line can be used to calculate average anisotropy and map subsurface fractures.

The Colorado School of Mines also acquired a three-component P- and SH- wave VSP in Silo Field. However, because the SH- wave vibrator source was aligned parallel to the S2 axis, no shear wave splitting was detected.

At the 1986 SEG Convention, Thomsen (1986), Lynn and Thomsen (1986), Alford (1986), and Willis et al (1986) all demonstrated that the analysis of surface-recorded shear wave data can be used to map subsurface fractures.

Lynn and Thomsen (1986) interpreted two intersecting SH- shear wave lines recorded in the natural coordinate system of a sandstone reservoir with north-south striking fractures. Lynn and Thomsen observed that where the fracturing is locally intense, the S2 wave has a lower amplitude than the S1 wave. This amplitude difference results because the impedance contrast in the S2 direction (between the reservoir sandstone and overlying shale roof rock) is reduced by the fractures. The impedance contrast in the S1 direction is not affected by the fractures.

Willis et al (1986) studied the recording of numerous multi-component shear wave surveys in the western United States. The source and receiver orientations were varied in 30 degree increments, from 0 to 150 degrees. From these data, Willis et al were able to determine the principle polarization directions, S1 and S2, of the split shear waves. They concluded that anisotropy in sedimentary rocks is very common.

Alford (1986) successfully implemented a four-component rotation of multi-component shear wave data recorded near Diley, Texas. Four shear wave data sets were recorded, corresponding to the four possible parallel and orthogonal combinations of source and receiver orientation. These data sets were rotated into the natural coordinate system by visually minimizing the energy of the cross-component data sets.

Murtha (1988) developed an algorithm for calculating the angle needed to rotate four-component shear wave data into the natural coordinate system. Murtha derived this algorithm by minimizing the energy of the cross-component data sets over some window in time and space. I applied a program implementing Murtha's algorithm to the Silo Field shear wave data to find the S1 and S2 polarization directions.

Garotta and Granger (1988) applied a two-component rotation to the Silo Field 3-D converted wave data. They rotated the unstacked data into radial and transverse coordinates and looked at the ratio of radial energy to transverse energy, for each of eight source-receiver azimuths. This ratio should theoretically be maximized in the natural coordinate system.

GEOLOGY

The location of the Silo II 3-D seismic survey is shown in Figure 3. The 3-D grid area covers a little over two square miles in sections 29, 30, 31, and 32 of T16N-R64W, Laramie County, Wyoming. The Silo Field is situated within the northern Denver basin. Production in Silo Field is from fractured chalks in the Smoky Hill member of the Niobrara Formation (Figure 4). Martin (1987) indicated that open fractures oriented northwest-southeast control production. These fractures probably resulted from folding over a salt solution edge. A Niobrara isopach map, which supports the theory of basement vertical faulting, is shown in Figure 5.

Evidence for the existence of these northwest-southeast fractures is shown in Figure 6. Iverson (1988) has plotted the fracture azimuths for the Combs #1 well and 24 other wells in the Silo Field. He used fracture identification logs (FIL) and oriented micro-resistivity logs (OMRL) to calculate these fracture azimuth plots for the Niobrara Formation and deeper rocks. He indicated that most of the fracture azimuths ranged from N 60° W to N 20° W.

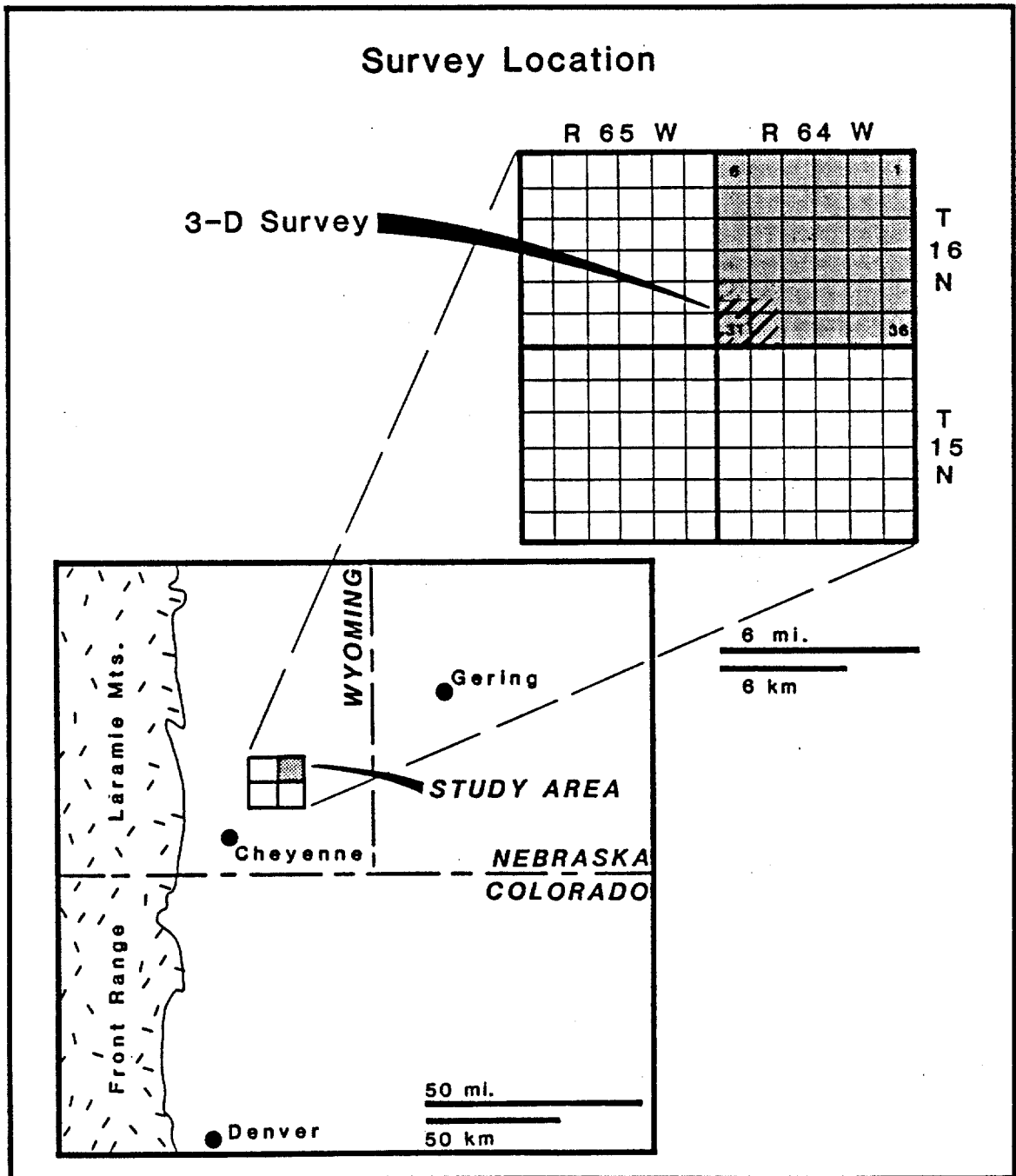


Figure 3. Location of 3-D survey.

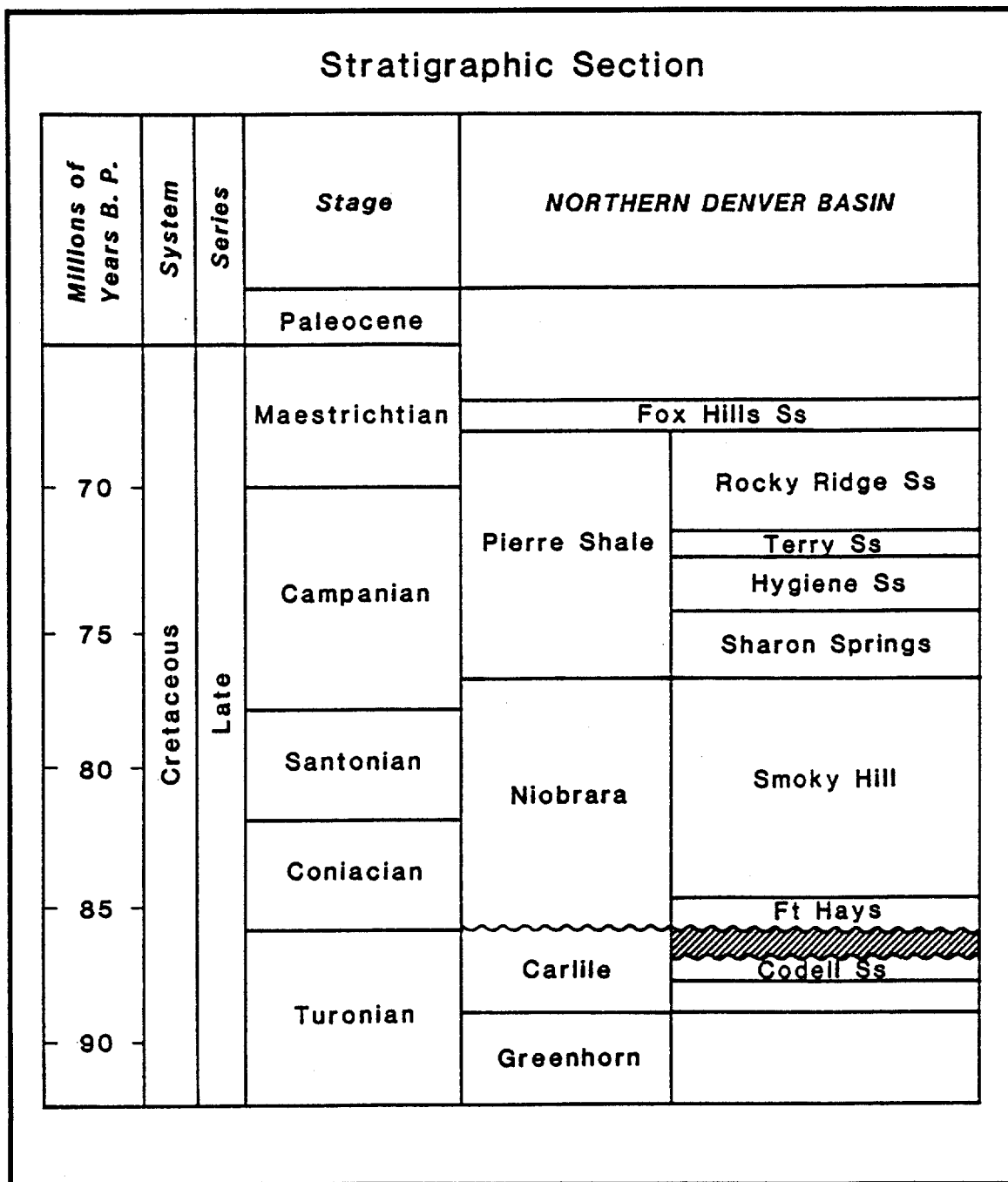


Figure 4. Stratigraphic section for northern Denver Basin (from Martin, 1987).

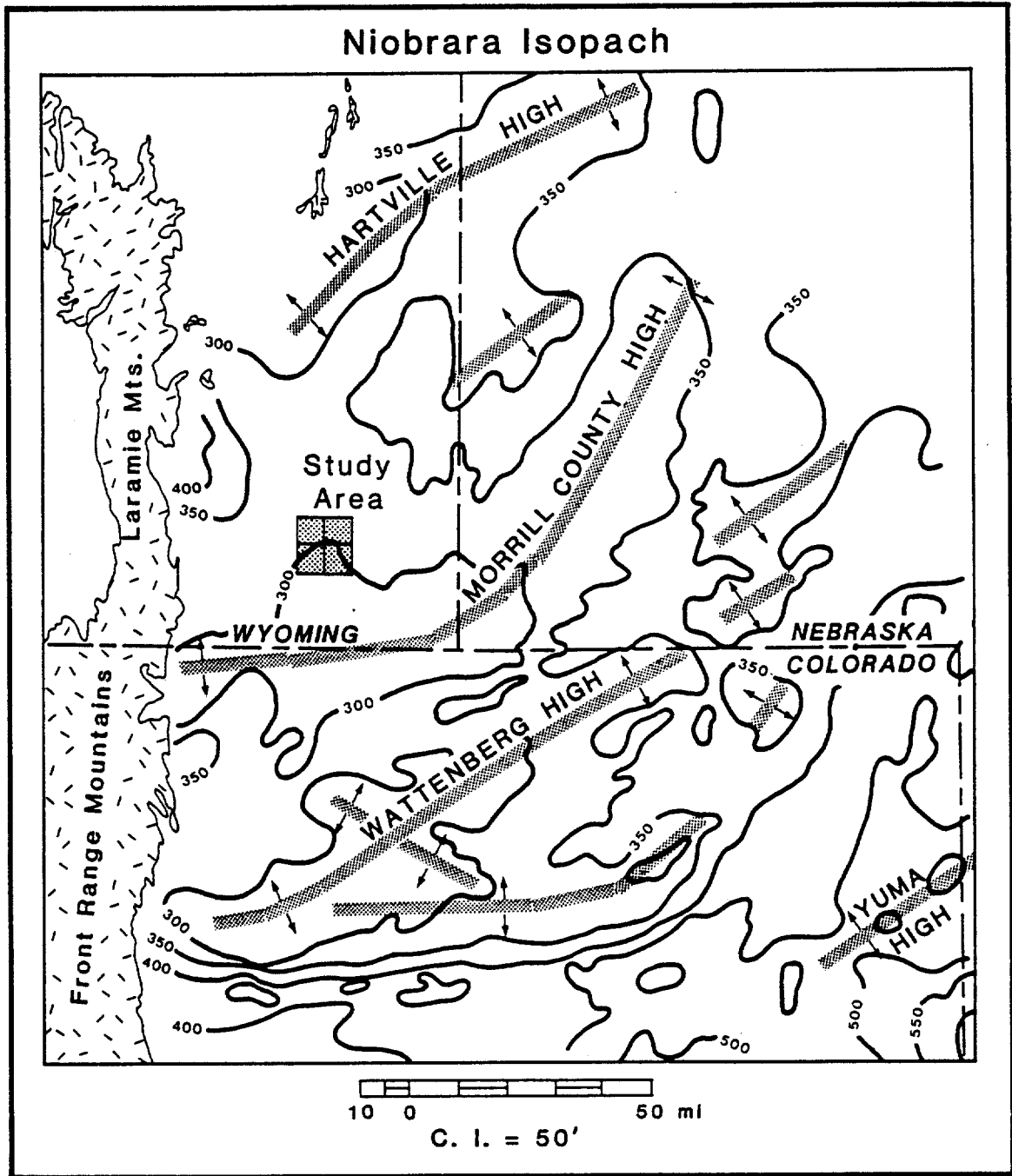


Figure 5. Regional Niobrara isopach map. This map supports the theory of basement vertical faulting (from Martin, 1987).

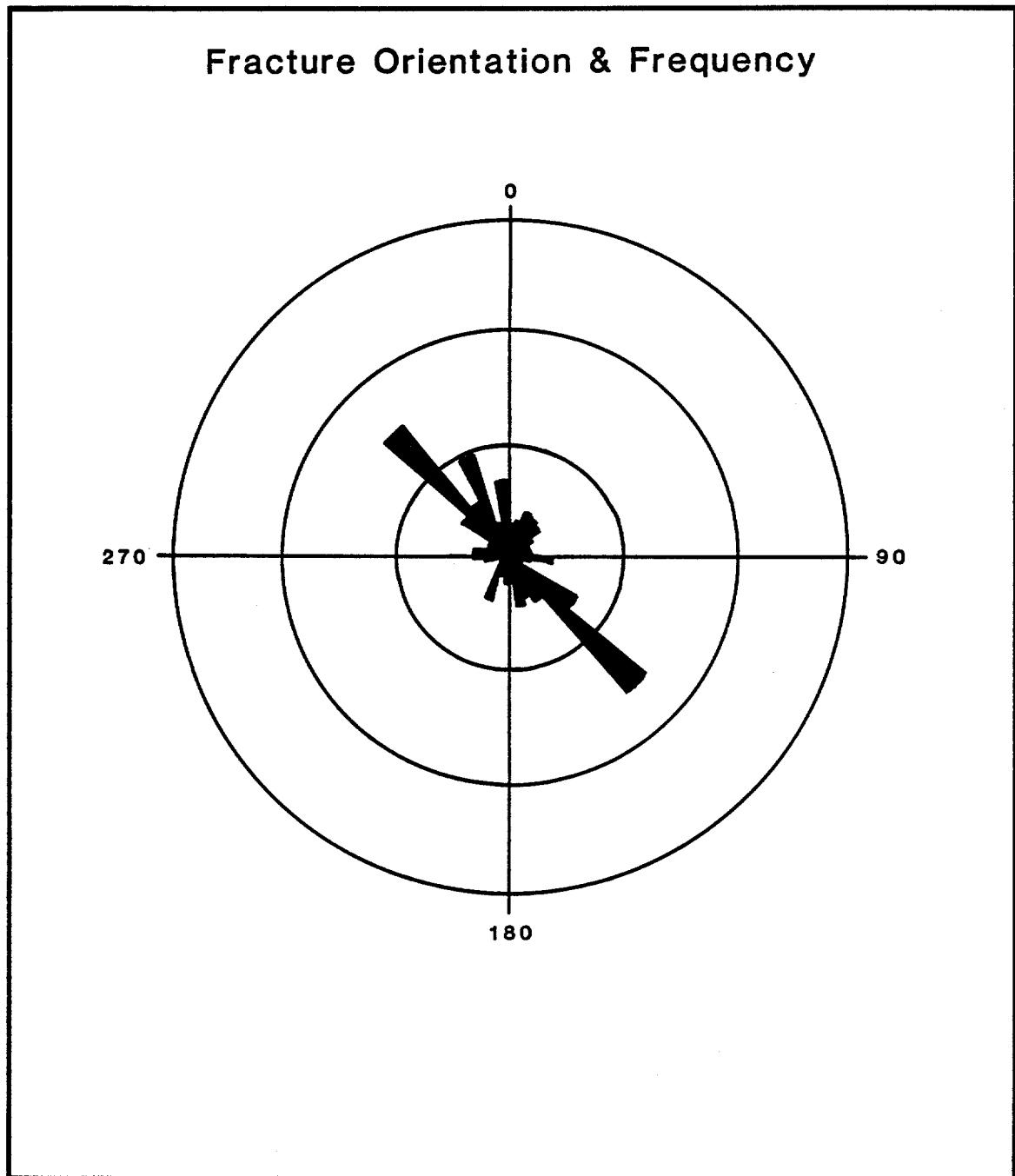


Figure 6. Combs #1 fracture orientation and frequency for depths from 8175 to 8520 feet. Frequency ranges from zero in the center to 300 at the edge. Divide frequency by 10 for fractured footage (modified from Iverson, 1988).

DATA ACQUISITION

The Silo II 3-D shear wave data were acquired by CGG American Services, Inc. from December 23, 1987 to January 3, 1988. The field layout of the survey is shown in Figure 7. There were eight receiver lines, each with 30 geophone groups. Each geophone group consisted of nine x- and y-component geophones spread out over 165 feet in an east-west direction (Figure 8). The x-component geophones had positive polarity to the east; the y-component geophones had positive polarity to the north. The geophone group interval was 330 feet (Vuillermoz et al, 1988).

The vibrator source configuration consisted of 11 north-south columns of approximately 42 vibrator points (east-west pad movement) and 21 east-west rows with approximately 22 vibrator points each (north-south pad movement). These columns and rows of VP's (vibrator points) formed diamond-shaped source arrays. Each source array consisted of four subarrays, as shown in Figure 9. The subarrays at the north and south vertices of the diamond pattern consisted of two or three vibrators travelling from north to south, spaced 165 feet linearly, without moveup. These x-component vibrators shook in an east-west direction.

The subarrays at the west and east vertices of the diamond pattern consisted of two or three vibrators, travelling from west to east, spaced 165 feet abreast. These y-component vibrators shook in a north-south direction.

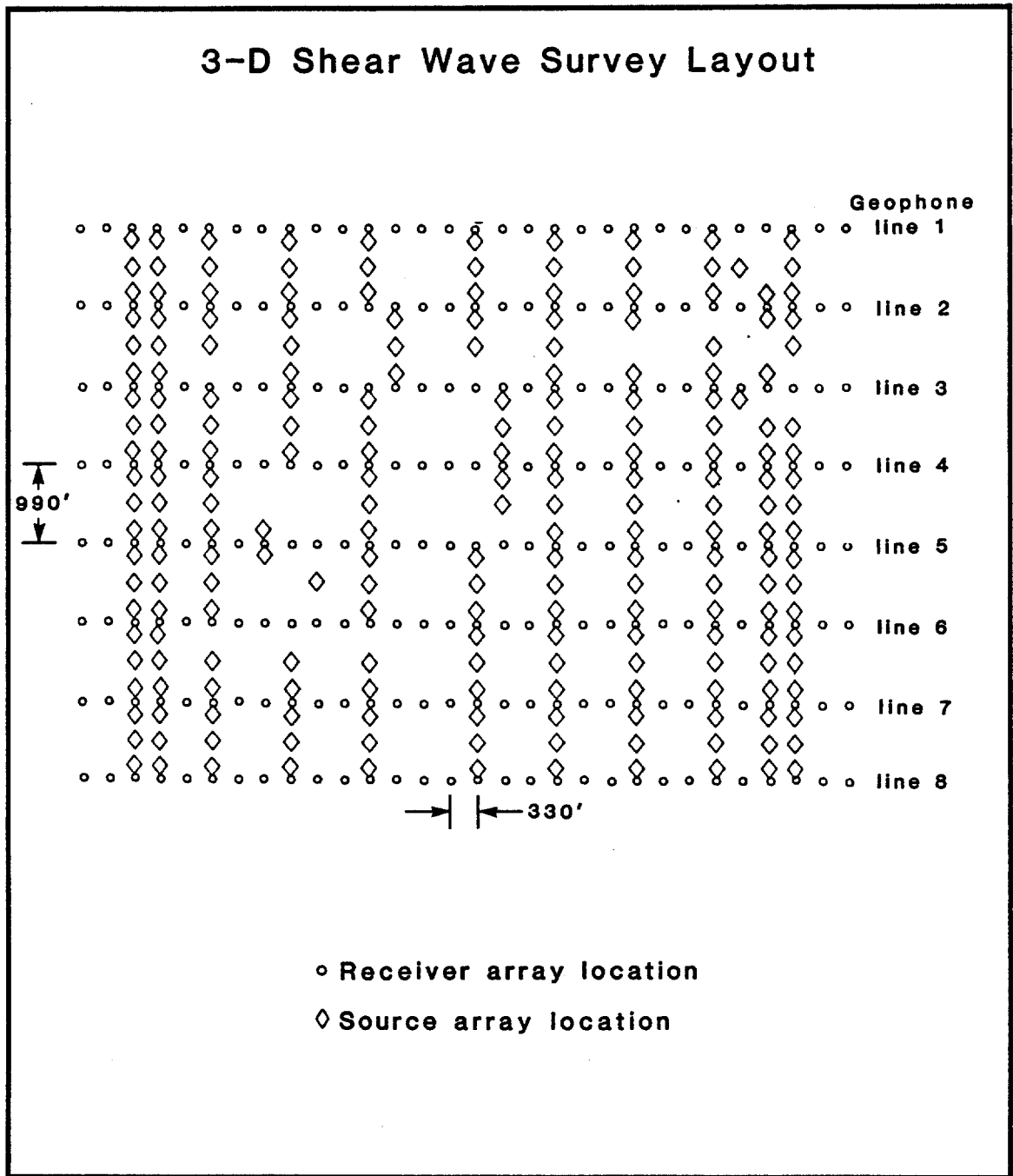


Figure 7. Location of source and receiver arrays for 3-D shear-shear survey (modified from Lewis, 1988).

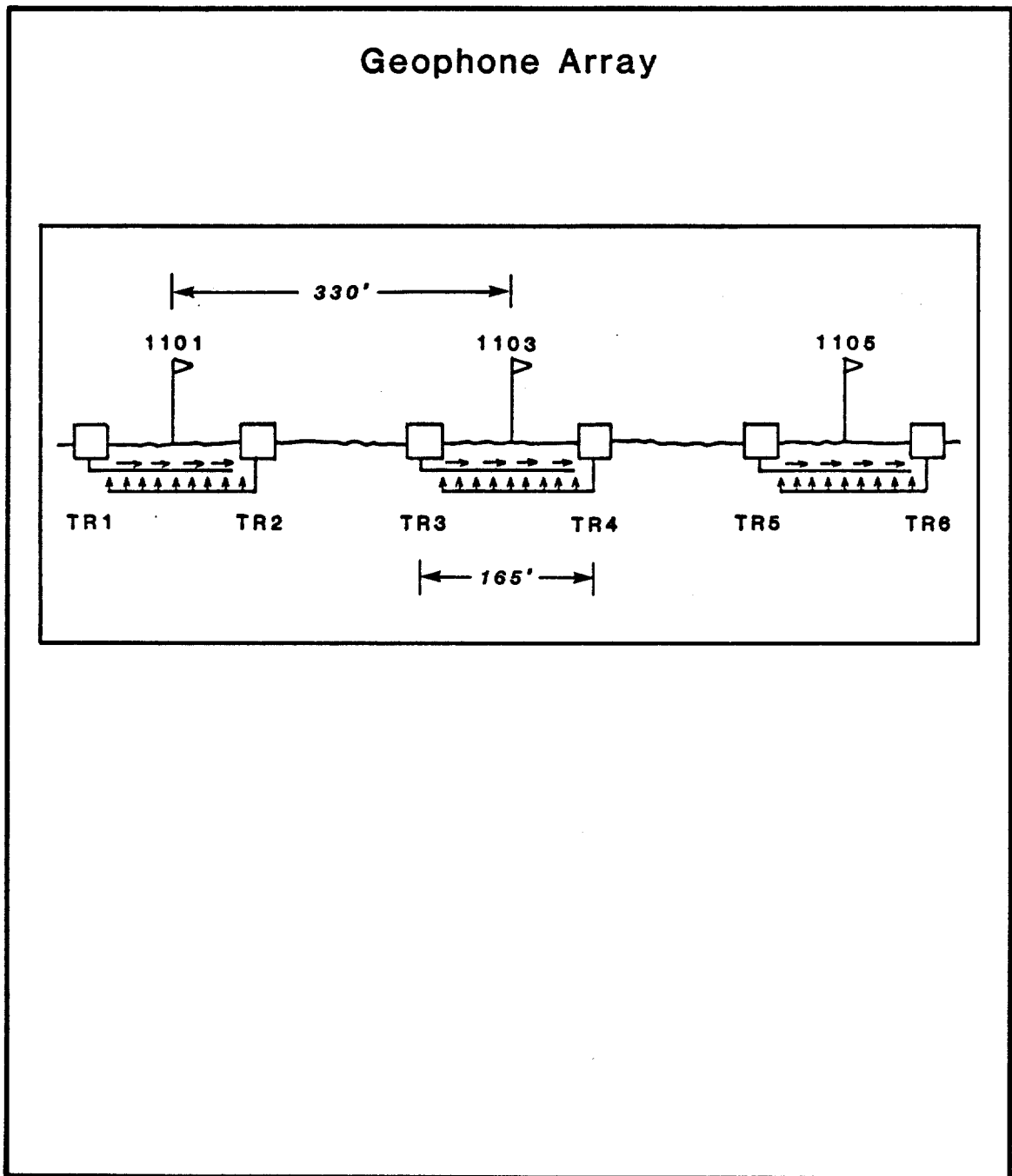


Figure 8. Cross-section view of shear wave geophone array. The arrows point in the direction of positive polarity for the x- and y-component geophones (modified from Vuillermoz et al, 1988).

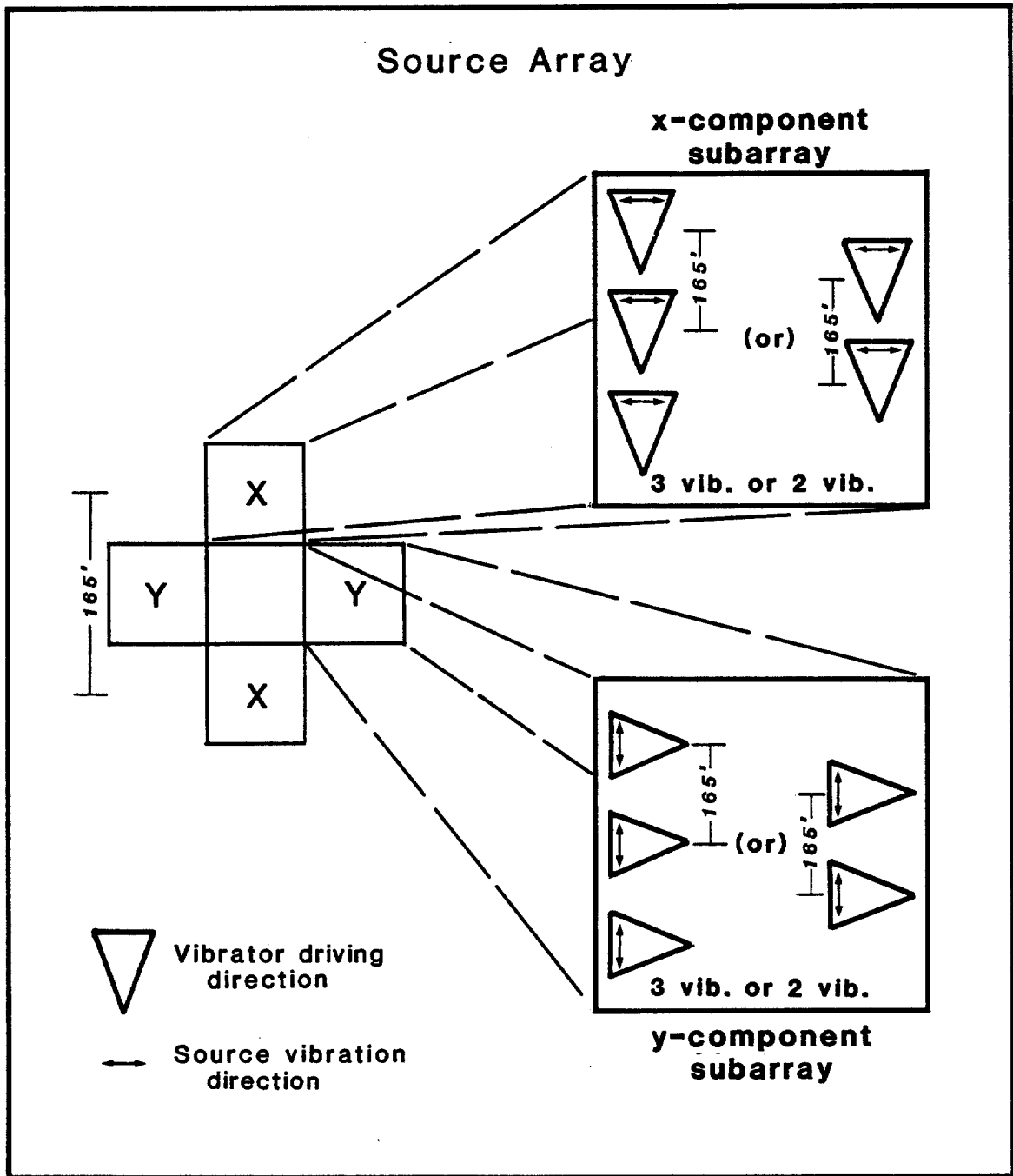


Figure 9. Vibrators travelled from north to south for east-west pad movement; from west to east for north-south pad movement. The subarrays consisted of 2 or 3 vibrators as shown.

The 165 foot VP interval was designed to avoid aliasing. Later, in the processing center, the two x-component subarrays were vertically stacked to the center of the diamond pattern. In a like manner, the two y-component subarrays were vertically stacked.

Because of their geometry, the source arrays tended to attenuate ground roll along a north-south azimuth; whereas, the receiver arrays tended to attenuate ground roll along an east-west azimuth. A list of the field recording parameters is contained in Table 1.

The CDP bin size, after vertical stacking of the x- and y-source subarrays, is 165 feet by 165 feet. There are 42 CDP lines with 55 CDP's per line. The stacking fold varies from one to 60; the mean fold is 44. The source-receiver offset varies from 82.5 feet to 12,320 feet.

Table 1 (modified from Vuillermoz et al, 1988)

ACQUISITION PARAMETERS	
Inline group interval	330'
Receiver line interval	990'
VP within column interval	165'
VP within row interval	165'
Recorder	Sercel SN 348
Number of channels	480, 8 lines of 30 groups of east-west receivers and 30 groups of north-south receivers
Sample rate	4 msec.
Correlator stacker	Sercel CS 2502
Filter	125 Hz, 72 db/octave
Vibrators	3 Mertz Model 13's
Number of sweeps per VP	3 vibrators = 8 sweeps 2 vibrators = 16 sweeps
Sweep frequency	5-40 Hz
Sweep length/record length	8/14 seconds
Sweep type	Linear
Sweep move-up	Stacked
Pad-to-pad spacing	165' - No move up
Receiver type	Geosource L28A, 8 Hz
Receiver damping	50%
Receiver array	9 over 165'
Tape density	6250 bpi

DATA PROCESSING

The 3-D shear wave data were processed by the Denver, Colorado office of CGG American Services, Inc. A total of 969 VP's of 480 traces each were processed on Perkin-Elmer 3230 and Cray 1/M computer systems. The processing began in January, 1988 and the rotation analysis was completed by December, 1988.

After the data were demultiplexed, a database of x-y locations and elevations for surface positions was created. Then a spherical divergence correction was applied using a time exponential function. Elevation statics were applied to the data using a shear wave velocity equal to one-half the compressional wave velocity. In order to maintain relative VP to VP amplitudes, a scaling factor was applied to the data. During recording the field records had been normalized by a factor based on the largest amplitude of each record (Vuillermoz et al, 1988).

The x-component subarray shot records were vertically stacked to the center of the diamond-shaped source arrays. To accomplish this, NMO time shifts were applied, using one velocity function. Then the records to be summed were renumbered with the same record number, sorted, and stacked. New x-y coordinates were assigned to the stacked records, corresponding to the diamond pattern centers. Lastly, the NMO time shifts were removed. The y-component subarray shot records were also vertically stacked in the same way. A vertically

stacked VP is shown in Figure 10.

Table 2 lists the four components (xx, xy, yx, and yy) recorded, corresponding to the different combinations of source and receiver orientation. Velocity analysis was performed on CDP test lines 70, 82, 94, 106, 118, 130, and test cross-lines 75, 105, and 135. Then predictive deconvolution was applied, followed by application of the converted wave statics. CGG processed the converted wave data in France.

After the converted wave statics were applied, residual statics were calculated twice on all four components. Windows of 2.4-3.5 seconds and 3.2-3.3 seconds were used. These residual statics were applied to the undeconvolved data. The resulting stacked xx- and yy-component sections of CDP line 94 are shown in Figure 11.

For rotation analysis the relative amplitude between the four components must be preserved. Therefore, only the undeconvolved data were used for the rotation analysis, since deconvolution affects amplitudes. Table 3 is a list of the processing steps for 3-D, four-component, split shear wave data, from demultiplexing to rotation analysis. Rotation analysis is discussed in the next chapter.

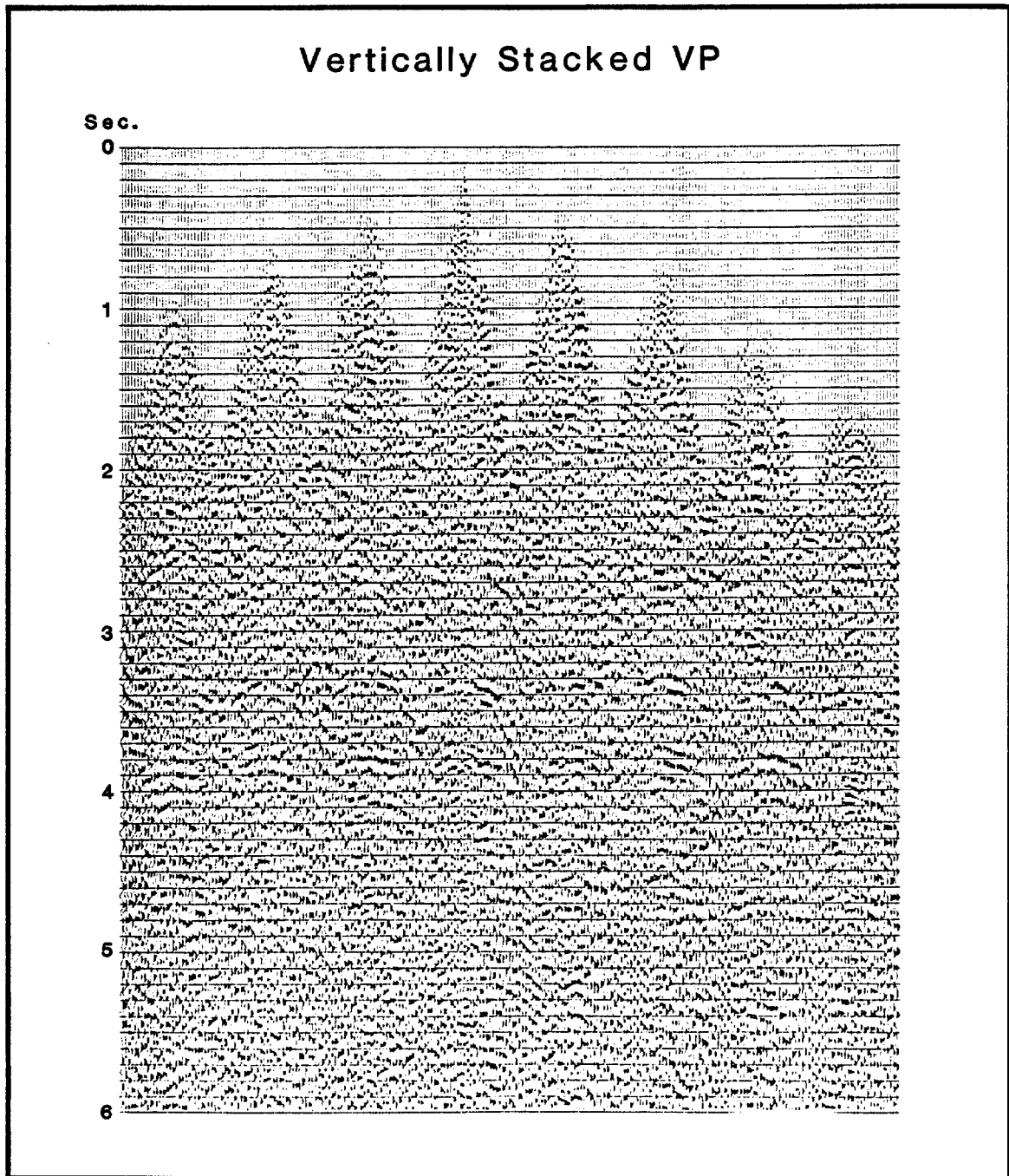


Figure 10. Vertically stacked V.P. with N.M.O. correction removed (from Vuillermoz et al, 1988).

Table 2 (modified from Vuillermoz et al, 1988)

SOURCE-RECEIVER CONFIGURATIONS				
SHOTS	PAD MOVEMENT	TRACE #	GEOPHONE ORIENTATION	COMPONENT
211-1251 Shot N-S	E-W	1-479 Odd	East	xx
211-1251 Shot N-S	E-W	2-480 Even	North	xy
2001-4024 Shot W-E	N-S	1-479 Odd	East	yx
2001-4024 Shot W-E	N-S	2-480 Even	North	yy

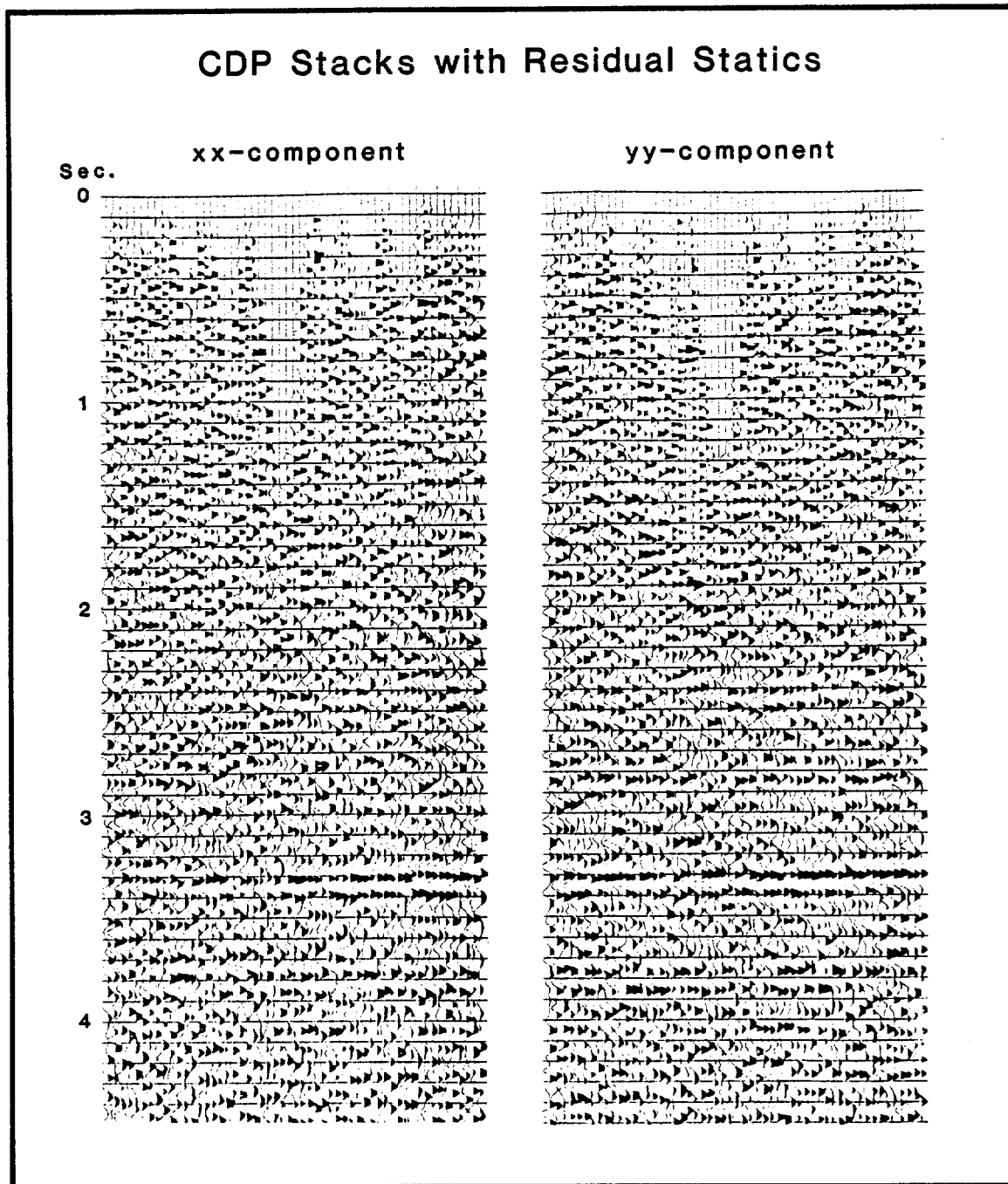


Figure 11. CDP line 94 stack with application of converted wave statics and four-component residual statics. Window used for residual statics was from 3.2 seconds to 3.3 seconds (from Vuillermoz et al, 1988).

Table 3

PRELIMINARY PROCESSING STEPS
1. Demultiplexing
2. Form SP location and elevation database
3. Geometric spreading correction *
4. Elevation statics
5. Trace balancing *
6. Velocity analysis of test lines and cross-lines
7. Deconvolution
8. Residual statics on all four components
9. Rotation analysis of undeconvolved data with statics applied
* All four components must be multiplied by the same exponent or scalar

ROTATION ANALYSIS

Four-Component Rotation

The four shear wave components (Table 2) were recorded in an (x, y) acquisition coordinate system. Four-component rotation is a similarity transformation, in a two-dimensional linear vector space, which rotates the four components from the (x, y) orthogonal basis into a new orthogonal basis. A basis is a set of linearly independent vectors such that all other vectors in the subspace or space are a linear combination of these. Alford (1986) derives this transformation for a one-dimensional model of vertical wave propagation in vertically fractured media.

In the natural coordinate system of the vertically fractured media the S1 and S2 shear wave propagation modes are distinct events; whereas, in most acquisition coordinate systems the S1 and S2 modes interfere with each other. It is therefore advantageous to find a new basis corresponding to the natural (S1, S2) coordinates and express the shear wave data in terms of this new basis (Figure 12).

The matrix equation for a counterclockwise four-component rotation by an angle θ is

$$U = R V R^T$$

where R^T is the transpose of the R matrix. The matrices R , V , and U are defined

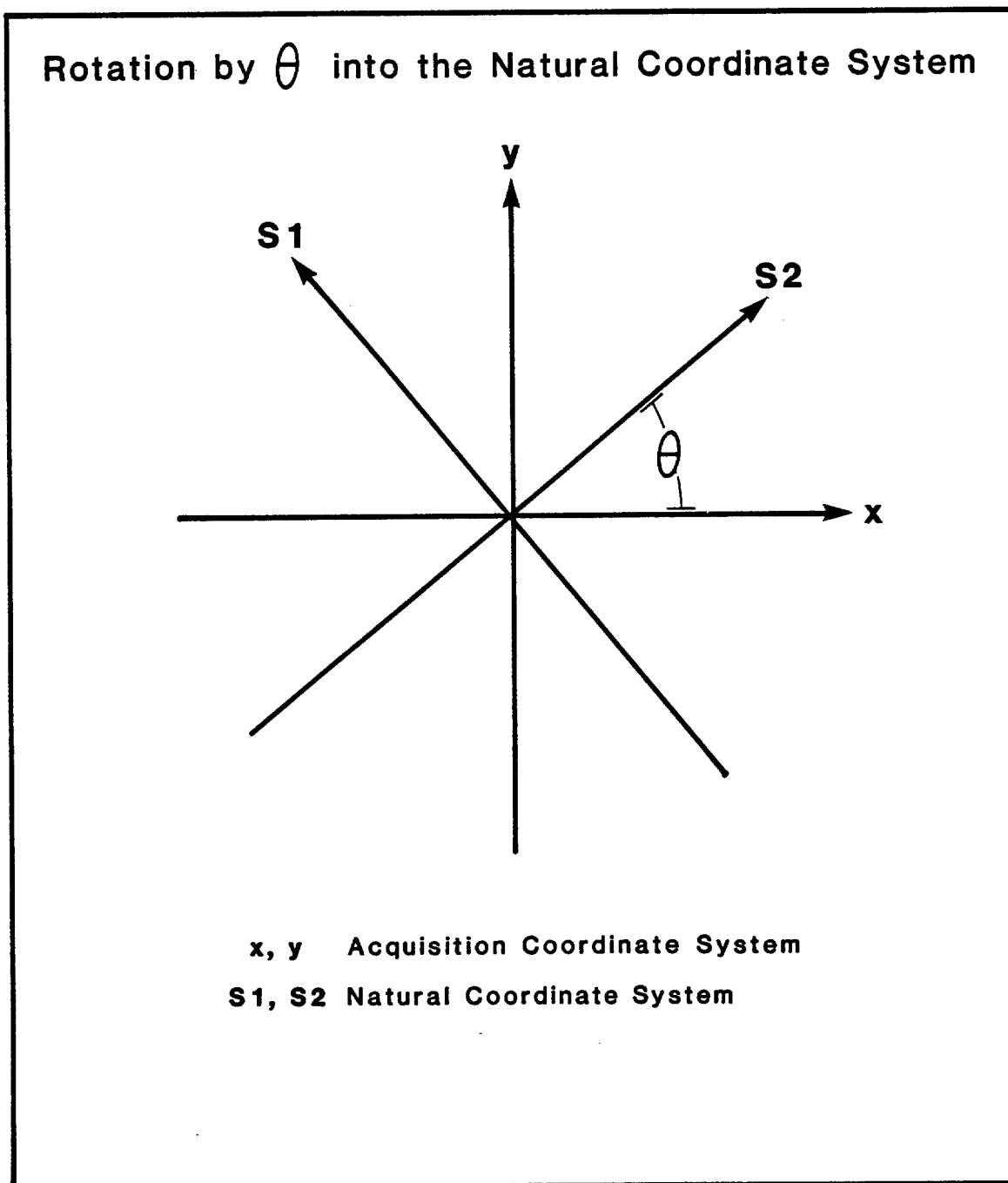


Figure 12. Rotation into the natural coordinate system of the fractures.

to be

$$R = \begin{bmatrix} \cos \theta & \sin \theta \\ -\sin \theta & \cos \theta \end{bmatrix}$$

$$V = \begin{bmatrix} xx & xy \\ yx & yy \end{bmatrix}$$

$$U = \begin{bmatrix} xx' & xy' \\ yx' & yy' \end{bmatrix} .$$

where xx' , xy' , yx' , and yy' are the four rotated components given by

$$xx' = xx\cos^2\theta + yx\sin\theta\cos\theta + xy\sin\theta\cos\theta + yy\sin^2\theta$$

$$xy' = xy\cos^2\theta - xx\sin\theta\cos\theta + yy\sin\theta\cos\theta - yx\sin^2\theta$$

$$yx' = yx\cos^2\theta - xx\sin\theta\cos\theta + yy\sin\theta\cos\theta - xy\sin^2\theta$$

$$yy' = yy\cos^2\theta - yx\sin\theta\cos\theta - xy\sin\theta\cos\theta + xx\sin^2\theta .$$

A synthetic data example of four-component rotation is shown in Figures 24-25. Four-component rotation into the natural coordinate system is approximately equivalent to diagonalizing the V matrix. The approximate eigenvectors, which correspond to the columns of the R matrix, then become the new basis for the vector space. The principle of reciprocity suggests that the V matrix is symmetric (i.e. the cross-components xy and yx are equal); however, because of noise, source

effects, and geophone effects, this usually isn't true for non-synthetic data. Since the V matrix isn't symmetric it can't be diagonalized without introducing complex eigenvalues.

Instead of diagonalizing the V matrix, an energy minimization algorithm was applied to find the optimum rotation angle. In the natural coordinate system, the principal components (xx' and yy') correspond to the S1 and S2 modes; whereas, the cross-components (xy' and yx') are reduced to noise. Therefore, in the natural coordinate system the energy of the principle components is maximized and the energy of the cross-components is minimized. An analytical expression for determining the rotation angle needed to minimize the energy of the cross-components was derived by Patricia Murtha (1988). The derivation (see Appendix A) consists of taking the derivative of the sum of the squares of the cross-components, setting it equal to zero, and solving for θ (the rotation angle). The expression for θ is

$$\theta = \frac{1}{4} \tan^{-1} \left[\frac{\sum (xxyx - xyyy - yxyy + xxyx)}{\sum \left[\frac{1}{2} (xx^2 - xy^2 - yx^2 + yy^2) - (xxyy + xyyx) \right]} \right].$$

The summation signs indicate summing over the desired window in space and time.

Analysis of Silo Field Synthetic Data

An eight layer model of the Silo Field, based on the model used by Cameron (1988), is shown in Table 4. There are three notable differences between the model in Table 4 and Cameron's model: 1.) The fracture azimuth is N 54° W. 2.) Layers 7 and 8 are vertically fractured. 3.) A thin (5 meters) isotropic "pseudo-layer" is located at the surface (not shown in Table 4). The TRISO* anisotropic modelling program requires that the surface layer be isotropic (Geoltrain, 1988).

Using the model in Table 4, I generated synthetic seismograms of the Silo Field. Geoltrain's (1988) TRISO* ray tracing program was used for the modelling. Subsequently, a program (Appendix B) implementing Murtha's (1988) four-component energy minimization algorithm was tested on the synthetic data.

Two four-component shot profiles were generated along azimuths (measured clockwise from north) of 36°, and 306°, which correspond to the S2 and S1 principal axes, respectively (Figure 13). The source pulse is a Klaunder wavelet generated from an eight-second, 5-40 Hertz sweep. A single source location was used. The vibrator pad movement was both east-west and north-south. Geophone stations are spaced at 100 meter intervals, from a minimum offset of 100 meters to a maximum offset of 2300 meters. Each station had one x-component geophone and one y-component geophone, with positive polarities to the east and north, respectively. A four millisecond sampling rate was used. The unrotated

* Proprietary software of the Center for Wave Phenomena (CWP), CSM

Table 4

SILO FIELD EIGHT LAYER OFFSET MODEL VELOCITIES AND THICKNESSES				
LAYER	P	FS	SS	THICKNESS
1	1786	768	710	305
2	2048	954	884	305
3	1847	890	823	32
4	3295	1664	1585	981
5	3441	1804	1719	419
6	3560	1856	1768	430
7	4029	2298	2188	271
8	3386	1676	1597	...

Layers 1, 2, 3, 7, and 8 are vertically fractured at N 54° W (transversely isotropic with horizontal symmetry axis).

Layers 4, 5, and 6 are transversely isotropic with a vertical symmetry axis.

P = compressional wave.

FS = fast split shear wave.

SS = slow split shear wave.

All units are metric.

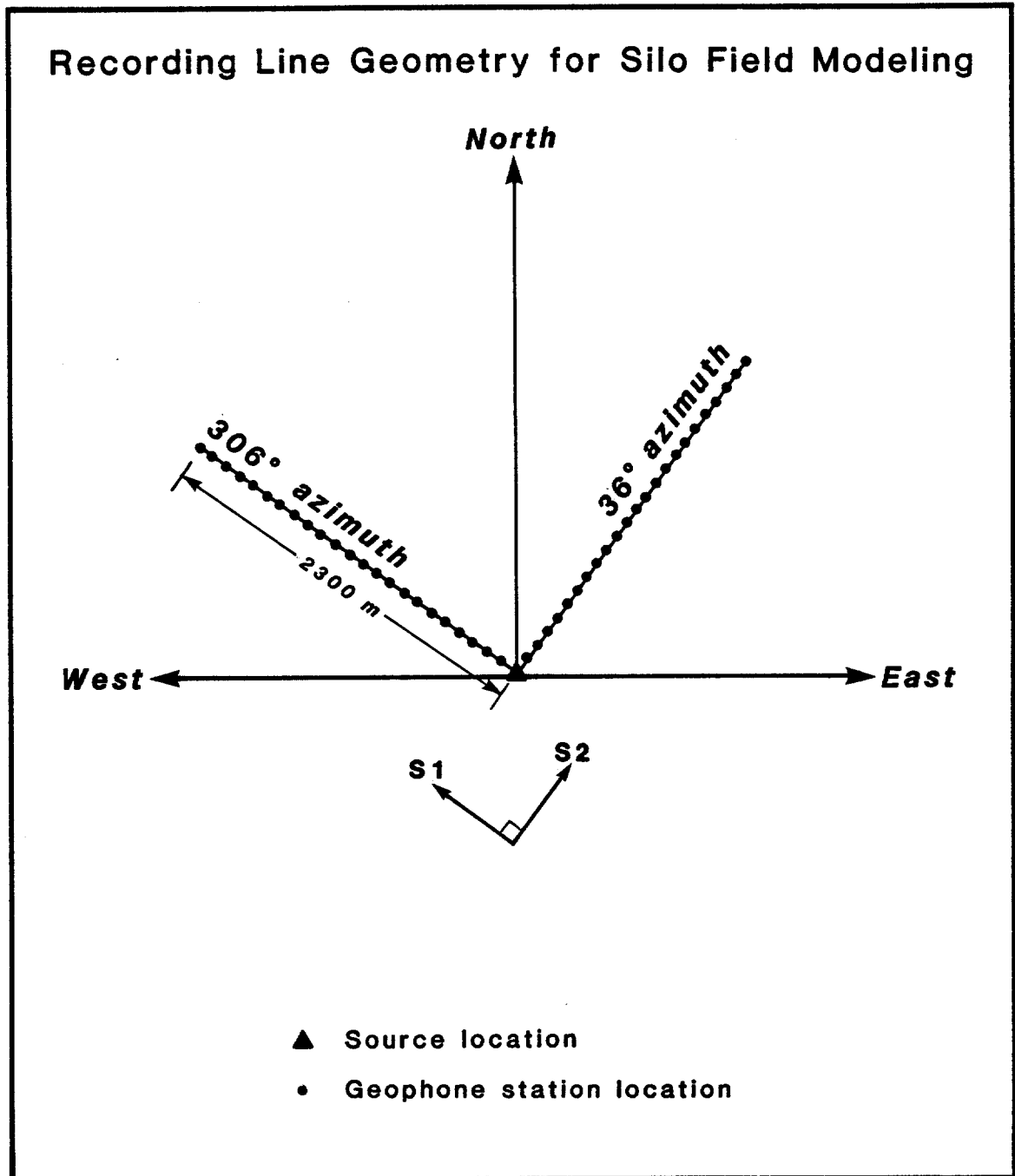


Figure 13. Recording line geometry for Silo Field modelling. Fracture azimuth is 306° from north (clockwise).

(acquisition coordinate system) and rotated (natural coordinate system) profiles are shown in Figures 14-21. Because these recording lines are along the principal axes of the vertical fractures, the in-line and cross-line shear wave polarizations remain constant for all offsets. Figures 14-21 illustrate the azimuth and offset dependence of reflection coefficients discussed by Thomsen (1988). Figures 15 and 19 contain examples of post-critical scattering at the two shallowest interfaces in the model. Post-critical reflections can result from shear to compressional mode conversions at the surface, for angles of incidence of more than $\sin^{-1} (v_s / v_p) \approx 25^\circ - 35^\circ$. Crampin (1988) calls this the shear wave window (Figure 2). All source-receiver offsets with angles of incidence less than about $25^\circ - 35^\circ$ are within the shear wave window. Post-critical reflections, recorded beyond the shear wave window, exhibit higher amplitudes, lower frequencies, and are phase-shifted.

Values of θ were calculated, using the energy minimization algorithm (Murtha, 1988), for both modelled source-receiver azimuths. A window from 3.6 seconds to 4.0 seconds was used for the analysis. The algorithm indicated a 54° rotation angle for both azimuths. The S1 polarization direction is the same for both source-receiver azimuths for two reasons: 1.) The 3.6-4.0 second window contains reflections entirely within the shear wave window. 2.) The Silo Field model used here doesn't have a pattern of orthorhombic anisotropy. A pattern of orthorhombic anisotropy is formed by three mutually perpendicular planes of mirror symmetry (Crampin, 1984). Vertical fractures and horizontal laminations,

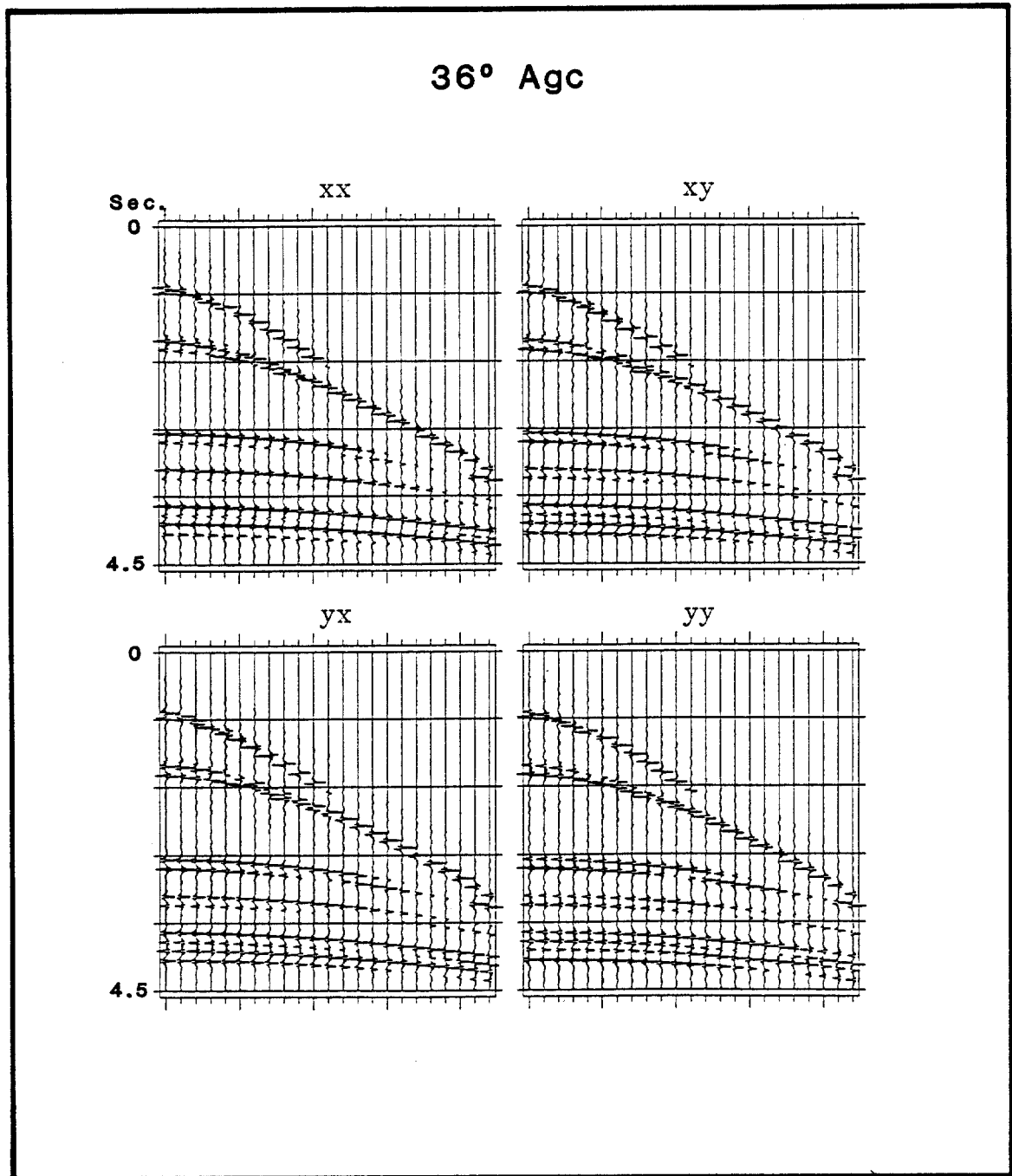


Figure 14. Shot profiles for 36° azimuth with automatic gain control applied. A 400 sample window was used for the agc.

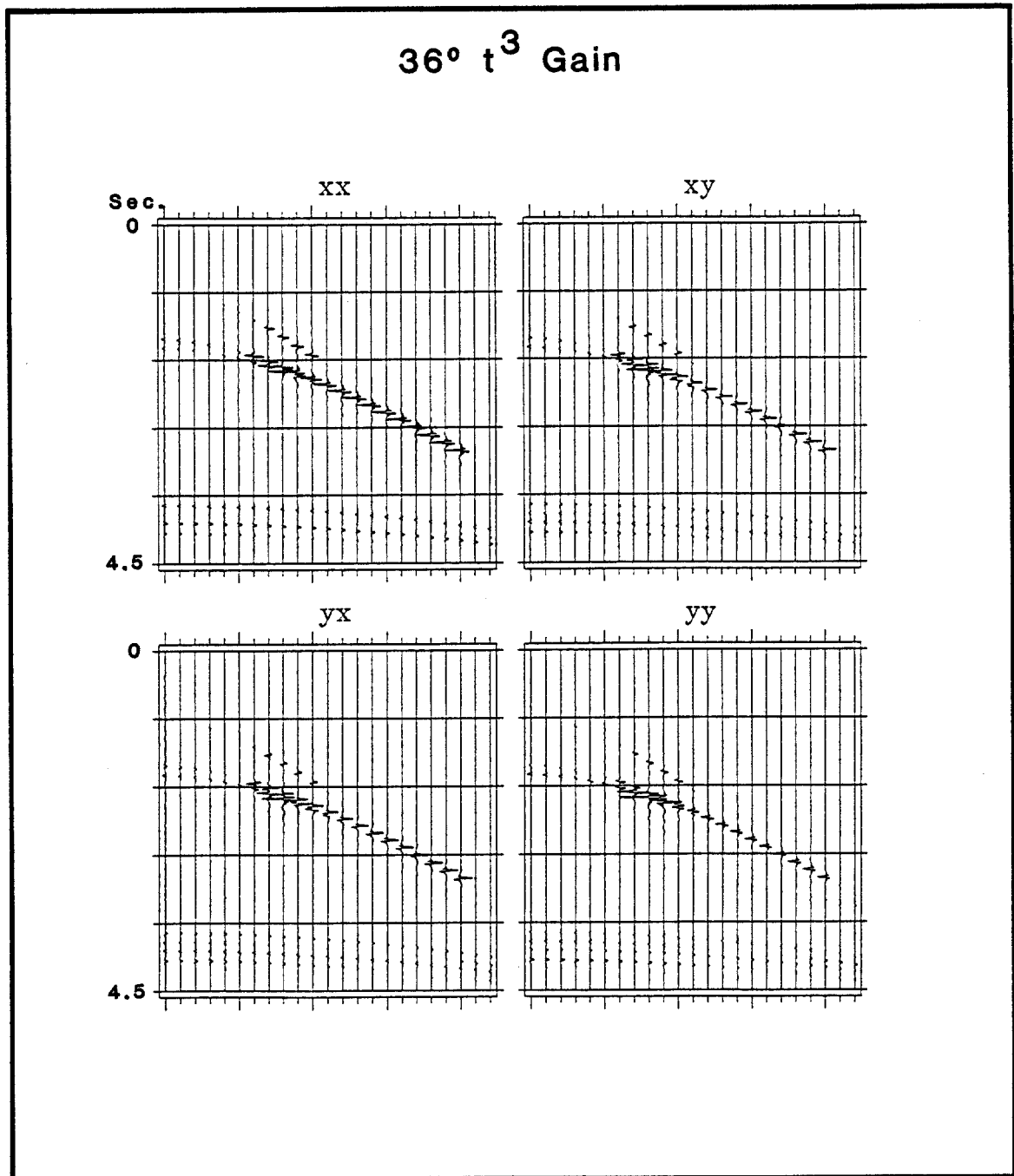


Figure 15. Shot profiles for 36° azimuth with t^3 gain applied. Shallow post-critical reflections are present. Relative amplitude between components is preserved for these plots and all other four-component plots in this thesis, when no agc has been applied.

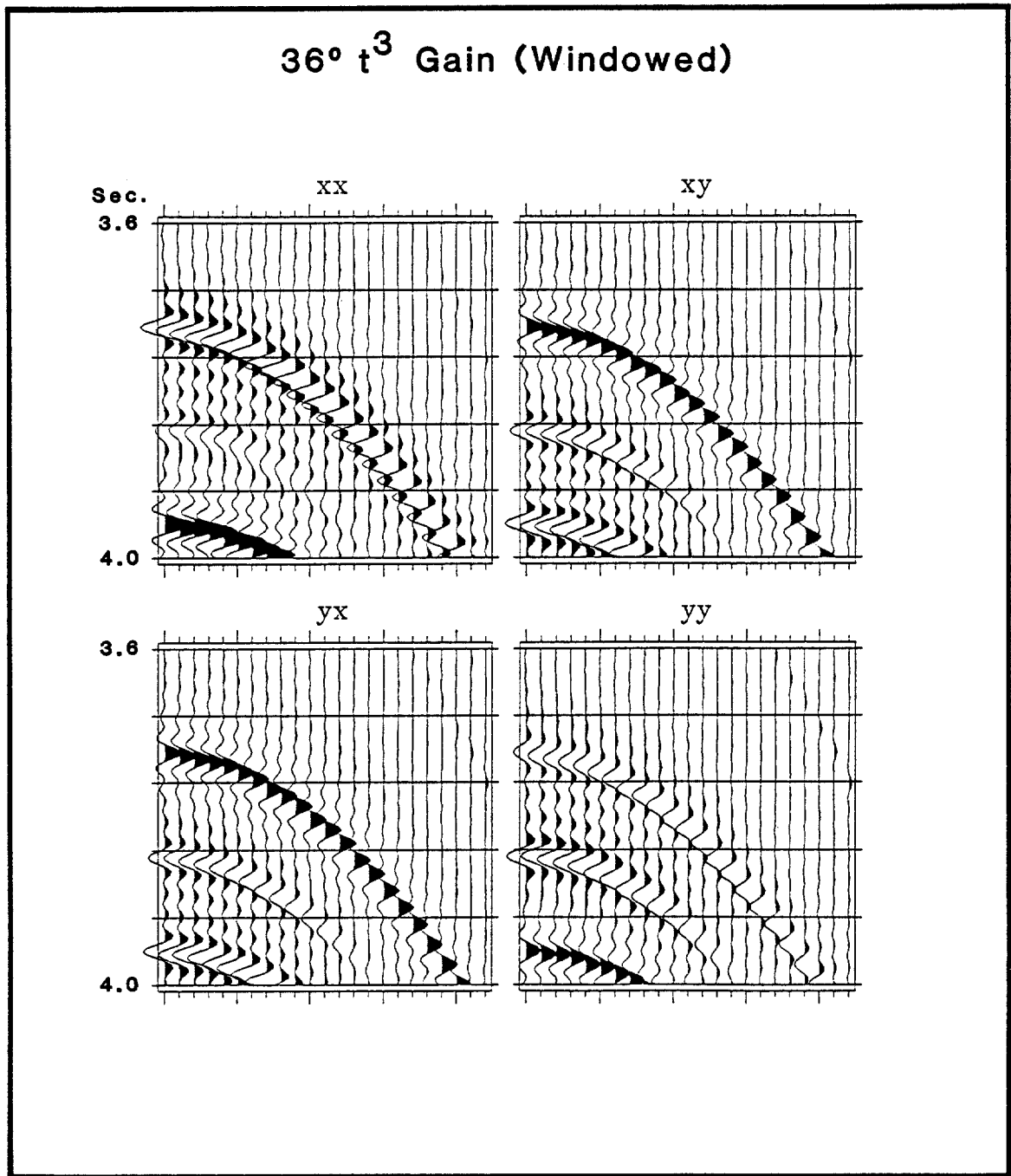


Figure 16. Windowed portion of data in Figure 15.

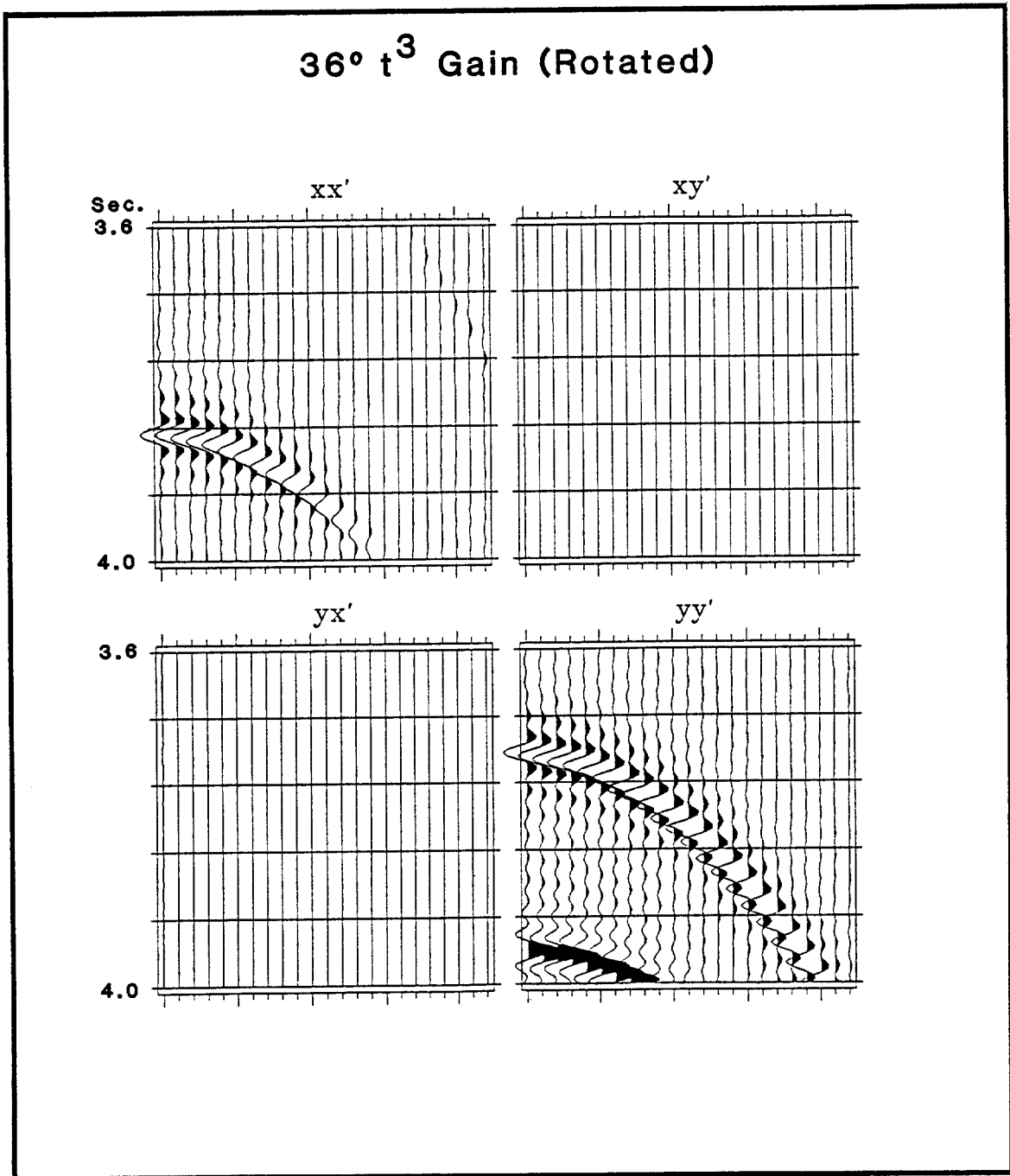


Figure 17. 54° four-component rotation of data in Figure 16.

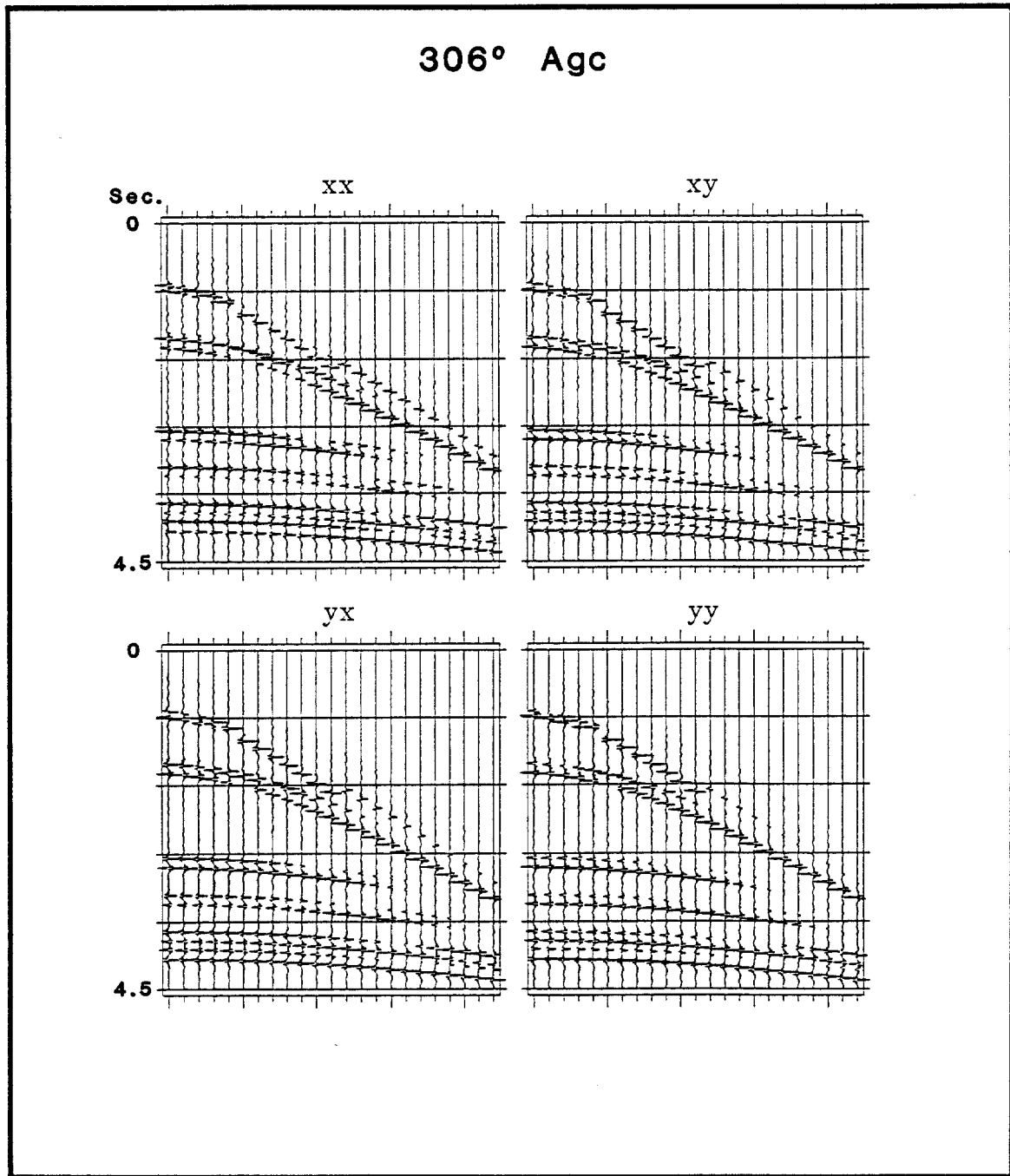


Figure 18. Shot profiles for 306° azimuth with automatic gain control applied. A 400 sample window was used for the agc.

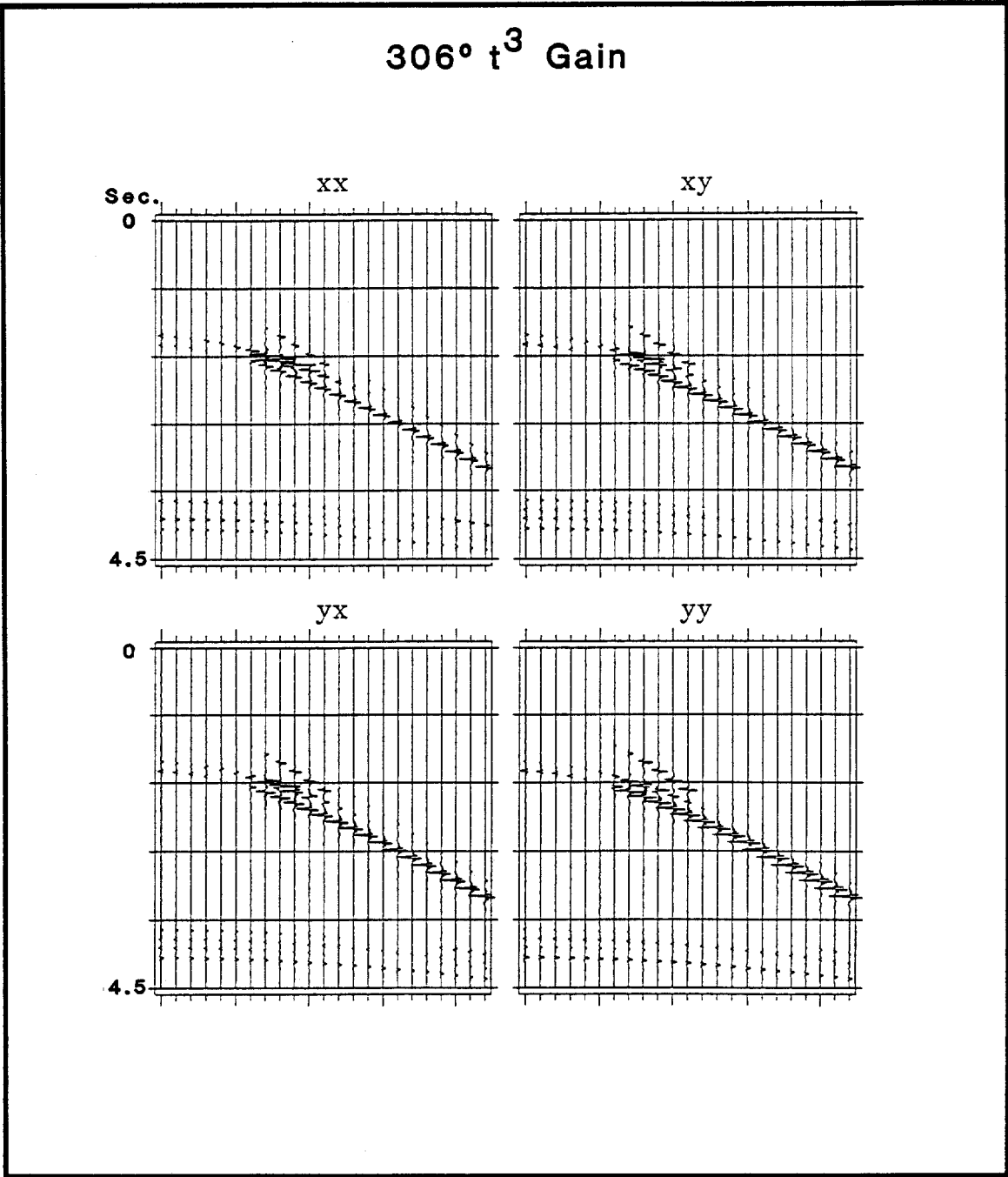


Figure 19. Shot profiles for 306° azimuth with t³ gain applied. Shallow post-critical reflections are present.

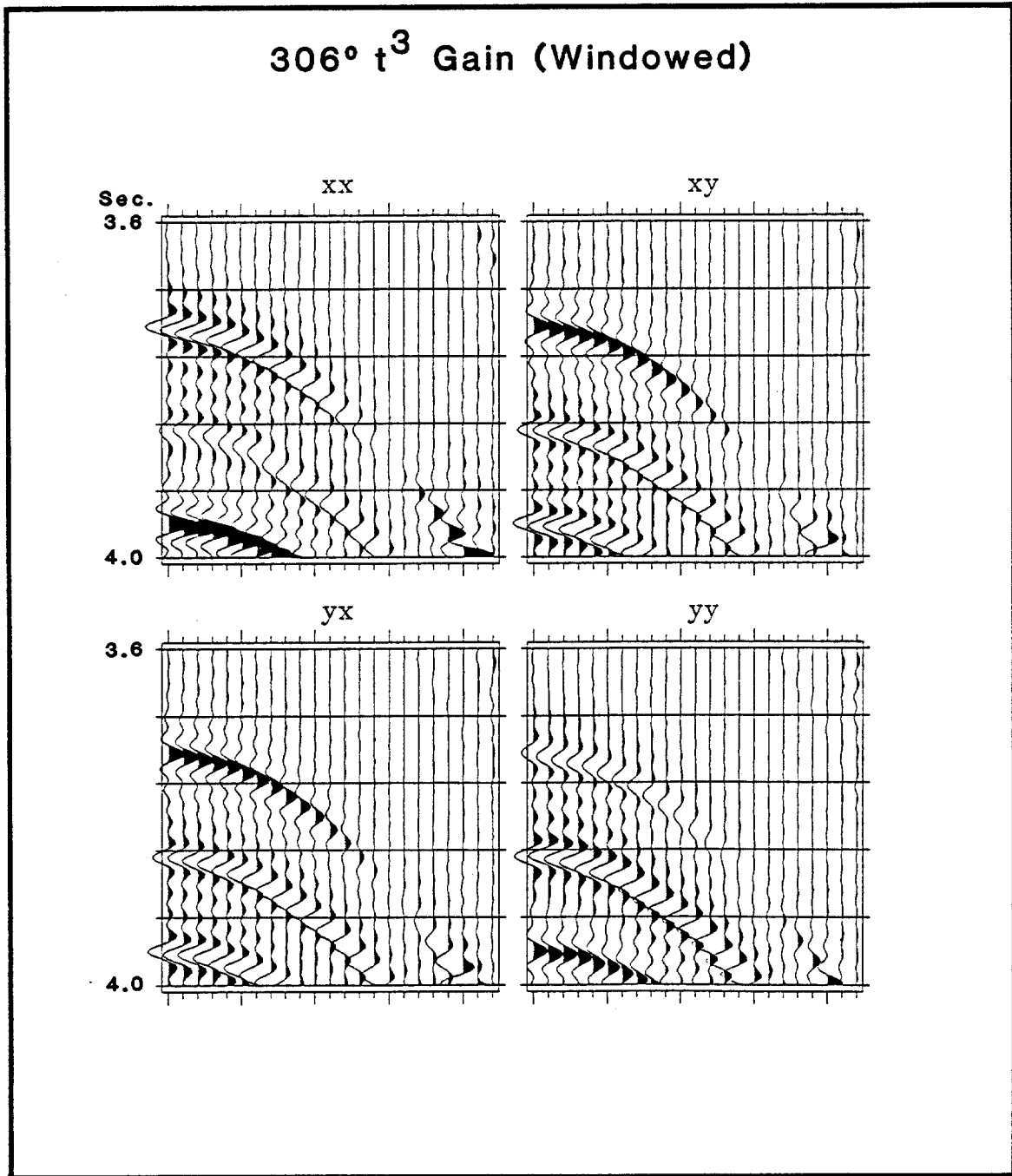


Figure 20. Windowed portion of data in Figure 19.

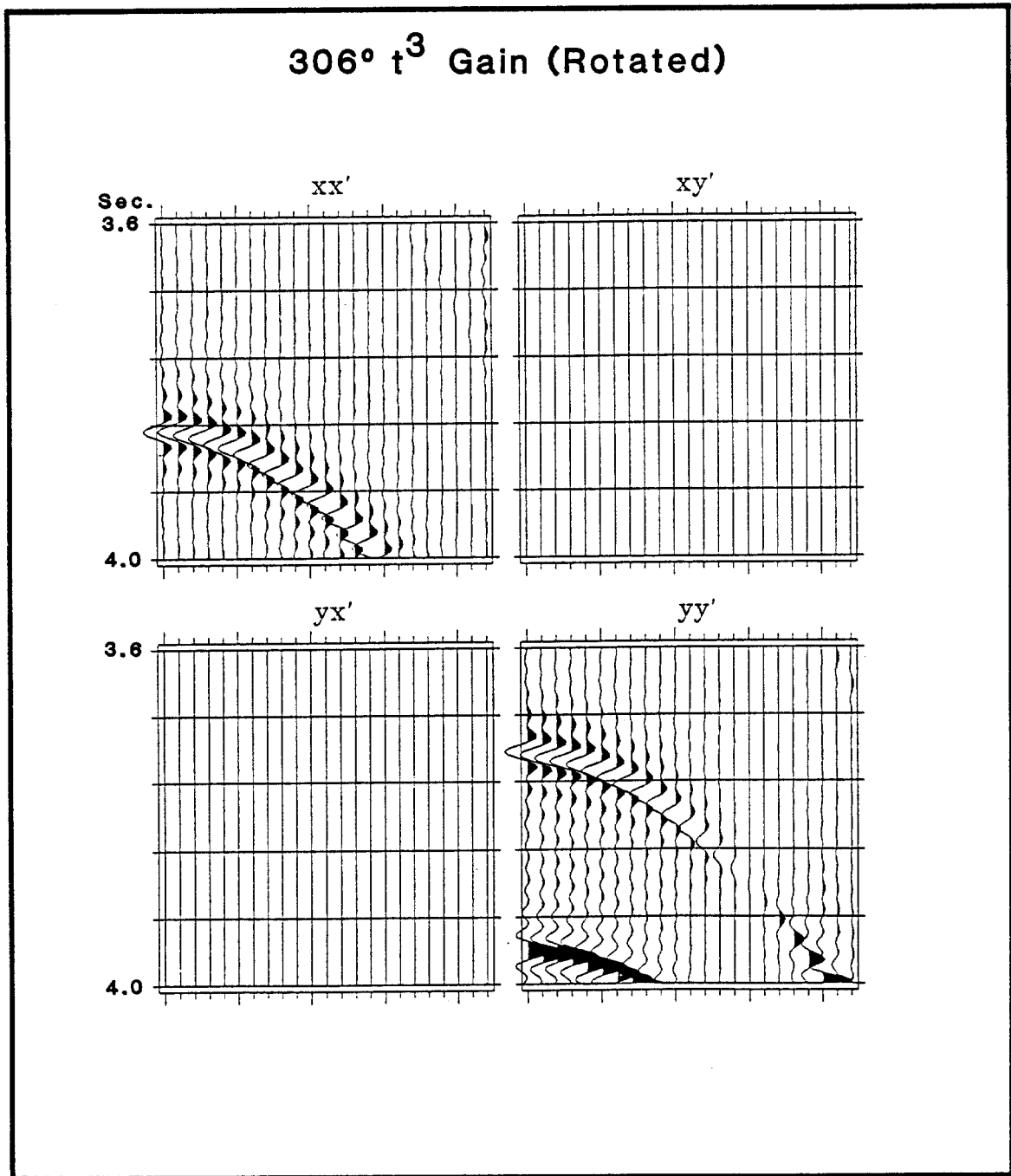


Figure 21. 54° four-component rotation of data in Figure 20.

within a single layer, result in orthorhombic anisotropy as shown in Figure 22. The black dots in Figure 22 are singularity points where the S1 and S2 split shear waves have coincident velocities. If data corresponding to different source-receiver azimuths are stacked together, polarization information may be lost due to smearing.

I tested the noise sensitivity of the energy minimization algorithm by adding Gaussian random noise to zero-offset four-component synthetic data. The zero-offset data were generated using the model in Table 5. In this model every layer contains vertical fractures which strike at N 58° W. Only two zero-offset geophones were used, with positive polarities to the north and east. The vibrator pad movement was both east-west and north-south. The source wavelet and sampling rate were the same as those used to generate the 36° and 306° offset synthetics. With these acquisition parameters only four zero-offset traces were generated, corresponding to the four components xx, xy, yx, and yy. Each trace was repeated 15 times for display and testing purposes (Figure 23). The windowed ($3.6 < t < 4.0$ seconds) unrotated and rotated data for signal-to-noise ratios of 6, 3, and 2 are shown in Figures 24-29. Table 6 shows the results of applying the energy minimization algorithm to the data in Figures 24-29. The results of applying two different variations of the algorithm are featured. In the total energy method, the total energy of all 15 traces of the cross-components, for a window from 3.6 seconds to 4.0 seconds, was minimized to obtain θ . In the trace-by-trace method, only the

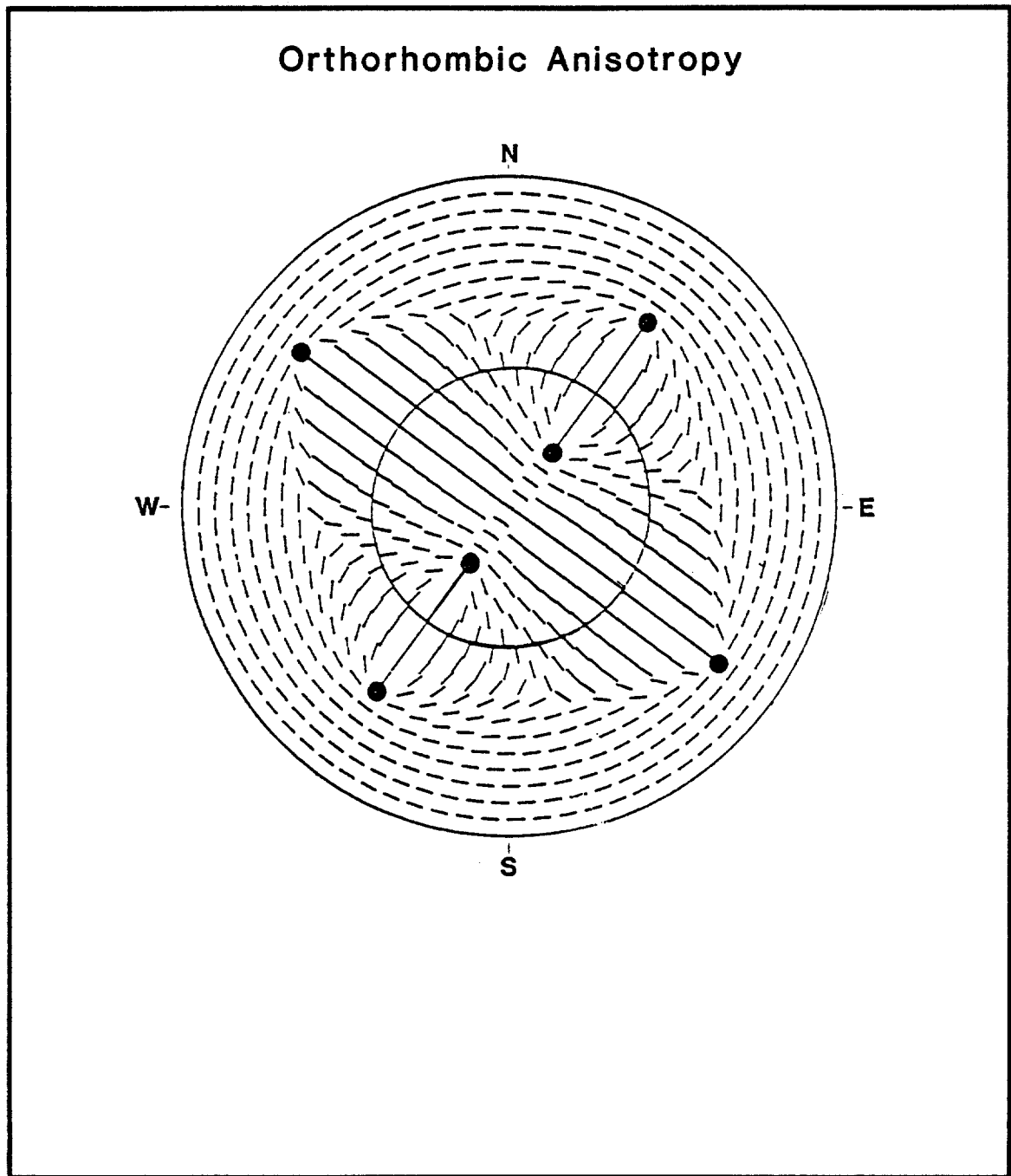


Figure 22. Plan view of projections onto a hemisphere of S1 polarization direction for a pattern of orthorhombic anisotropy. The inner circle corresponds to the shear wave window (from Lewis, 1988, modified after Crampin, 1988).

Table 5

SILO FIELD EIGHT LAYER ZERO-OFFSET MODEL VELOCITIES AND THICKNESSES				
LAYER	P	S1	S2	THICKNESS
1	1786	768	710	305
2	2048	954	884	305
3	1847	890	823	32
4	3295	1664	1585	981
5	3441	1804	1719	419
6	3560	1856	1768	430
7	4029	2298	2188	271
8	3386	1676	1597	...

All layers are vertically fractured at N 58° W (transversely isotropic with horizontal symmetry axis at N 32° E).

P = compressional wave.

S1 = fast split shear wave.

S2 = slow split shear wave.

All units are metric.

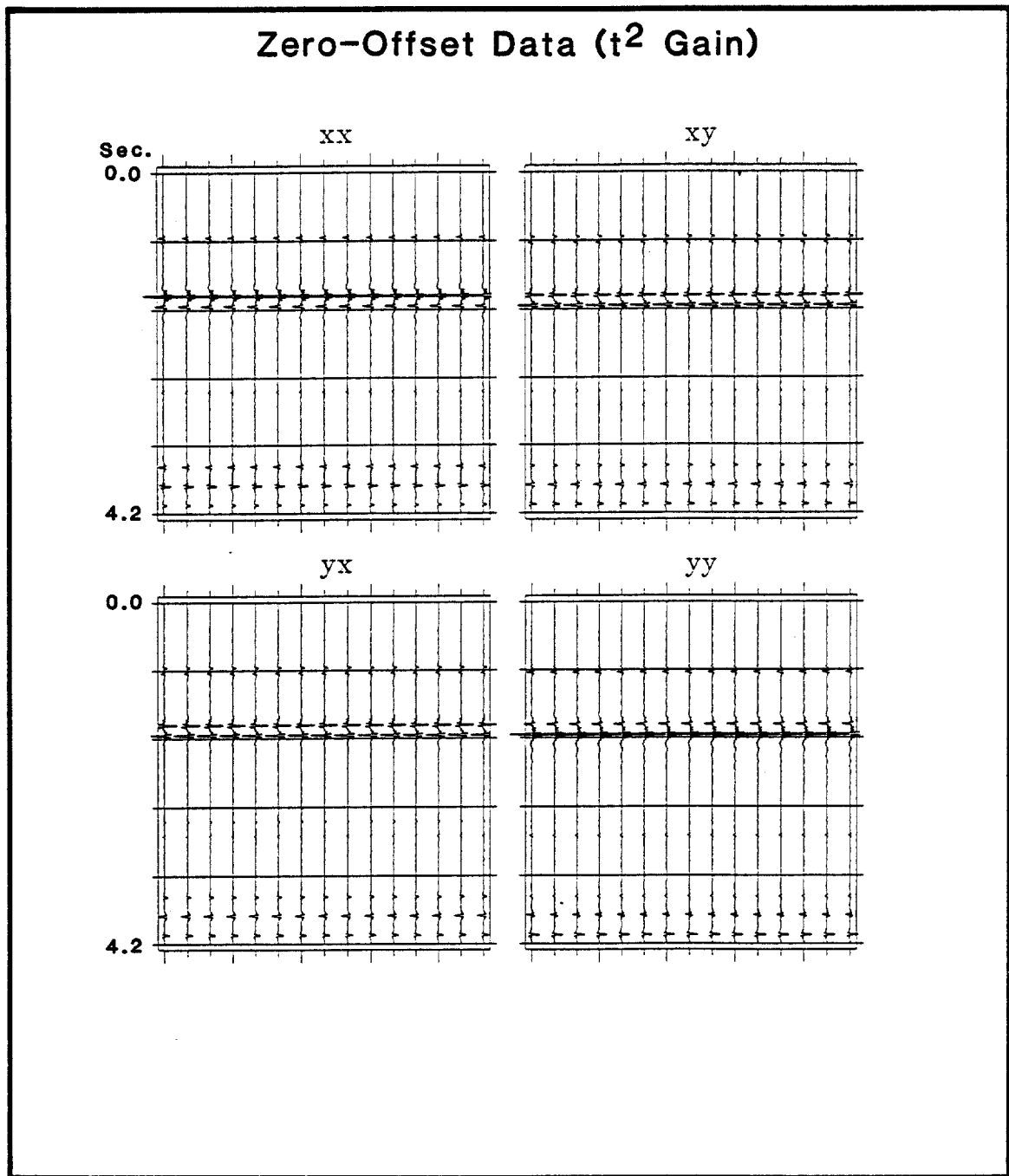


Figure 23. Zero-offset four-component data with t^2 gain applied. Each component contains 15 identical traces.

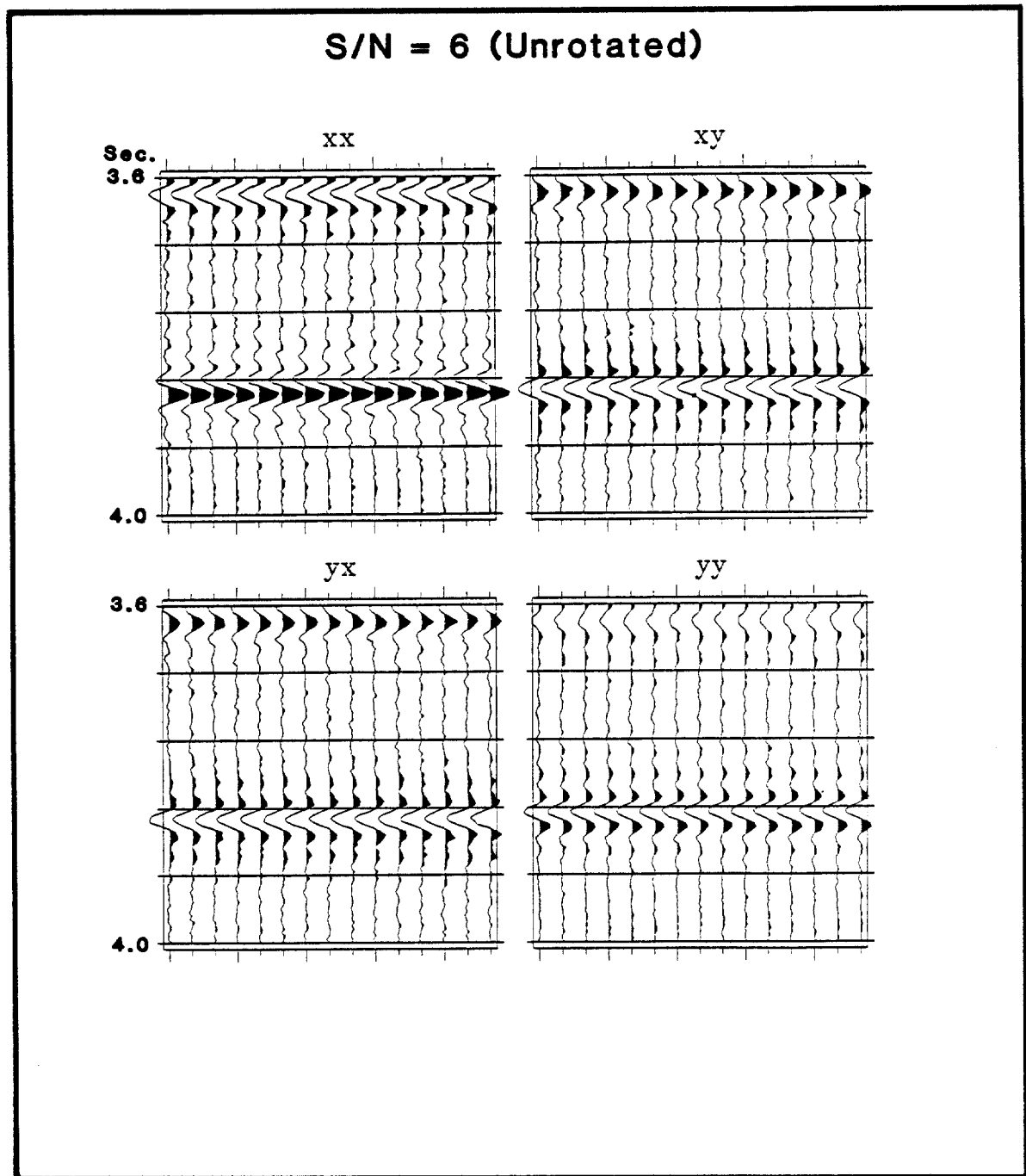


Figure 24. Windowed portion of Figure 23 with Gaussian random noise added. The signal-to-noise ratio is 6.

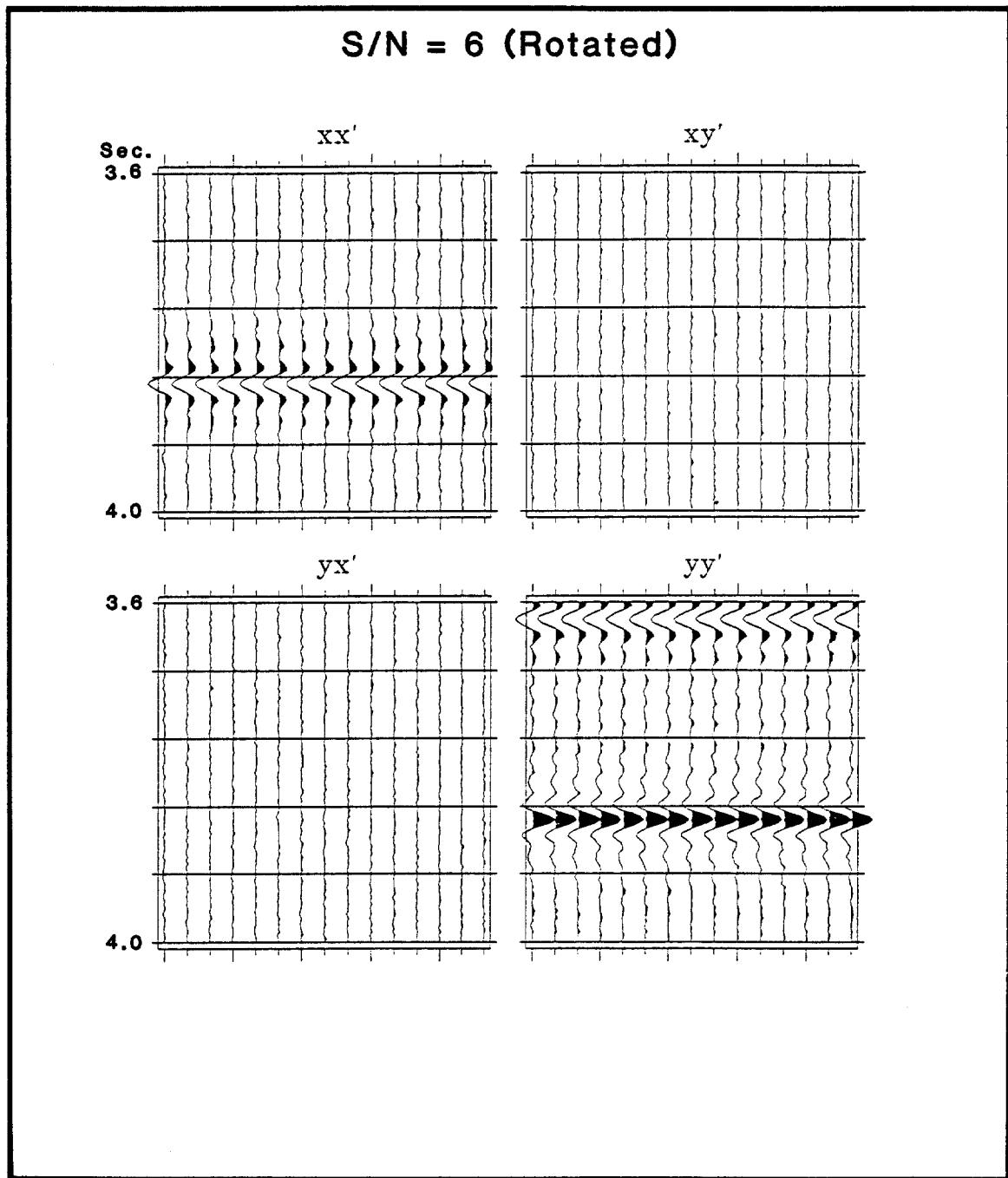


Figure 25. 58° rotation of data in Figure 24.

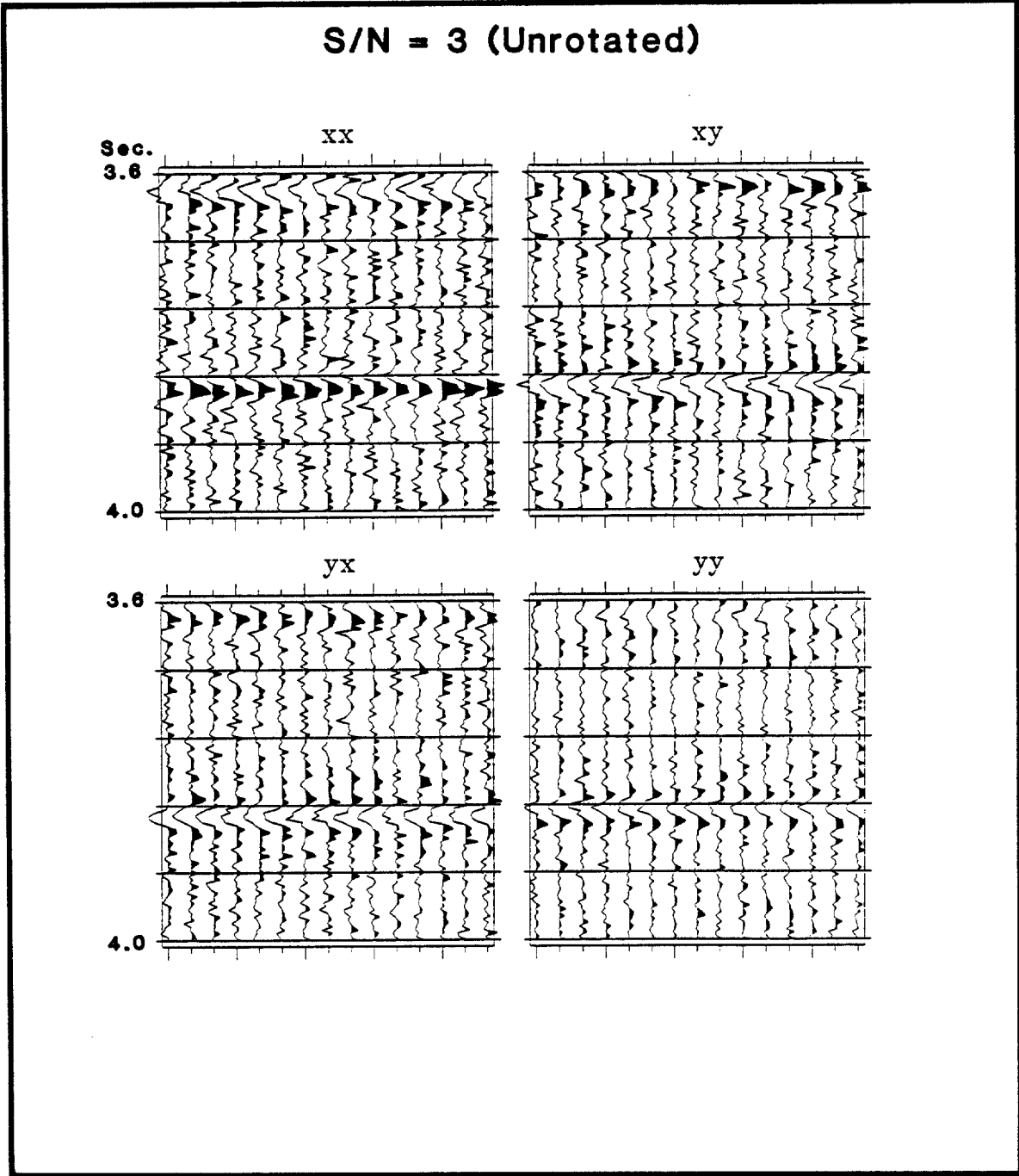


Figure 26. Zero-offset data with Gaussian random noise added corresponding to a signal-to-noise ratio of 3.

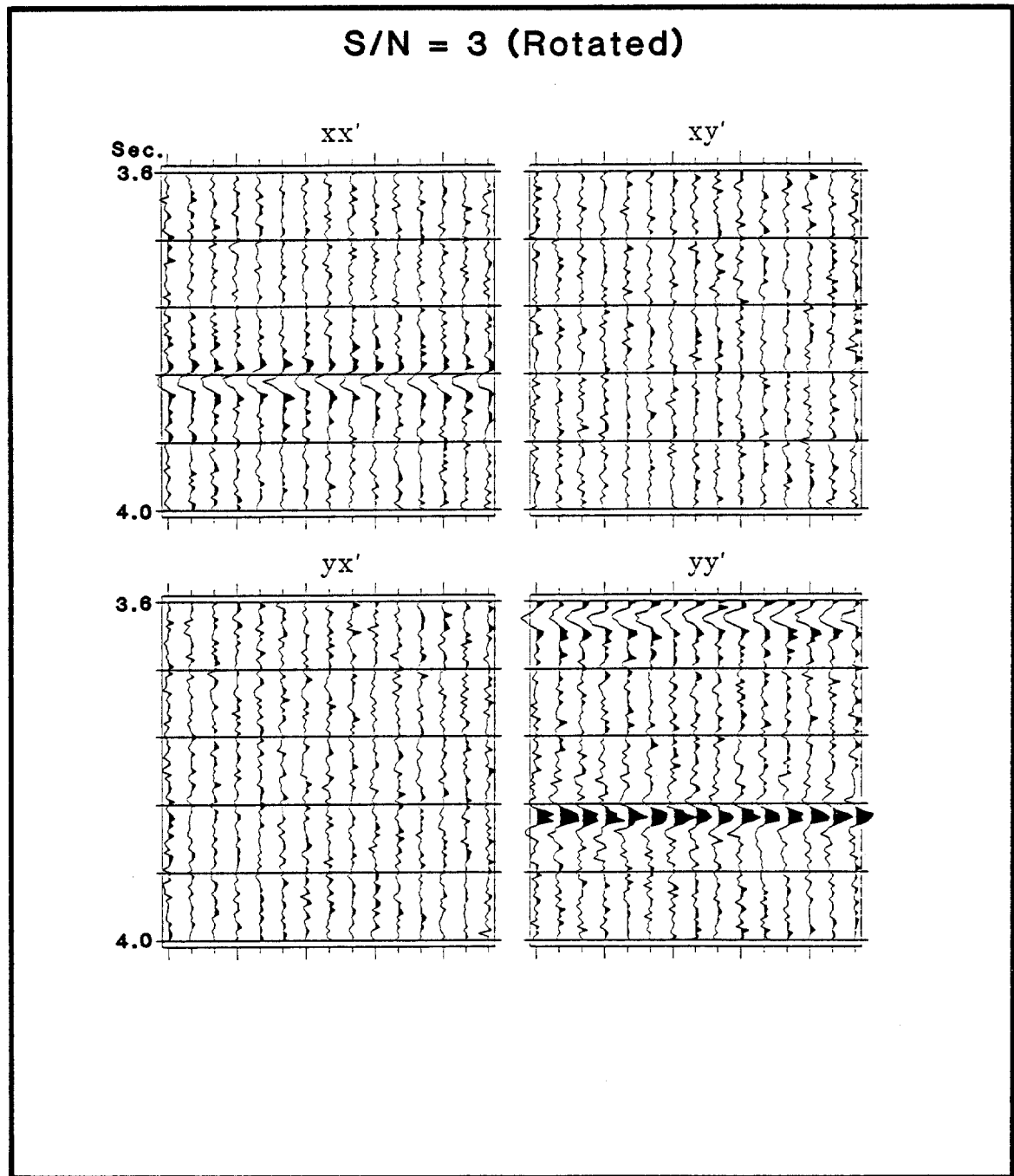


Figure 27. 58° rotation of data in Figure 26.

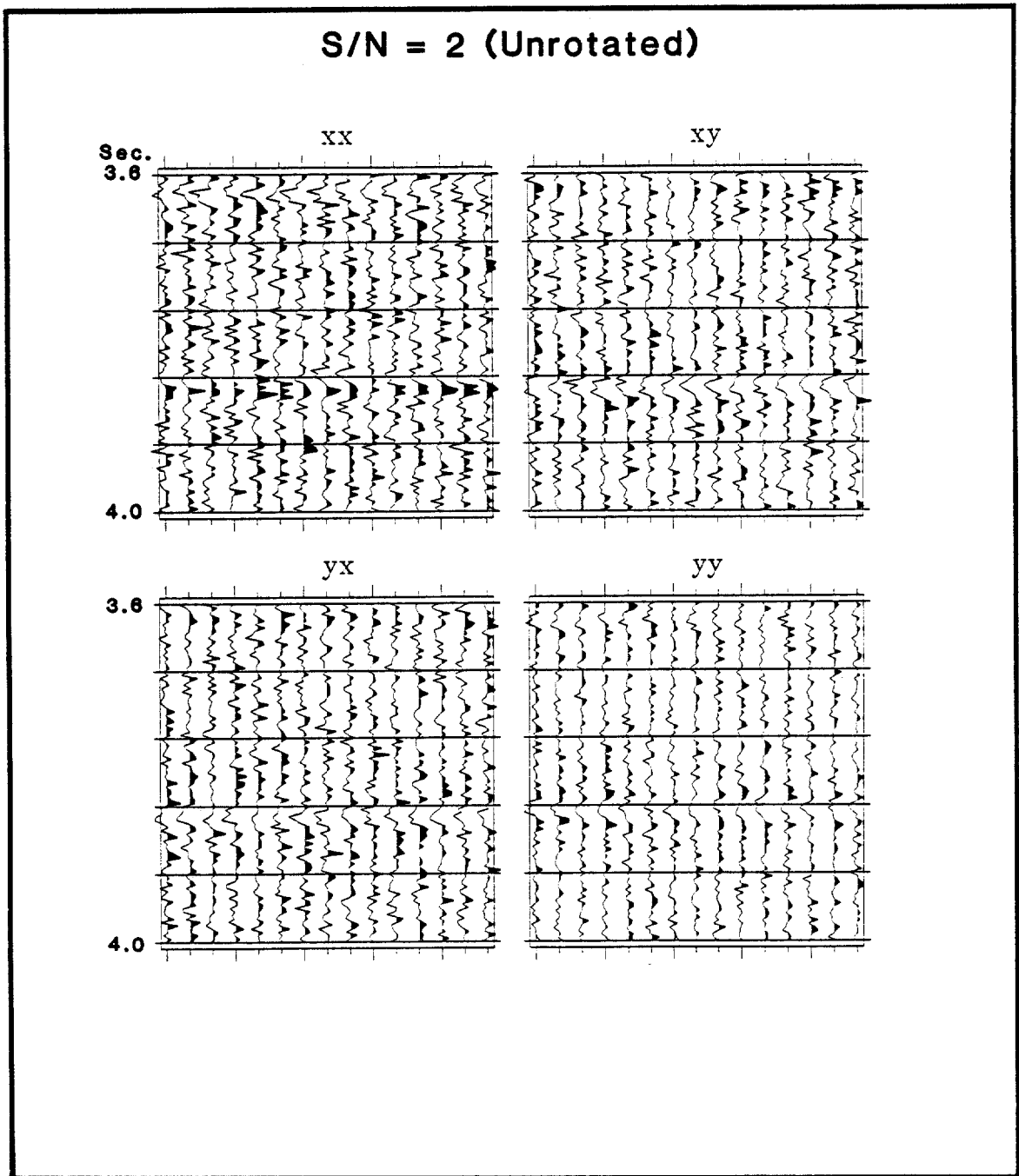


Figure 28. Zero-offset data with Gaussian random noise added corresponding to a signal-to-noise ratio of 2.

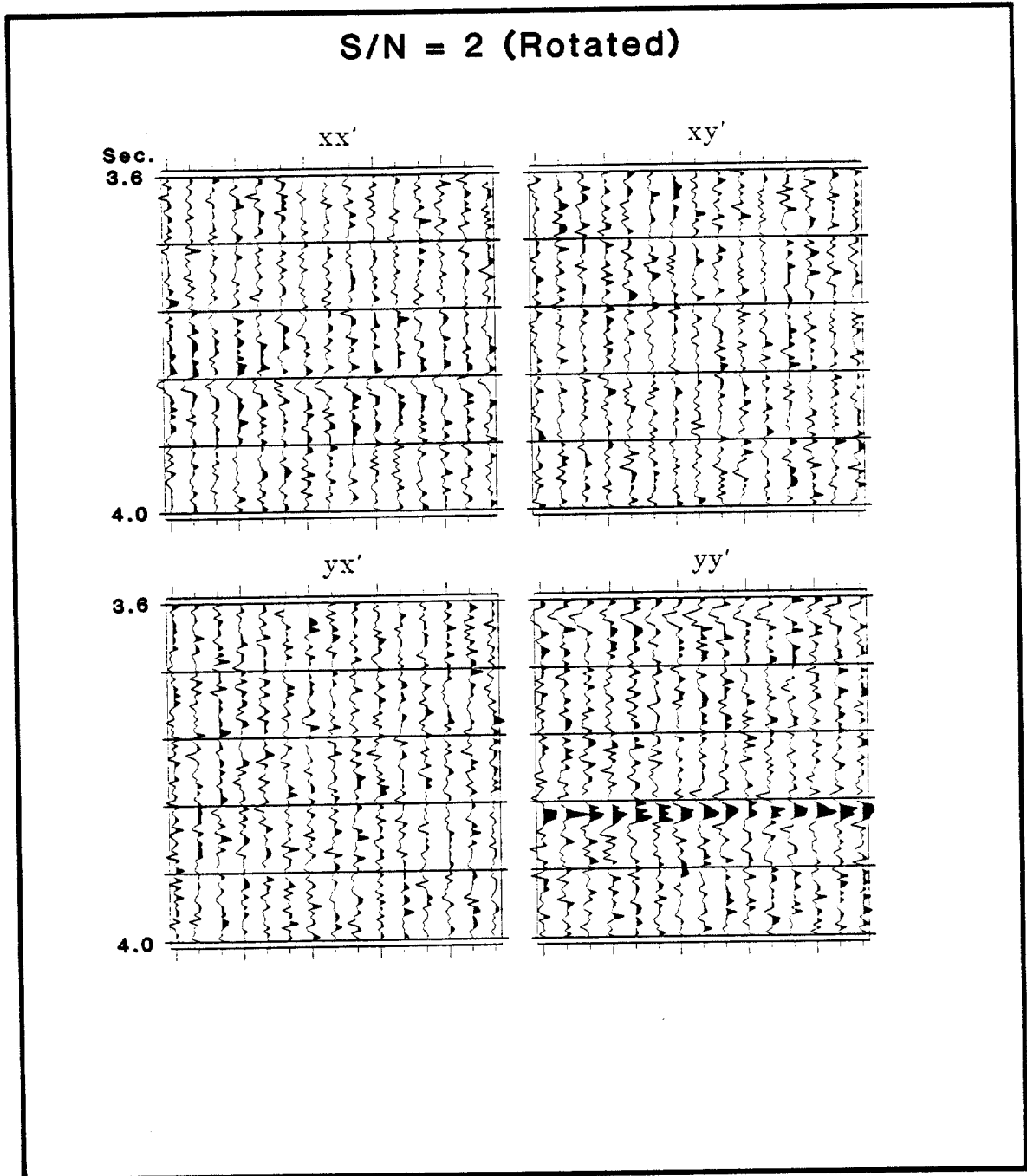


Figure 29. 58° rotation of data in Figure 28.

Table 6

ENERGY MINIMIZATION RESULTS FOR NOISY DATA			
Algorithm	Signal-to-noise ratio		
	6	3	2
Total energy θ	58.0	57.7	58.5
Trace-by-trace $\hat{\theta} \pm \hat{\sigma}$	58.0 ± 0.3	57.6 ± 1.5	58.9 ± 6.8

energy of one windowed ($3.6 < t < 4.0$ seconds) trace per component was used to calculate values of θ_i . This was repeated for all 15 traces and then an average value for θ_i , $\hat{\theta}$, was calculated. In addition, a standard deviation, $\hat{\sigma}$, was calculated for $\hat{\theta}$. $\hat{\theta}$ and $\hat{\sigma}$ were calculated via

$$\hat{\theta} = \sum_{i=1}^n \frac{\theta_i}{n}$$

$$\hat{\sigma} = \left[\frac{\sum_{i=1}^n (\theta_i - \hat{\theta})^2}{n - 1} \right]^{1/2}$$

for $n = 15$.

The results of the two variations of the energy minimization algorithm agree very closely. The standard deviation of $\hat{\theta}$ is inversely proportional to the signal-to-noise ratio.

Figure 30 contains plots of the ratio of the total (all 15 traces) principal component energy to the total cross-component energy, as a function of rotation angle, for the data of Figures 24-29. The total deflection and width of these energy ratio curves can be used as a measure of how well resolved θ , calculated via the energy minimization algorithm, is.

From these synthetic data random noise analyses it can be concluded that the resolution of the energy minimization algorithm decreases as the signal-to-noise

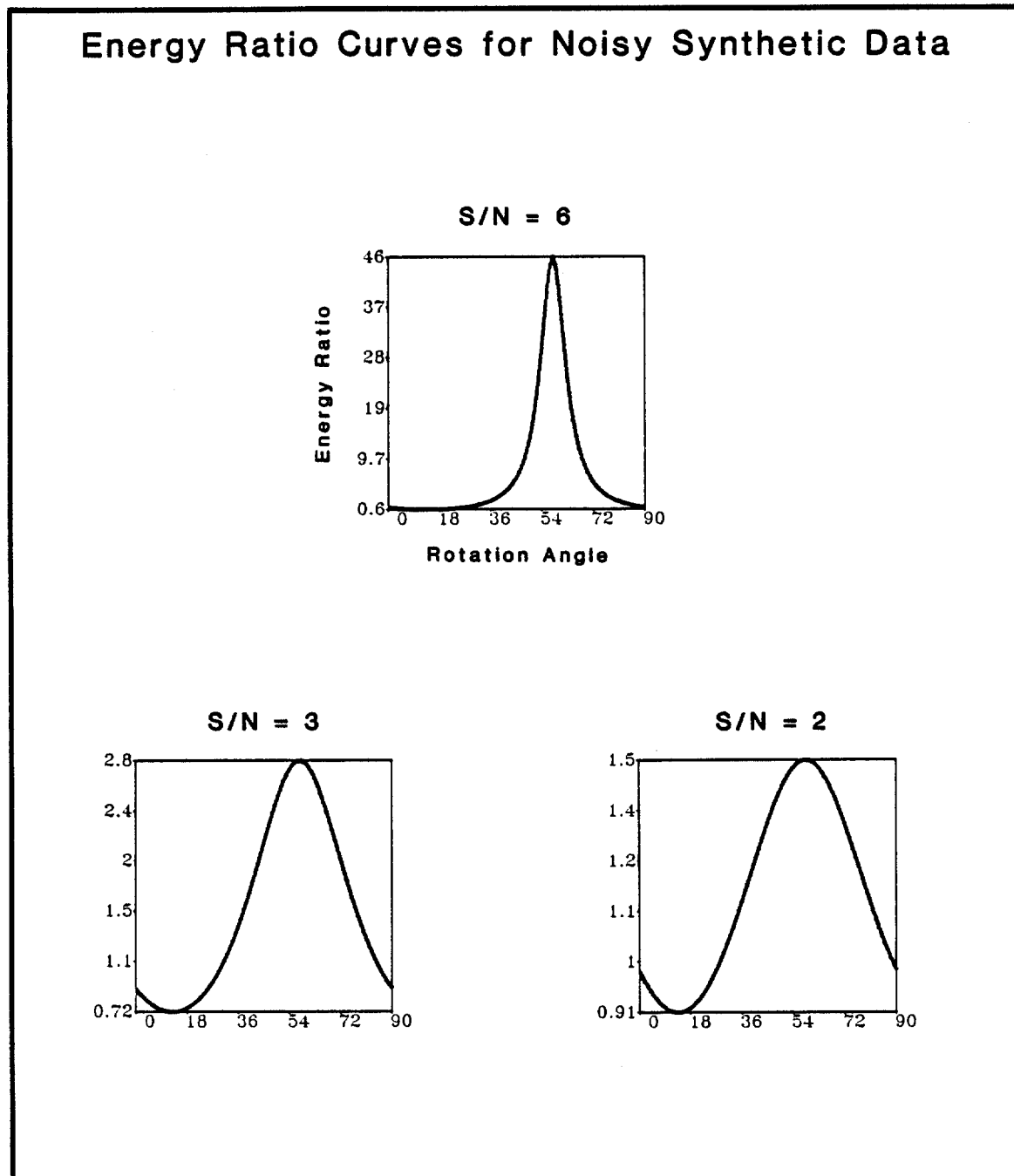


Figure 30. Energy ratio curves for signal-to-noise ratios of 6, 3, and 2, obtained by rotating the data in Figures 24, 26, and 28.

ratio approaches values of two or less. Since the error of the calculated rotation angle for low signal-to-noise ratios is only on the order of a few degrees, it can be concluded that random noise poses no major threat to rotation analysis via the energy minimization algorithm. Unfortunately, the real Silo Field data contains a lot of coherent noise (especially groundroll). High energy coherent noise has an important effect on the θ calculated with the energy minimization algorithm.

Robertson and Corrigan (1983) showed that SH- and SV- vibrator sources have different radiation patterns. In the experiment which they conducted the SV-source had a displacement amplitude that was 1.5 to 2 times greater than the displacement amplitude of the SH-source. Figure 31 shows the errors resulting from applying the energy minimization algorithm when the x-component source has a different displacement amplitude than the y-component source. The absolute value of the rotation angle error is plotted, for five different rotation angles (corresponding to the strike of vertical fractures), as a function of the ratio of the x-component source amplitude to the y-component source amplitude. The errors for rotation angles greater than 45° are not shown because the error curves are symmetric about 45° . The energy minimization algorithm maps values of θ which are greater than 45° into the 0° to -45° range. Therefore errors for rotation angles which are greater than 45° are equal in magnitude but opposite in sign to the errors for rotation angles in the 0° to 45° range. The rotation angle error for an x-component to y-component source displacement ratio of 1.5 to 2 is less than

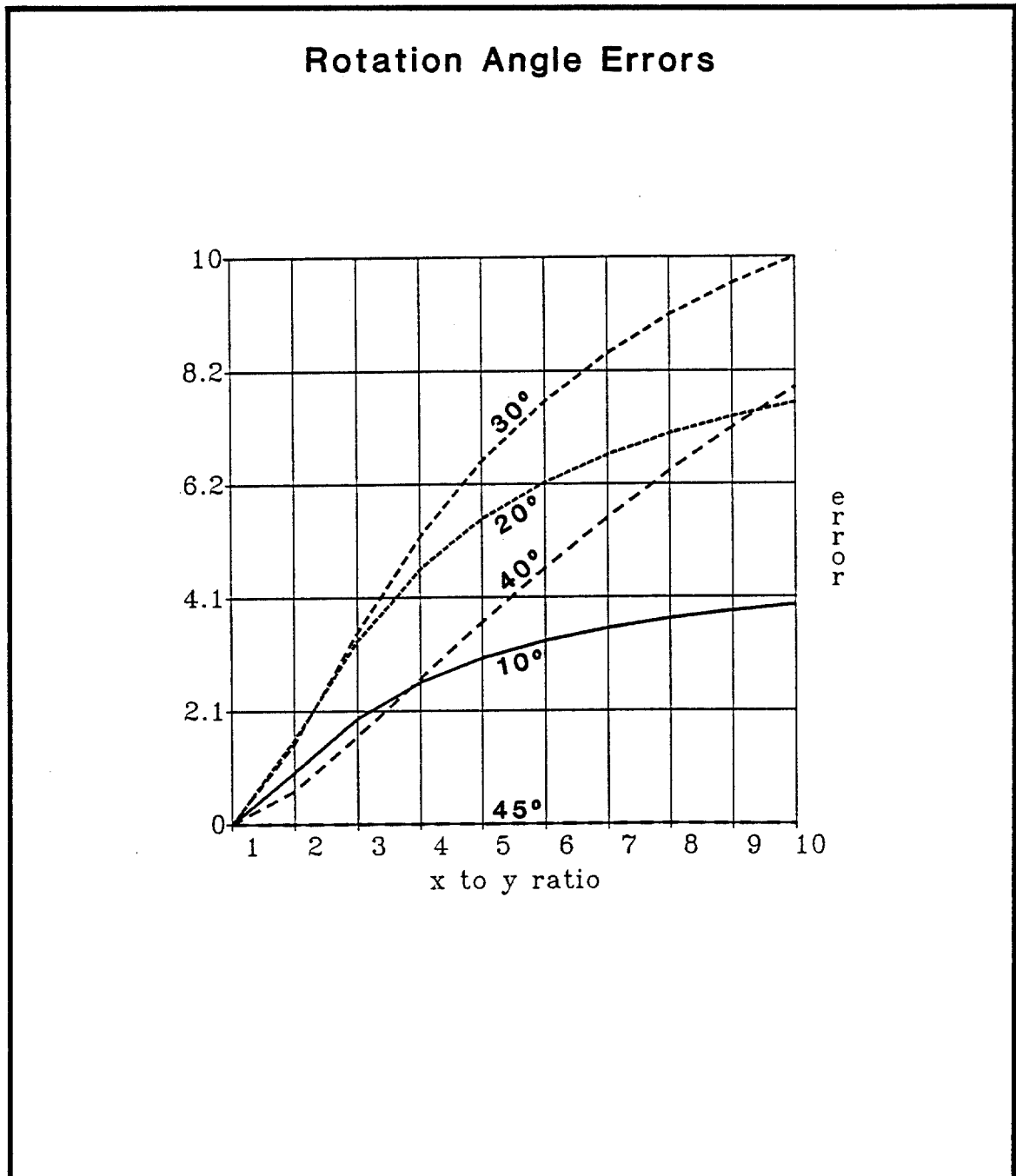


Figure 31. Absolute value of the error, in degrees, of the calculated rotation angle as a function of the ratio of the x-component source or receiver displacement amplitude to the y-component source or receiver displacement amplitude. The error curves for 5 different fracture azimuths are plotted.

2° for all possible rotation angles (Figure 31).

For this error analysis an impulse source with unit amplitude was used. A time window consisting of two samples corresponding to the S1 and S2 mode traveltimes was used. Notice that the error at 45° is always zero. It can be concluded from Figure 31 that if the differences in x- and y-component source displacement amplitude in Silo Field were less than an order of magnitude, then the resulting rotation angle error will not be significant. Based on Robertson and Corrigan's results, it will be assumed that the displacement amplitude differences between the x- and y- component sources in Silo Field were less than an order of magnitude. The same error curves result for differences in geophone coupling between the x- and y-component receivers. Since the geophones were frozen into the ground, it will be assumed that any coupling differences between x- and y-component geophones in Silo Field were less than an order of magnitude.

Analysis of Silo Field Data

In order to test for azimuth dependence of shear wave polarization directions in the Silo Field, geophone azimuth stacks were created. For each geophone station, ten geophone azimuth stacks were formed corresponding to ten different 18 degree sectors (Figure 32). For example, the geophone azimuth stacks for sector two (see Figure 32) consist of the stacks of all traces having a source-receiver azimuth within the range 54° to 72° (clockwise from north). The maximum

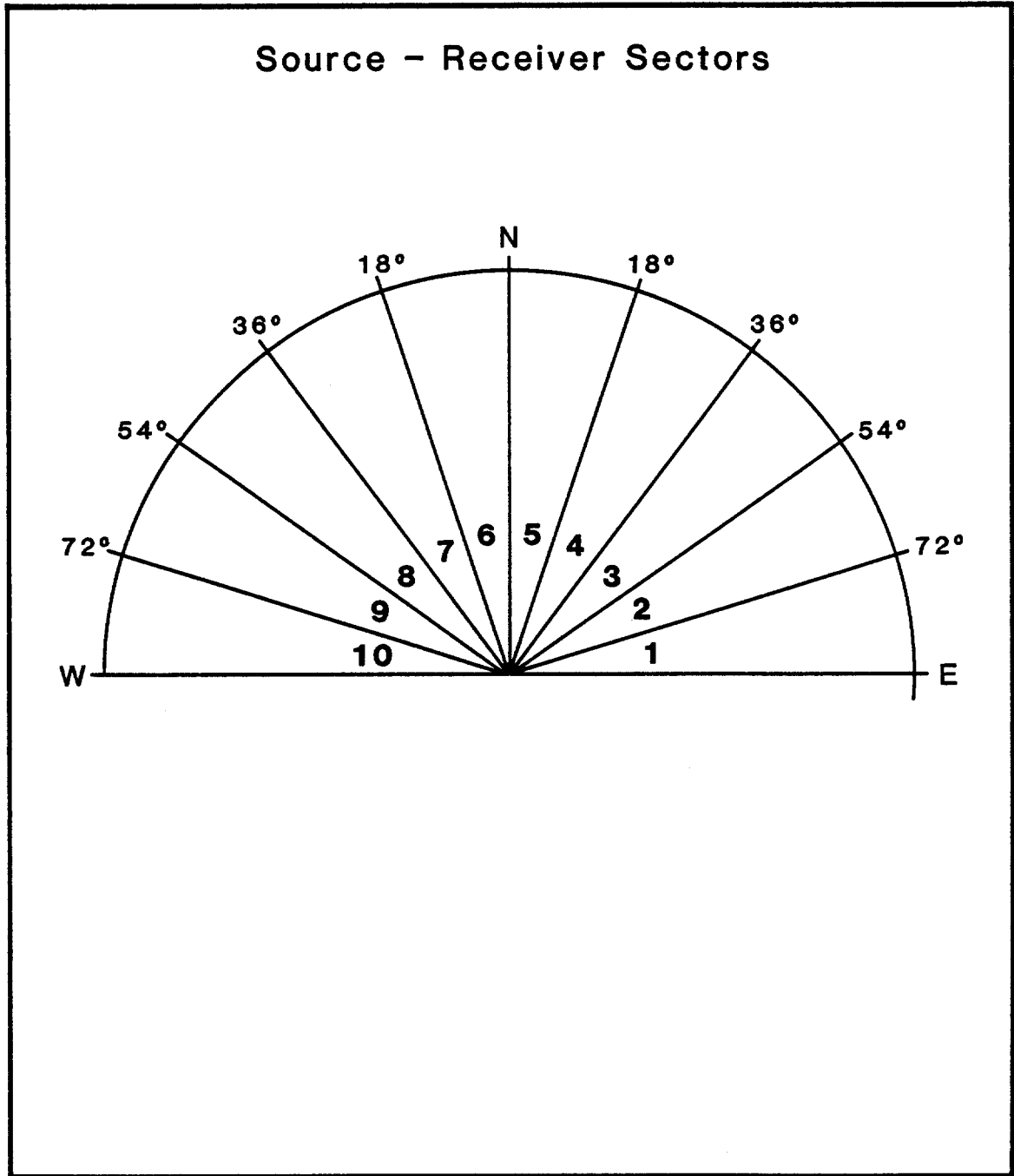


Figure 32. 18° sectors for geophone azimuth stacks (modified from Lewis, 1988).

source-receiver offset of the traces included in the geophone azimuth stacks was limited to 2377 meters. This restricted the rotation analysis to reflections within the shear-wave window (see Figure 22).

Geophone azimuth stacks are more appropriate for 3-D rotation analysis than CDP azimuth stacks for the the main reason that the shallowest anisotropic layer determines the final shear wave polarizations observed at the surface. It is possible that the orientation of the anisotropy symmetry axis might change from the geophone location to the CDP location. This could result in an erroneous interpretation of the shear wave polarization directions for the CDP location.

A four-component rotation was performed on the geophone azimuth stacks. Five rotated datasets were created, corresponding to counterclockwise rotation angles of 18° , 36° , 54° , 72° , and 90° . Figure 33 shows the five rotated yy-component data sets for sector three of geophone line six (Figure 7). These displays show the groundroll that contaminates most of the 3-D shear wave data.

In order to remove some of the groundroll, every six consecutive traces of the rotated geophone azimuth stacks were vertically stacked. Vertical stacking reduced the number of traces in each sector from 30 to 5. Figures 34-37 show the vertically stacked traces for the ten sectors of geophone line six. The five rotated data sets are displayed for each sector. The vertical stacking did help remove some of the groundroll. No frequency-domain filter was used to eliminate groundroll

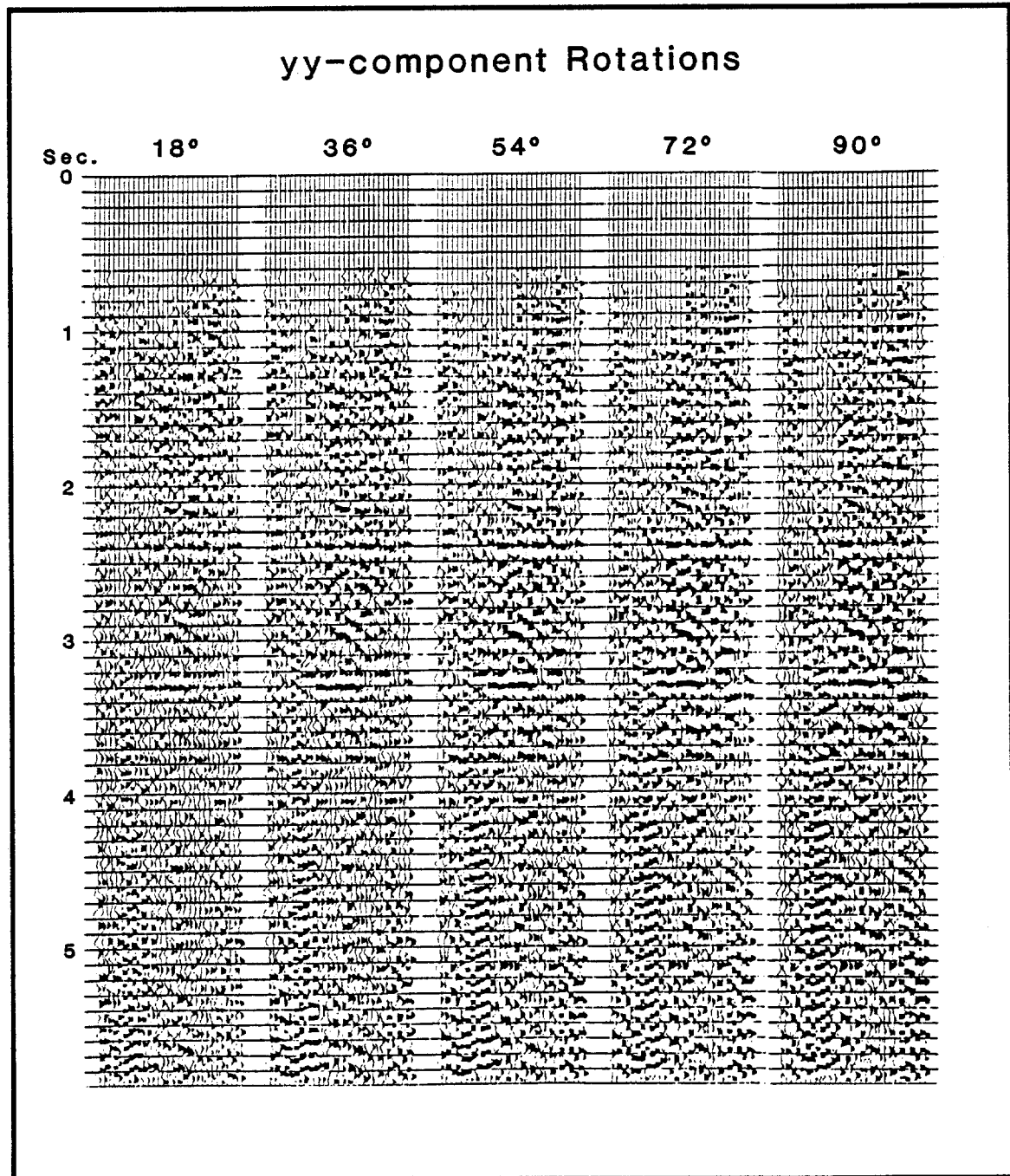


Figure 33. yy-component rotations for sector 3 of geophone line 6. From left to right these sections represent counterclockwise rotations of 18°, 36°, 54°, 72°, and 90°, respectively (from Lewis, 1988).

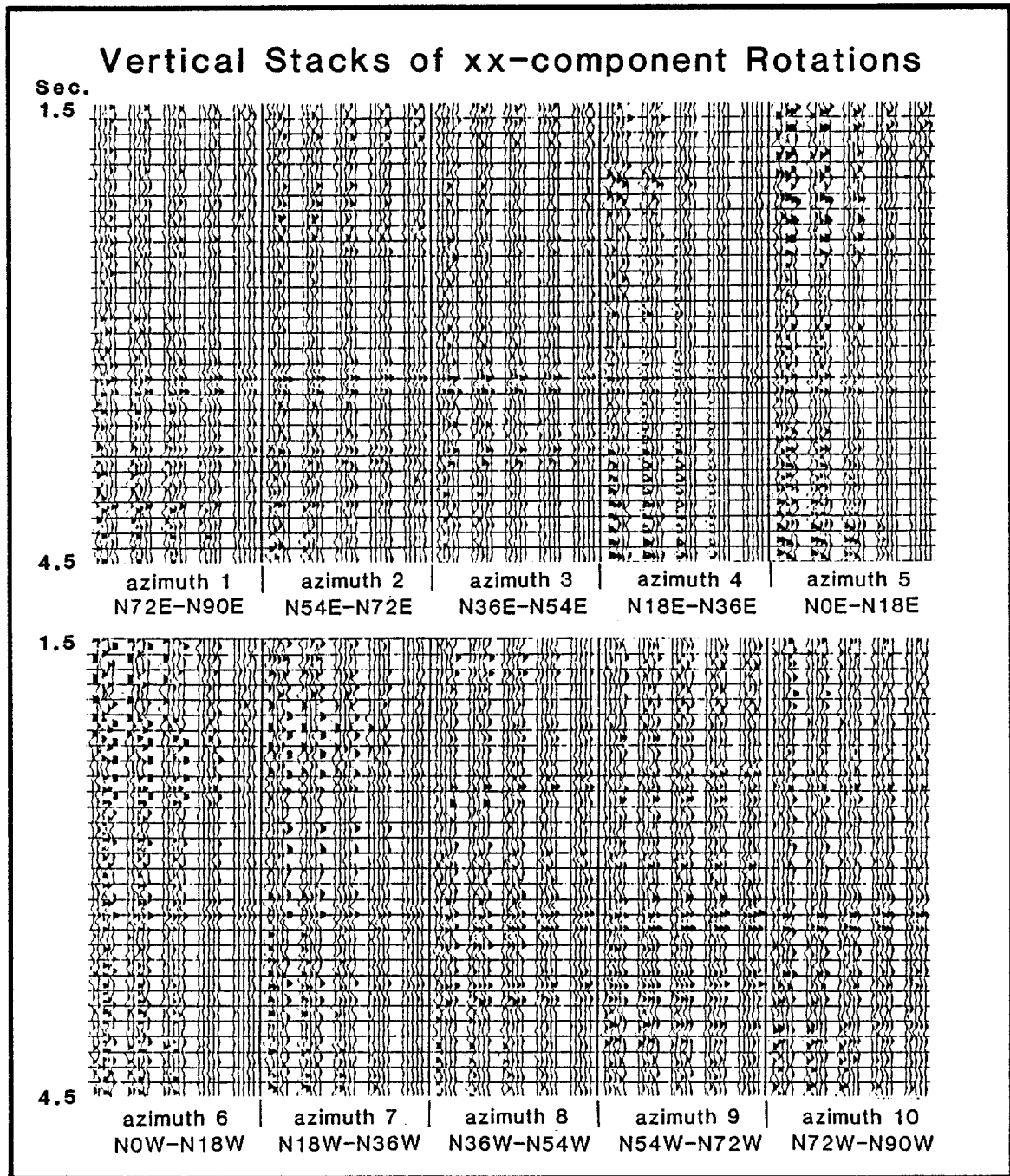


Figure 34. Vertical stacks of xx-component rotations for geophone line 6 (from Lewis, 1988).

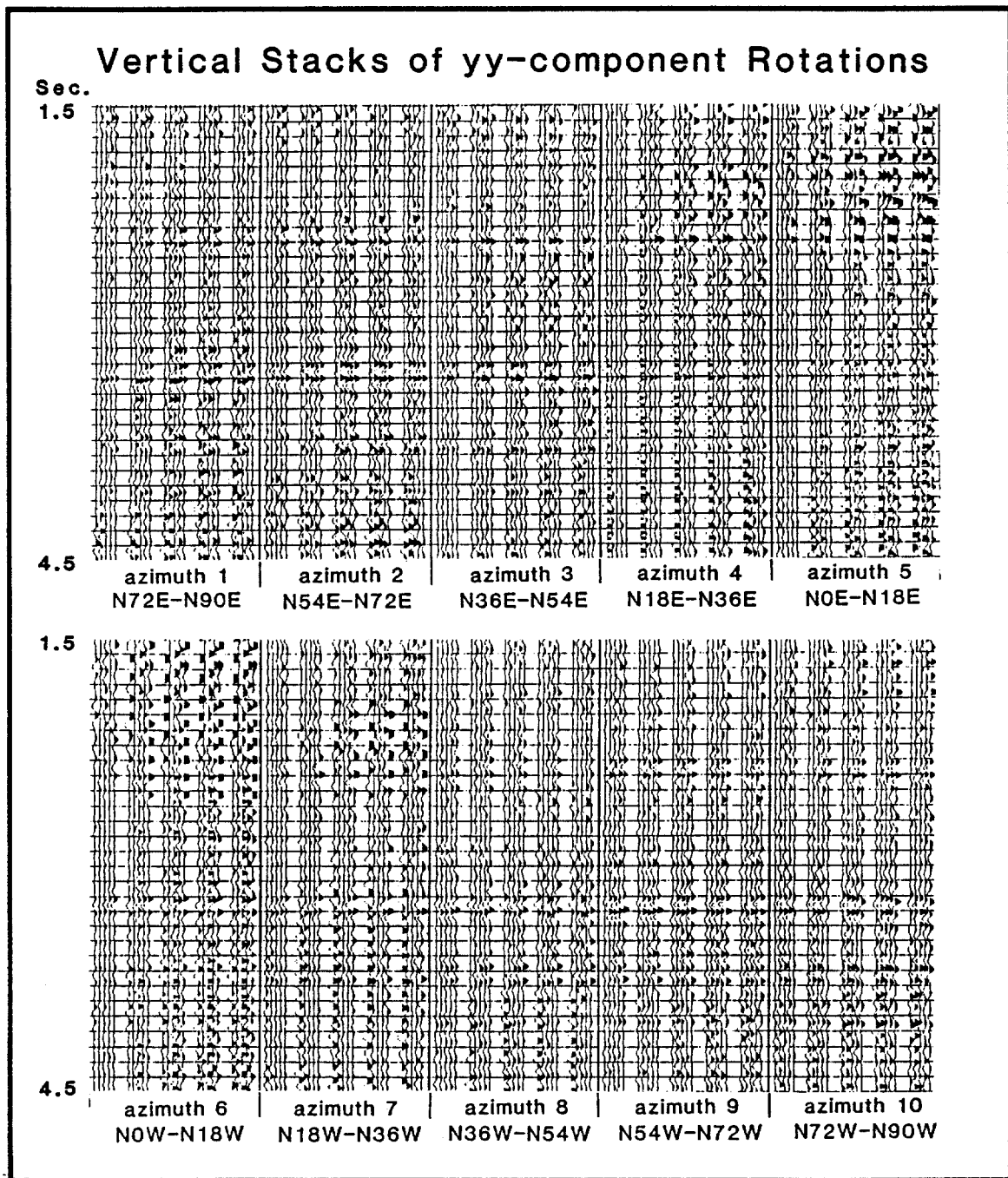


Figure 35. Vertical stacks of yy-component rotations for geophone line 6 (from Lewis, 1988).

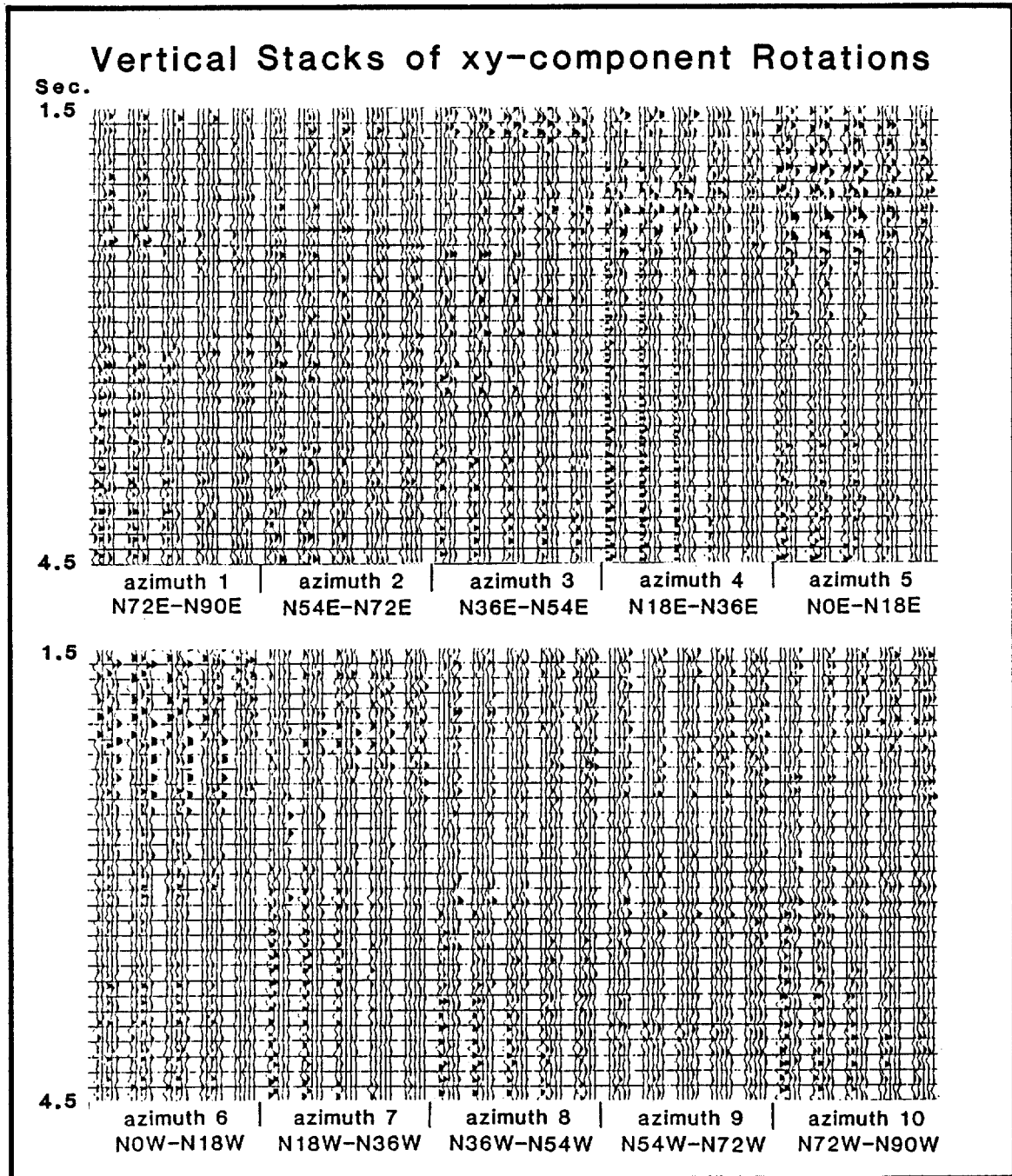


Figure 36. Vertical stacks of xy-component rotations for geophone line 6 (from Lewis, 1988).

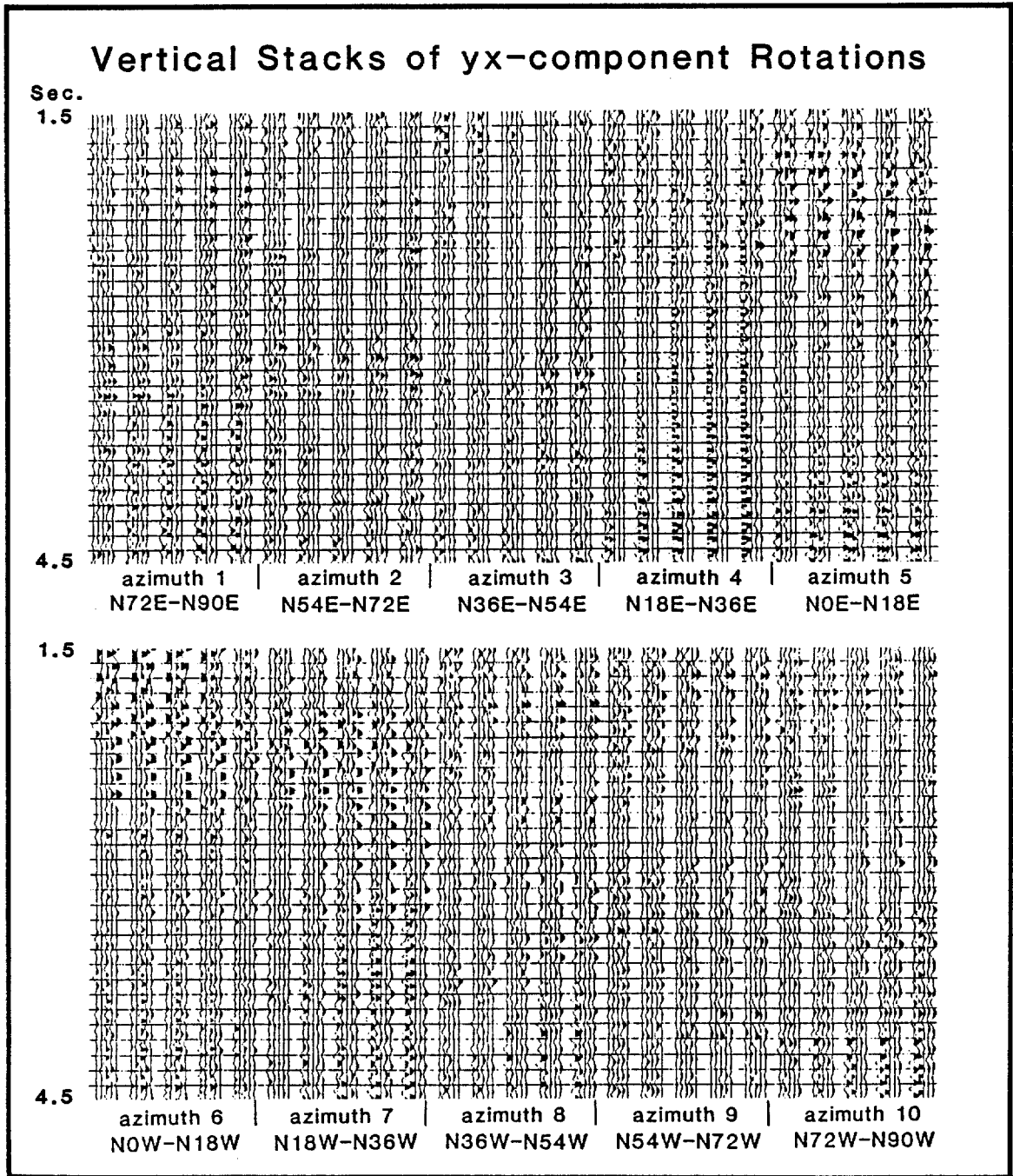


Figure 37. Vertical stacks of yx-component rotations for geophone line 6 (from Lewis, 1988).

because: 1.) The frequency content of the shear wave signal and the groundroll is similar. 2.) A frequency filter will affect some of the amplitudes which need to be preserved for rotation analysis.

A comparison of the yy' and xx' data sets shows that the yy' -component is the faster S1 split shear wave. Since the yy' -component is the faster arrival in all ten sectors, it can be concluded that the Silo Field doesn't exhibit an orthorhombic anisotropy pattern. If an orthorhombic pattern occurred, the xx' -component would be the faster S1 mode in a sector orthogonal to the sector where the yy' -component is the S1 mode.

A visual interpretation of these noisy data, for geophone line six, and for the other seven geophone lines (Figure 7), is quite cumbersome. Together there are five rotated displays per sector; ten sectors per line; eight lines; and four components, resulting in 1600 displays to interpret.

In order to reduce the time involved for the rotation analysis, I applied the four-component energy minimization algorithm to all 80 sectors (ten sectors times eight geophone lines) of the 3-D data. A time window ($3.1 < t < 3.5$ seconds) around a reflector in the Pierre Shale (Martin, 1987) was used because it included a coherent reflection and less groundroll than other time windows. A larger time window would have included more groundroll; a smaller window would not have smoothed out the errors due to random noise as effectively as this window. It was

assumed that the S1 and S2 polarization directions remain constant in an east-west direction along each geophone line. This assumption is probably valid since the rotation analysis results from the converted wave data set indicate a fairly constant S1 polarization direction over the 3-D grid area (Garotta and Granger, 1988). Therefore, only one rotation angle was calculated for each sector of each geophone line, resulting in 80 values of θ to interpret. The results of applying the algorithm are shown in Figure 38.

The S1 polarization directions shown in Figure 38 were calculated using the total energy of all five windowed traces in each sector. The S1 polarization directions corresponding to $\hat{\theta}$ (average of θ_i), calculated using the trace-by-trace variation of the energy minimization algorithm, are shown in Figure 39. Values of both $\hat{\theta}$ and $\hat{\sigma}$ (standard deviation) are listed in Appendix B. The random variation in the calculated S1 polarization direction is probably not due to the geology but to the groundroll and other noise in the data. The trace-by-trace algorithm appears to be slightly less affected by the noise than the total energy algorithm. Perhaps this is due to the fact that the total energy algorithm only involves one θ calculation; whereas the trace-by-trace algorithm involves a smoothing of several θ calculations. Both methods give inaccurate results when groundroll is present because high energy groundroll is probably not polarized in the S1 and S2 directions of the natural coordinate system.

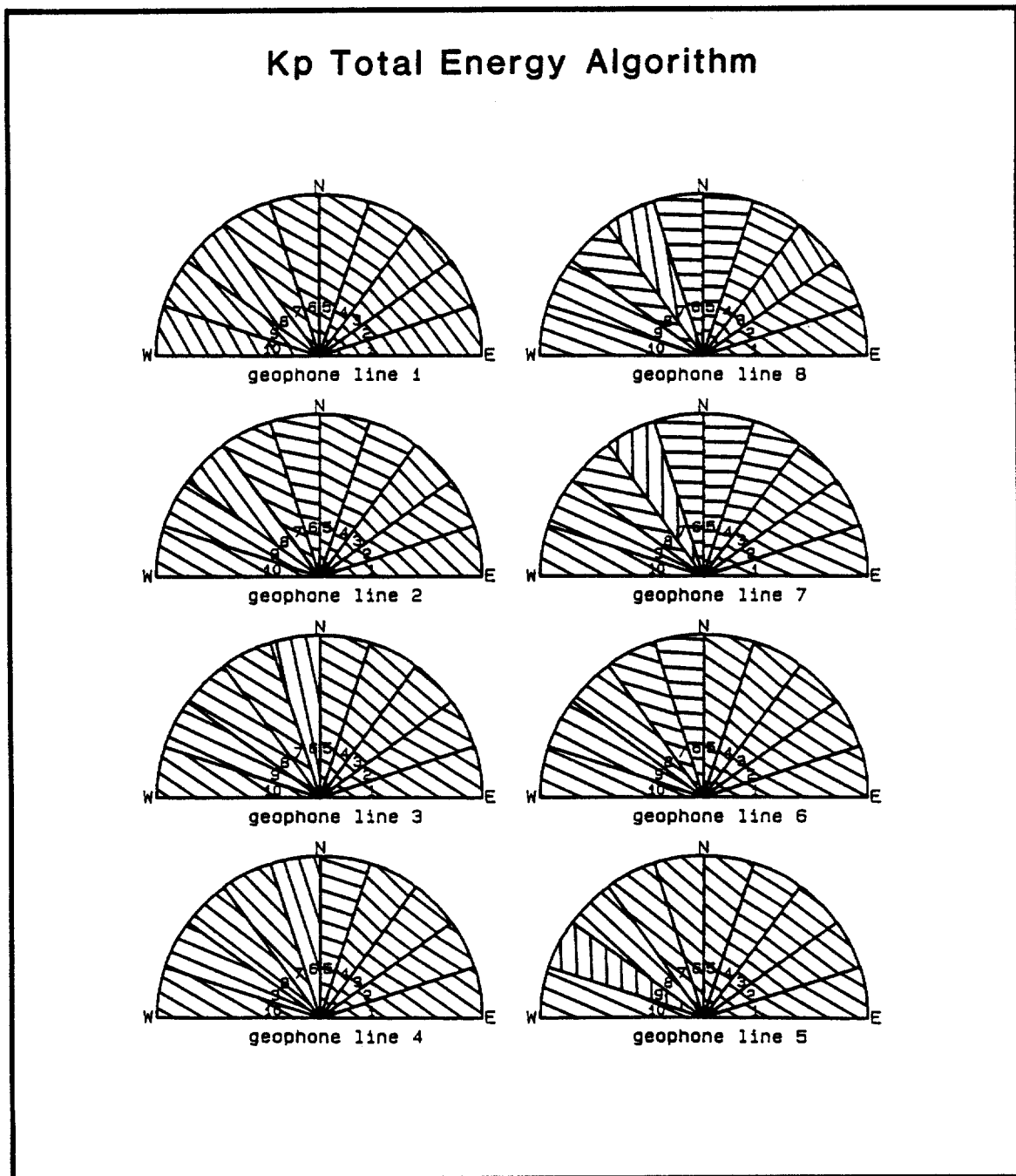


Figure 38. S1 polarization plots for Pierre (Kp) window ($3.1 < t < 3.5$ seconds), calculated using total energy minimization algorithm.

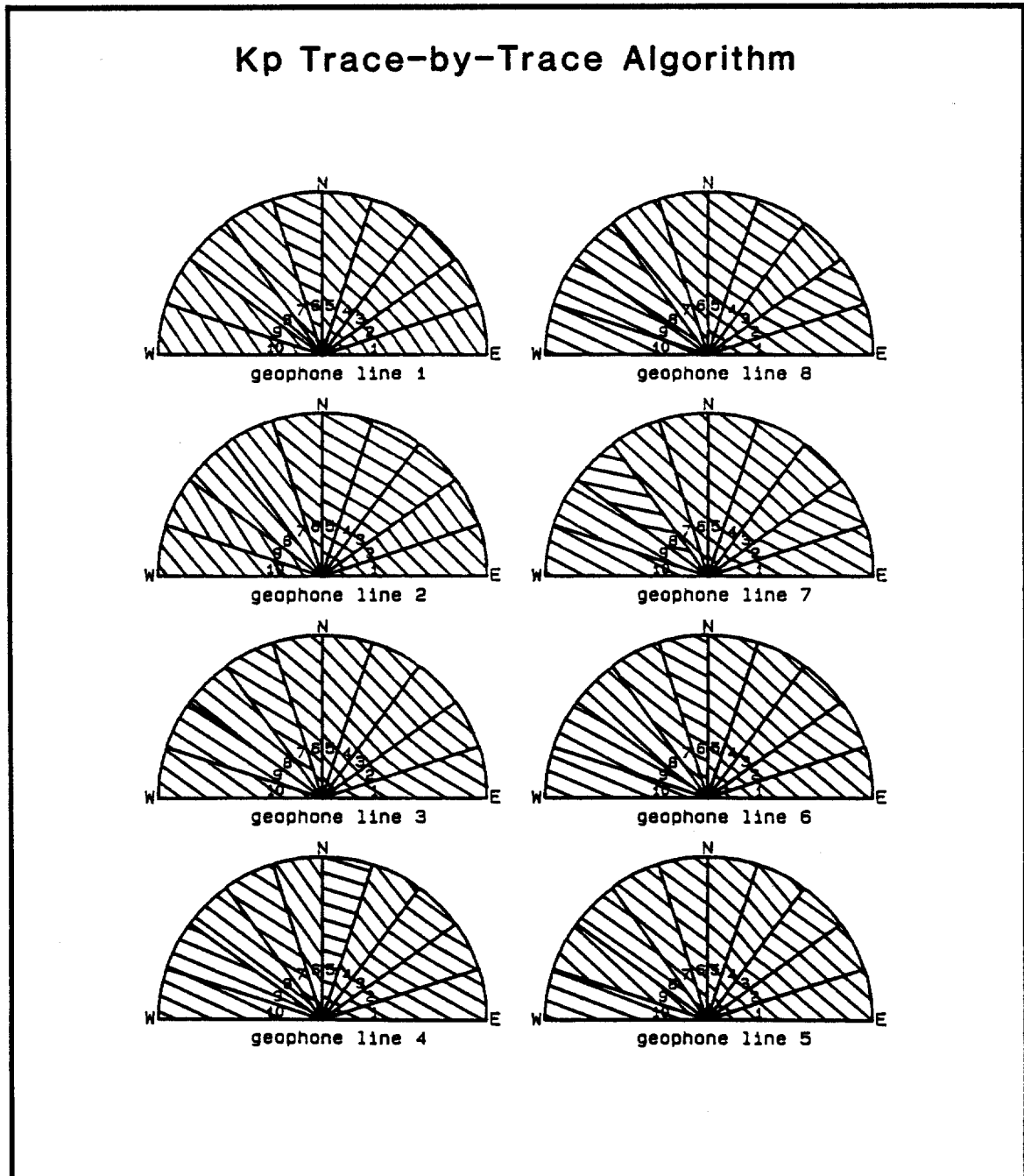


Figure 39. S1 polarization plots for Pierre (Kp) window ($3.1 < t < 3.5$ seconds), calculated using trace-by-trace energy minimization algorithm.

When groundroll is not present, $\hat{\sigma}$ in the trace-by-trace algorithm can be used as a guide to the quality of the calculated rotation angle, $\hat{\theta}$. On the other hand, when groundroll is present, $\hat{\sigma}$ can be deceptively low in value due to the coherency of the groundroll.

Figure 40 shows the calculated S1 polarization directions, using the trace-by-trace algorithm, for a window ($3.6 < t < 4.0$ seconds) around the Niobrara reflection (Martin, 1987). For low noise level sectors, the S1 polarization directions calculated from the Niobrara window agree closely with those calculated from the Pierre window. This is as expected since the shallowest anisotropic layer controls the final shear wave polarizations observed at the surface.

Figures 41-46 show windowed ($3.1 < t < 3.5$ seconds), unrotated and rotated geophone azimuth stacks for all the sectors of geophone lines four, five, and six. A counterclockwise 58° four-component rotation appears to have minimized the cross-component energy and maximized the principal component energy. The curves in Figure 47 show the ratio of the total principal component energy to the total cross-component energy, as a function of rotation angle, for the windowed ($3.1 < t < 3.5$ seconds) sectors of geophone line six. These curves illustrate the sensitivity of the energy minimization algorithm to the presence of groundroll.

The concentration of groundroll is highest in the north-south sectors because the geophone arrays were laid out in an east-west direction (Figure 8). Catherine

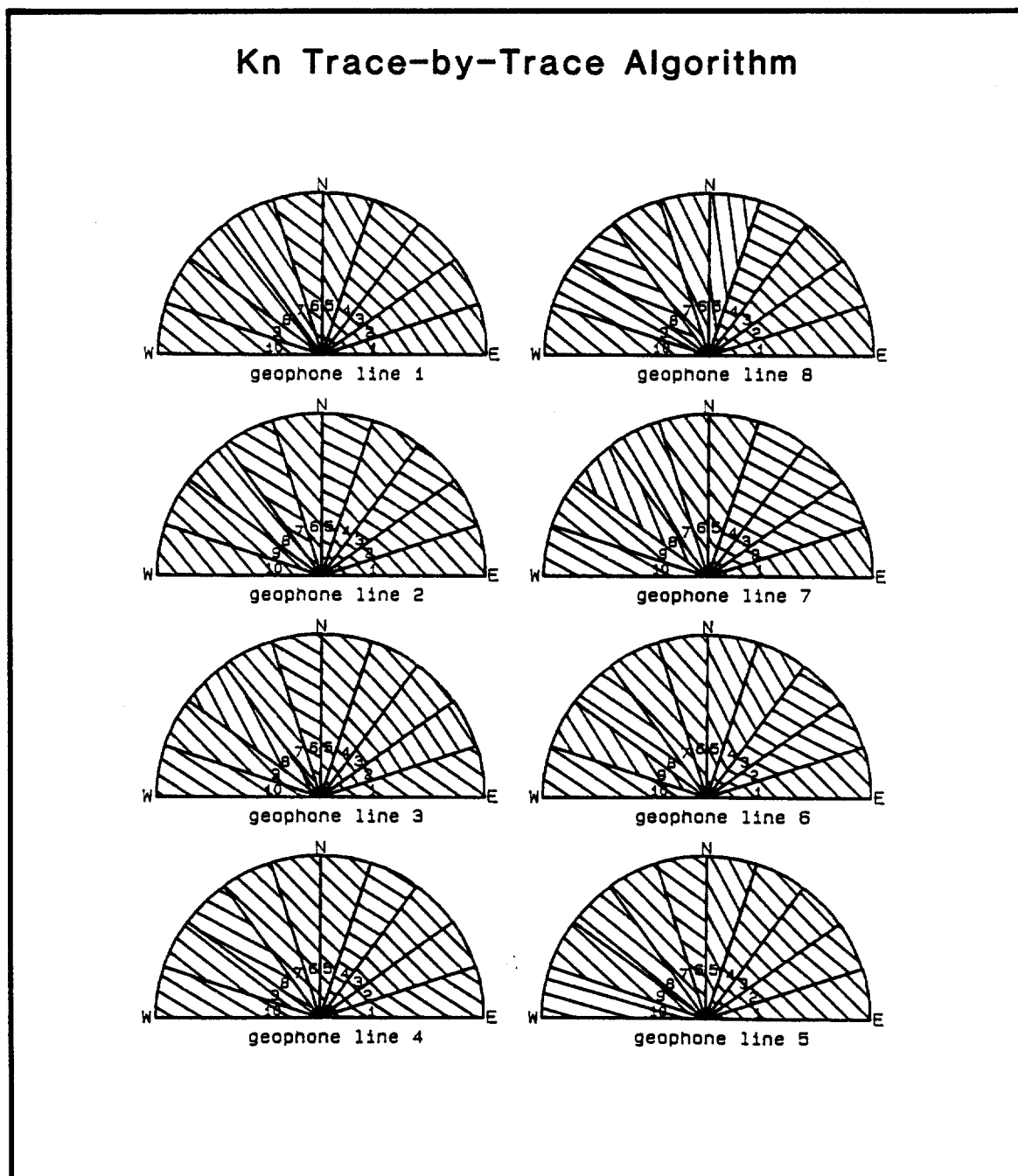


Figure 40. S1 polarization plots for Niobrara (Kn) window ($3.6 < t < 4.0$ seconds), calculated using trace-by-trace energy minimization algorithm.

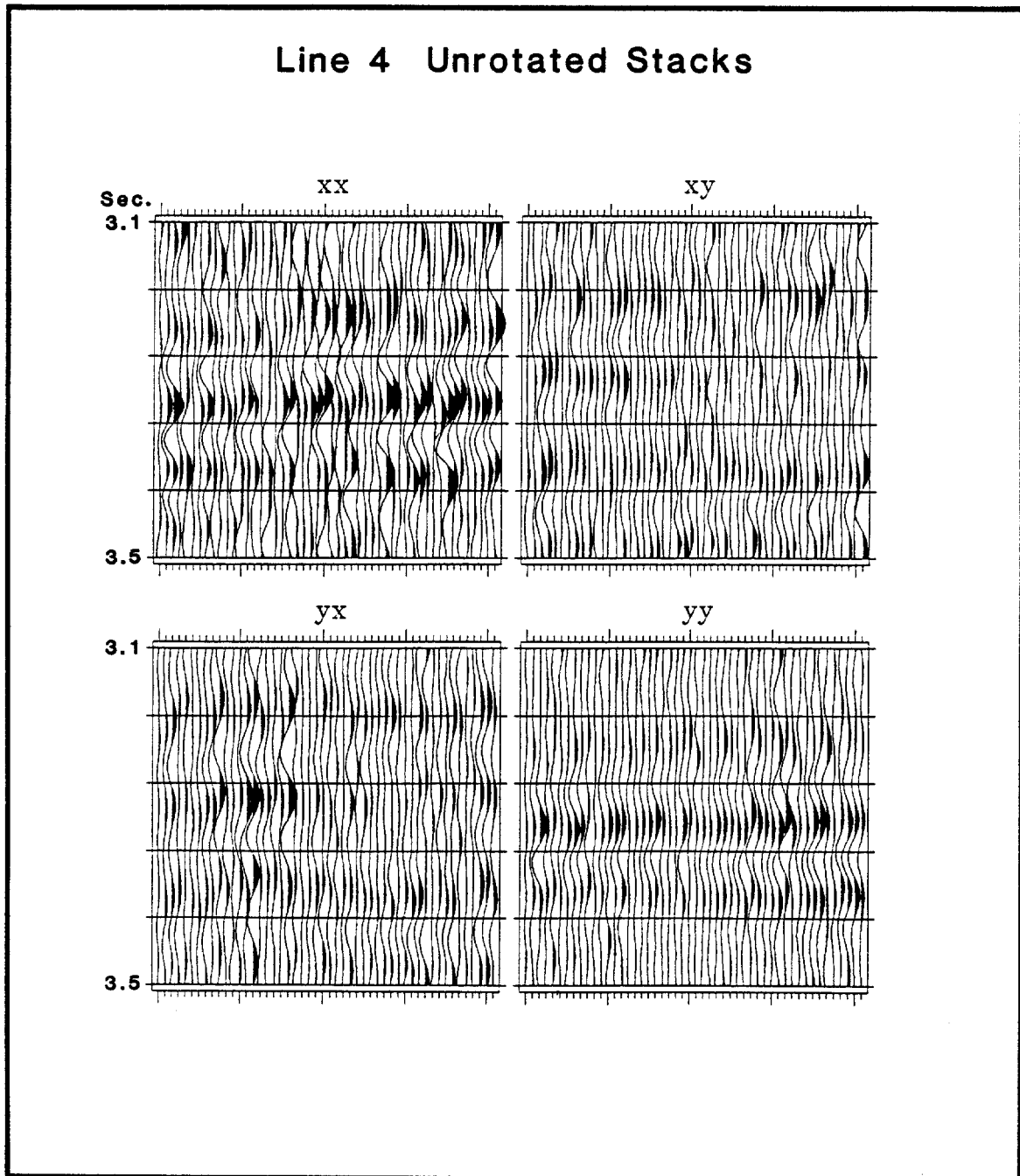


Figure 41. Unrotated geophone azimuth stacks for Pierre window of geophone line 4. Sectors 1-10 are displayed from left to right, for each component. There are 50 traces per component; 5 traces per sector.

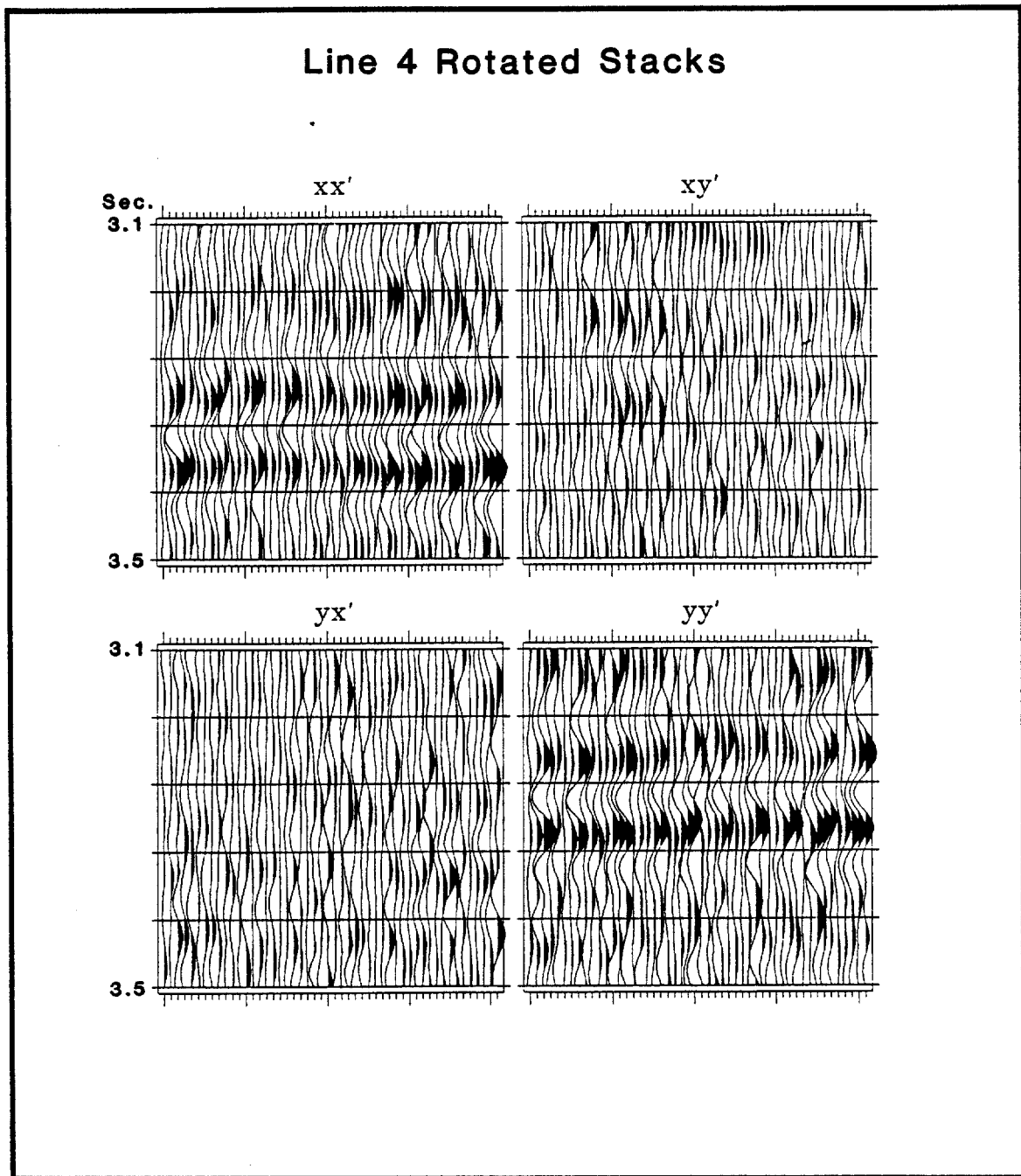


Figure 42. 58° rotated geophone azimuth stacks for Pierre window of geophone line 4. Sectors 1-10 are displayed from left to right, for each component. There are 50 traces per component; 5 traces per sector.

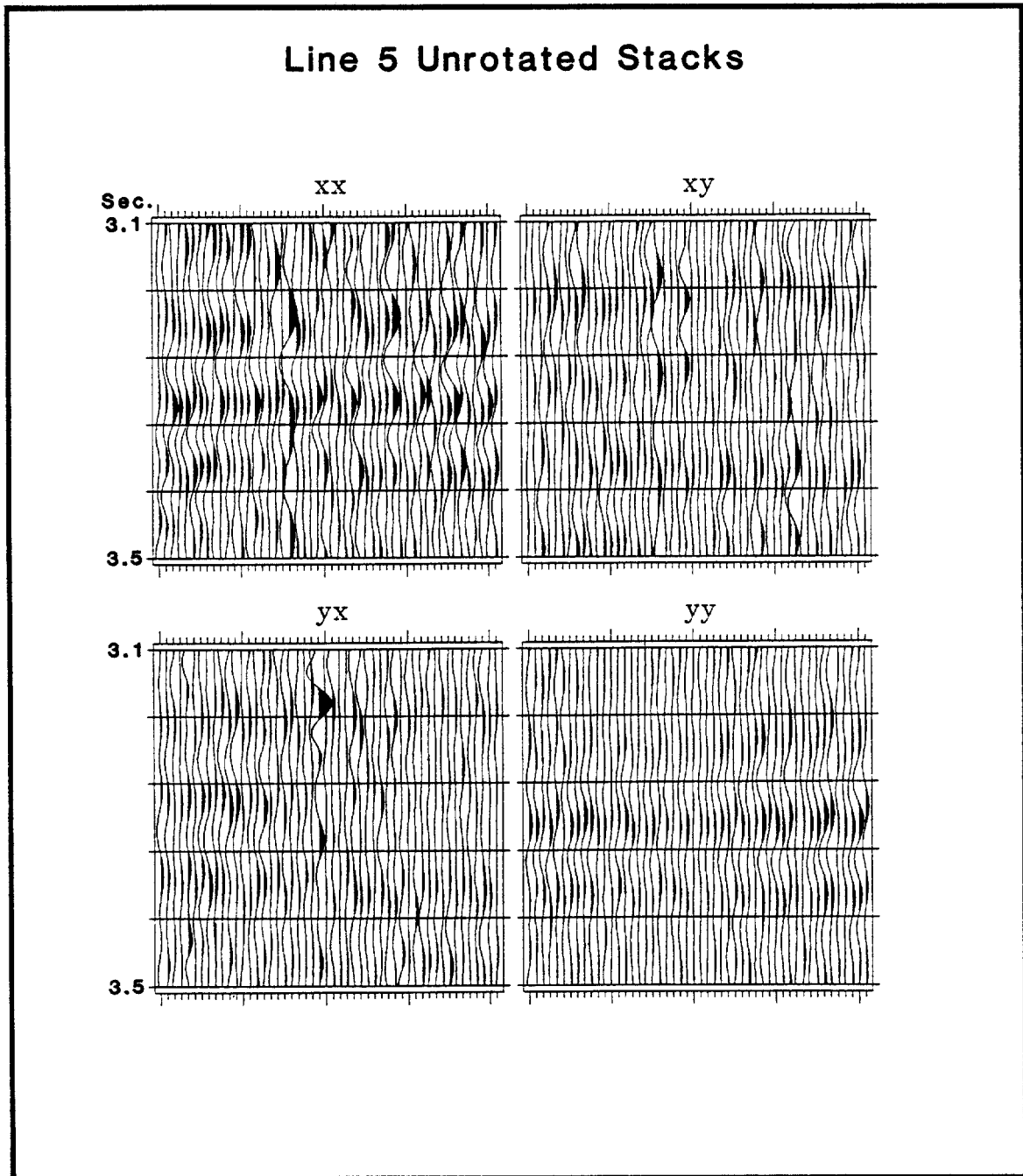


Figure 43. Unrotated geophone azimuth stacks for Pierre window of geophone line 5. Sectors 1-10 are displayed from left to right, for each component. There are 50 traces per component; 5 traces per sector.

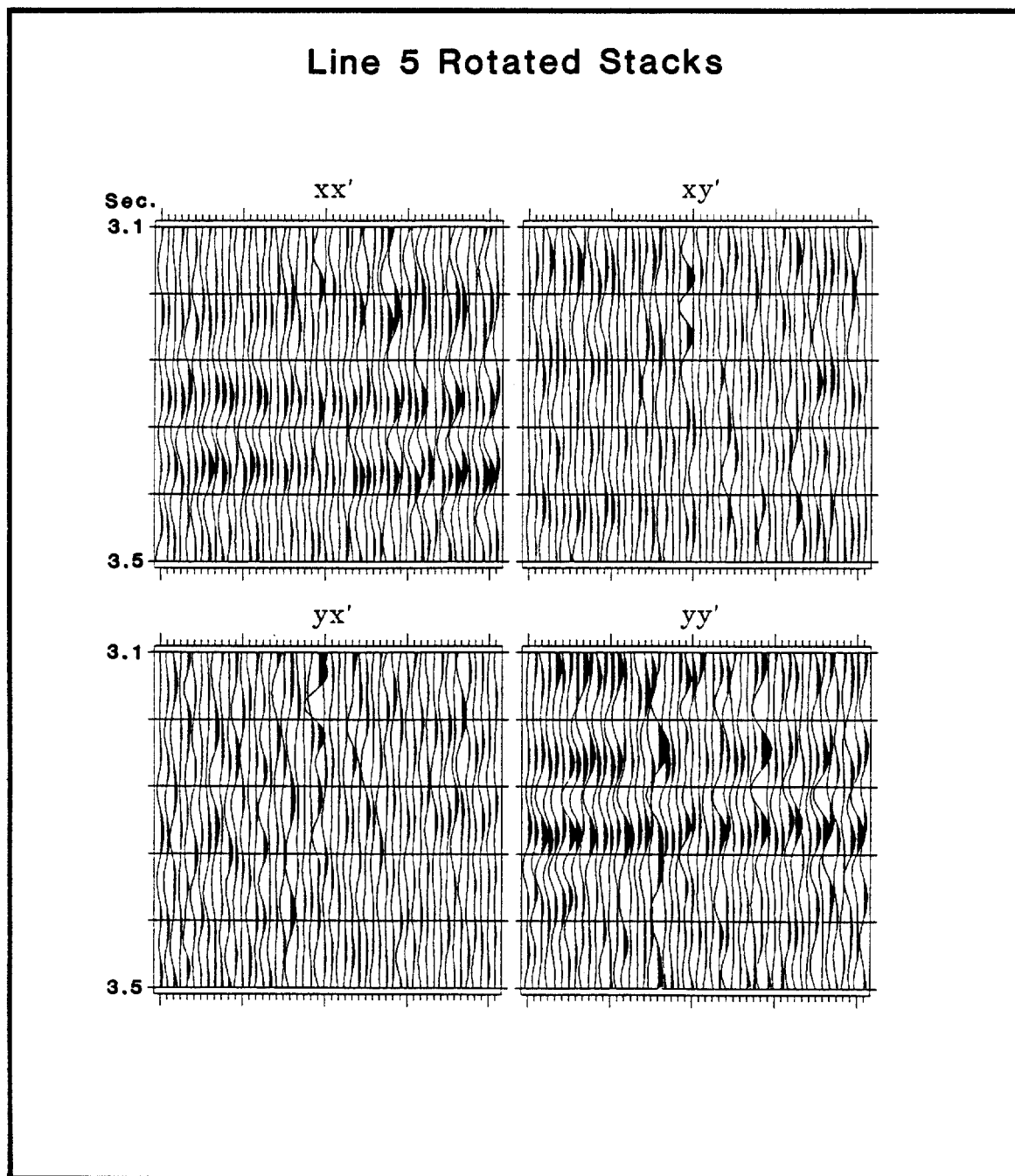


Figure 44. 58° rotated geophone azimuth stacks for Pierre window of geophone line 5. Sectors 1-10 are displayed from left to right, for each component. There are 50 traces per component; 5 traces per sector.

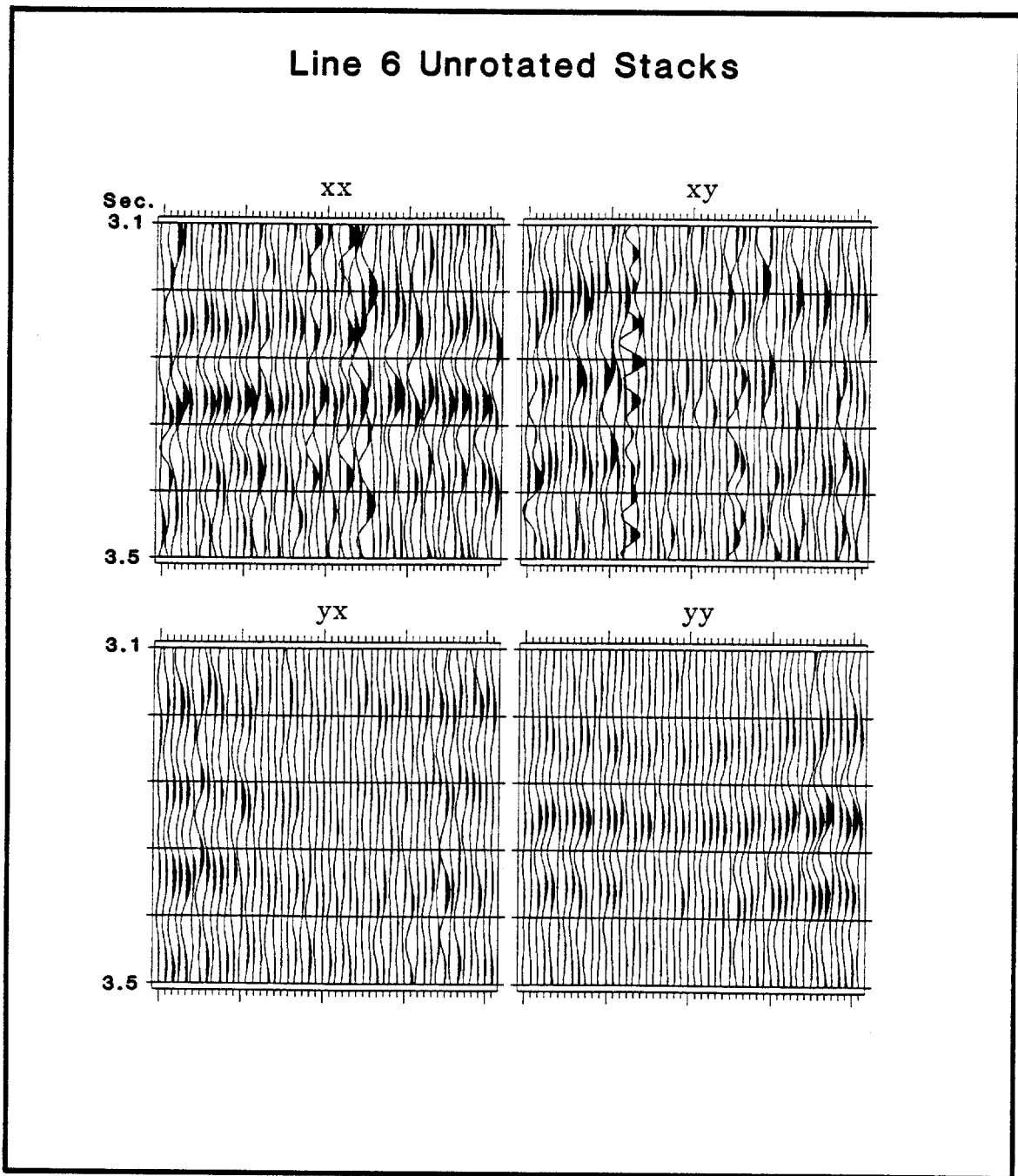


Figure 45. Unrotated geophone azimuth stacks for Pierre window of geophone line 6. Sectors 1-10 are displayed from left to right, for each component. There are 50 traces per component; 5 traces per sector.

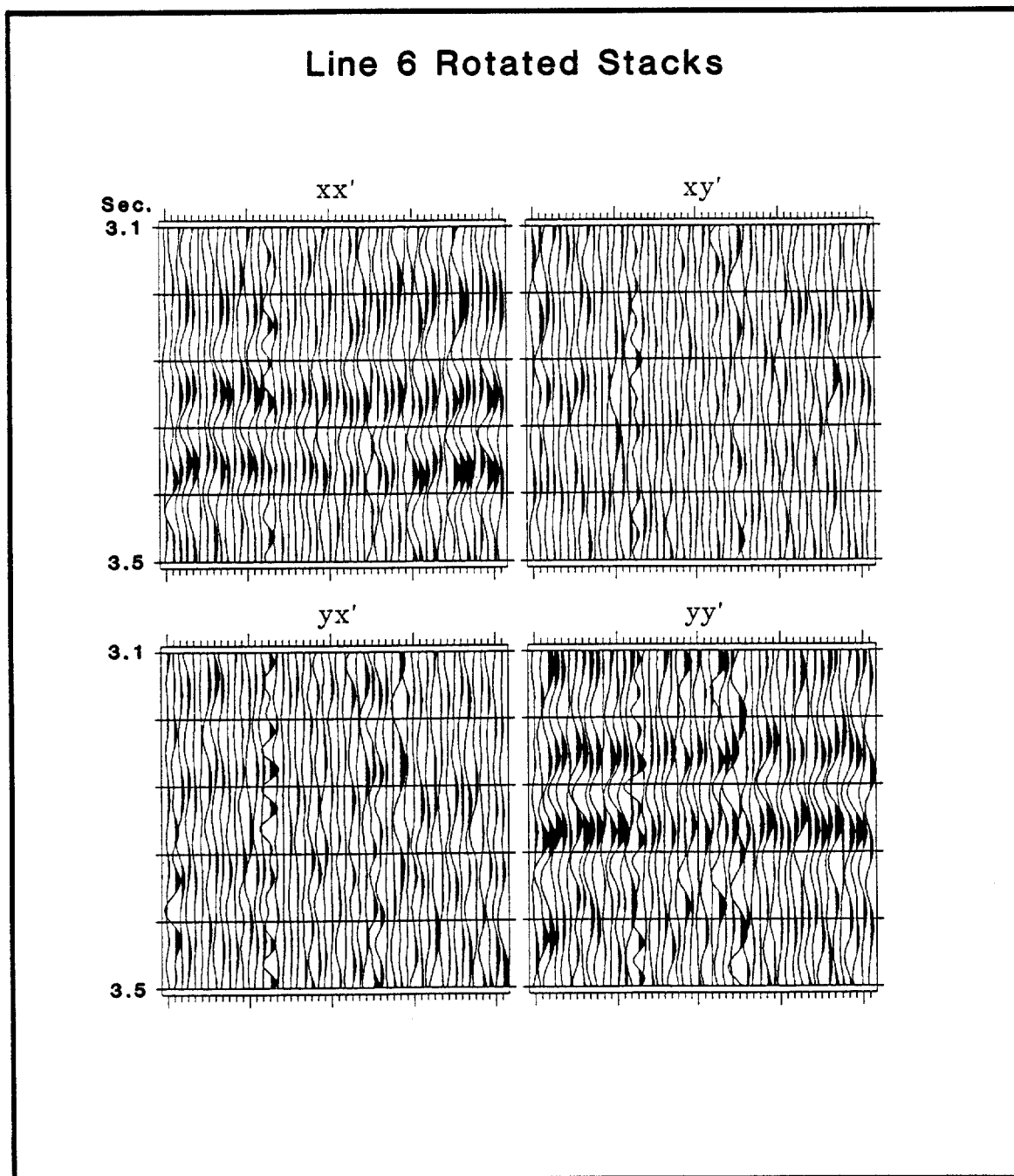


Figure 46. 58° rotated geophone azimuth stacks for Pierre window of geophone line 6. Sectors 1-10 are displayed from left to right, for each component. There are 50 traces per component; 5 traces per sector.

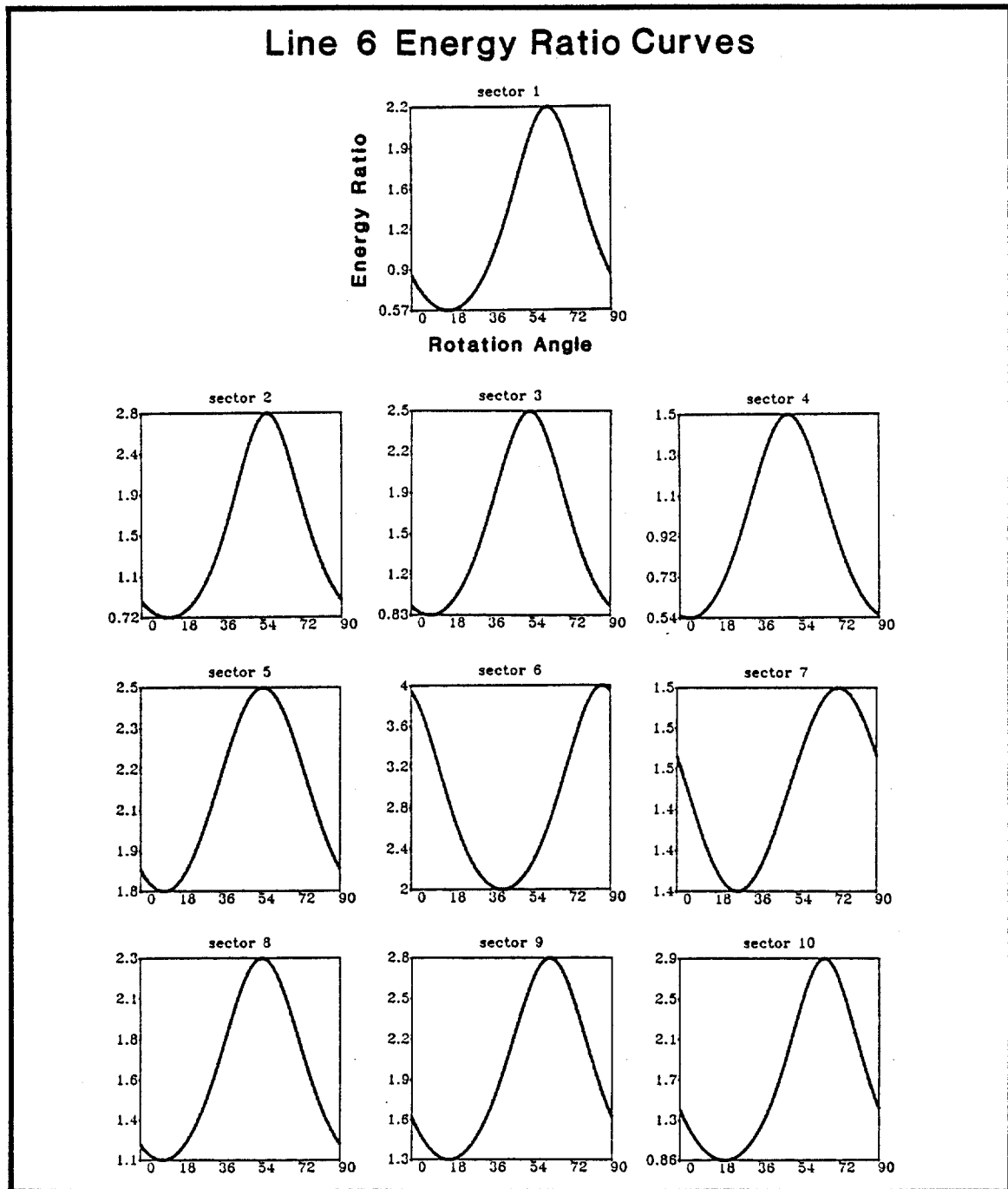


Figure 47. Energy ratio curves for geophone line 6. The ratio of the total principal component energy to the total cross-component energy, as a function of the rotation angle, is shown for all 10 sectors of geophone line 6. A window from 3.1 seconds to 3.5 seconds was used.

Lewis, a PhD student at Colorado School of Mines who is interpreting the Silo Field 3-D data, found only a few sectors in the data to be “trustworthy” (limited groundroll) for her interpretation. She used the results of applying the trace-by-trace variation of the energy minimization algorithm to the windowed Pierre ($3.1 < t < 3.5$ seconds) and Niobrara ($3.6 < t < 4.0$ seconds) sectors. The calculated S1 polarization directions for the sectors that she used varied by only a few degrees (noise level of the data). Lewis (personal communication) interpreted an S1 polarization direction of N 58° W for the entire 3-D grid area (see Figures 41-46). My own interpretation of the S1 polarization direction, based on examining the total energy minimization results of the Pierre sectors for geophone lines 4-6, agrees with Lewis’ result of N 58° W.

Hodograms corresponding to a windowed Pierre sector of geophone line 4 are shown in Figures 48-49. Some of these hodograms confirm the principal axes orientation calculated using the energy minimization algorithm. However, some of the hodograms are too noisy to interpret. Hodogram interpretation is not a robust procedure for determining the principal axes of vertically fractured media because hodograms contain information from only one source orientation. The energy minimization algorithm utilizes information from two orthogonal source orientations.

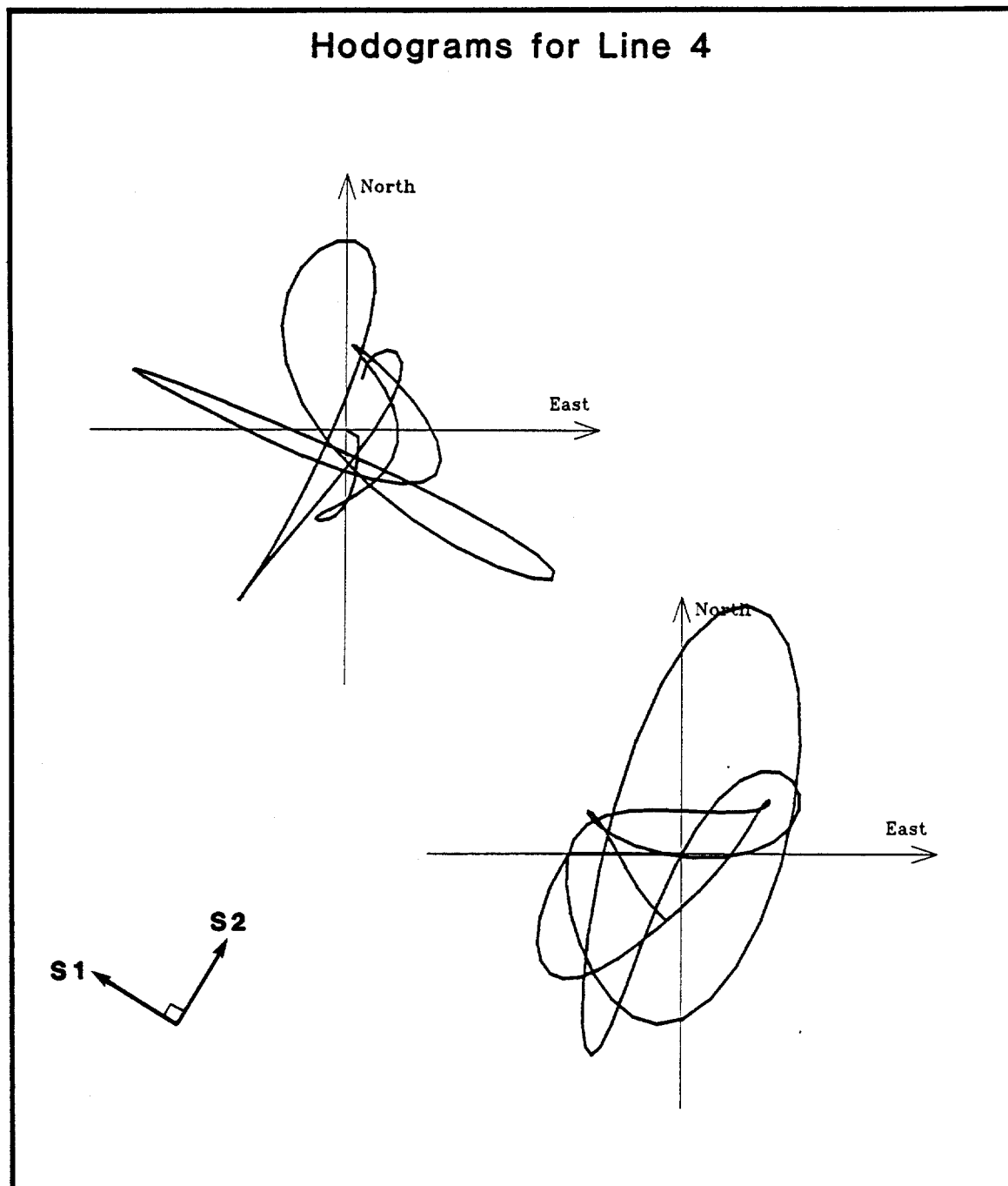


Figure 48. Hodograms for the x-component source (top) and y-component source (bottom) of trace 2 of sector 2 of geophone line 4. The window used was $3.1 < t < 3.5$ seconds.

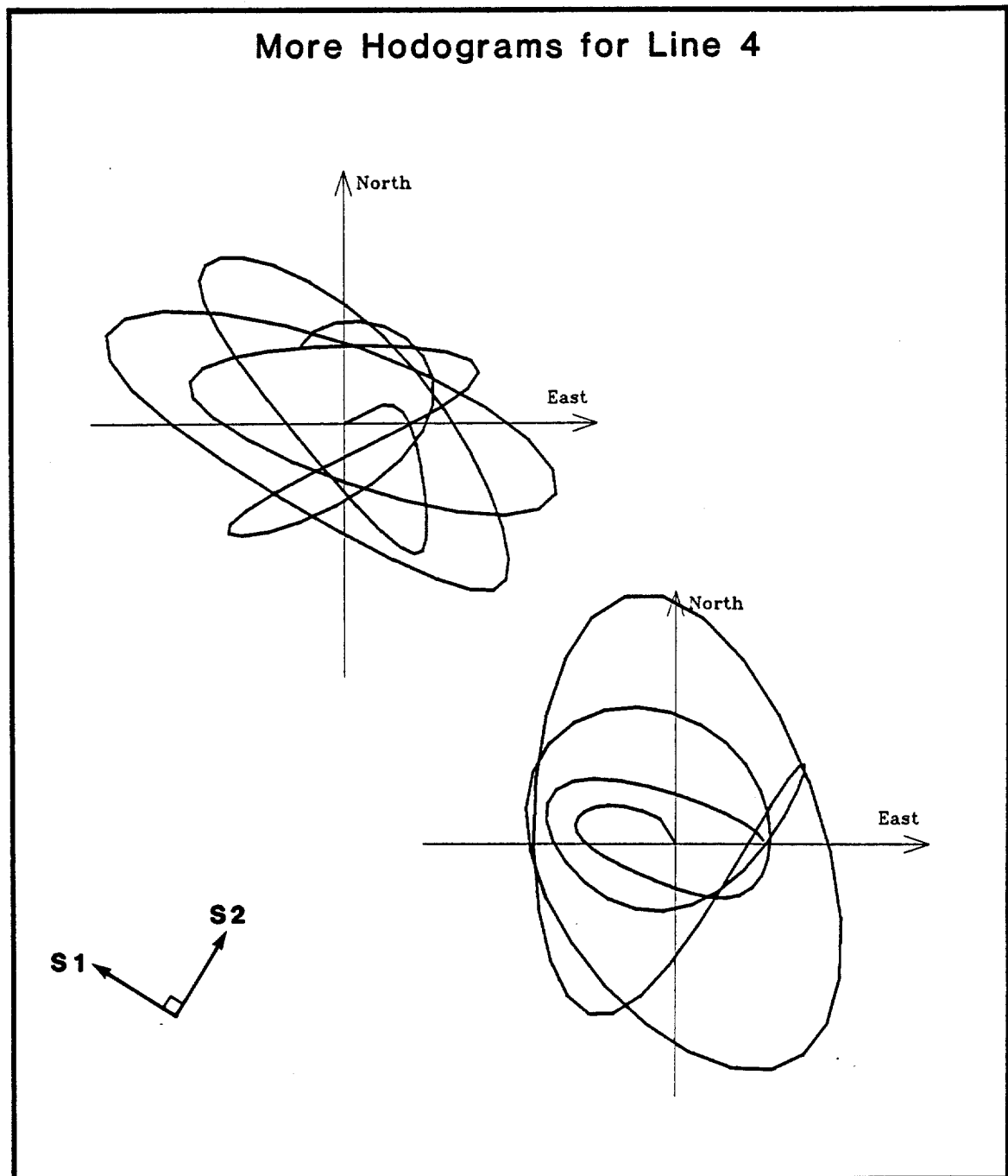


Figure 49. Hodograms for the x-component source (top) and y-component source (bottom) of trace 3 of sector 2 of geophone line 4. The window used was $3.1 < t < 3.5$ seconds.

The rotation analysis was performed on stacked data because the unstacked data were too noisy. After the rotation analysis the raw shot records (vertically stacked) were rotated into the natural coordinate system and a 74 millisecond gap deconvolution was applied. The converted wave statics were applied prior to the stacking process. The stacking process was repeated because velocity analyses and statics corrections are more accurate for the focussed S1- and S2-components than for the unfocussed data in the acquisition coordinate system. The effect of pre-stack rotation on S1- and S2-component CDP stacks, using the same velocity function to stack both components, is shown in Figure 50. Next separate velocity functions will be derived for the S1- and S2-components. After NMO, 3-D residual statics and a final pass of S1 and S2 velocity analyses will be performed to produce the final stacks.

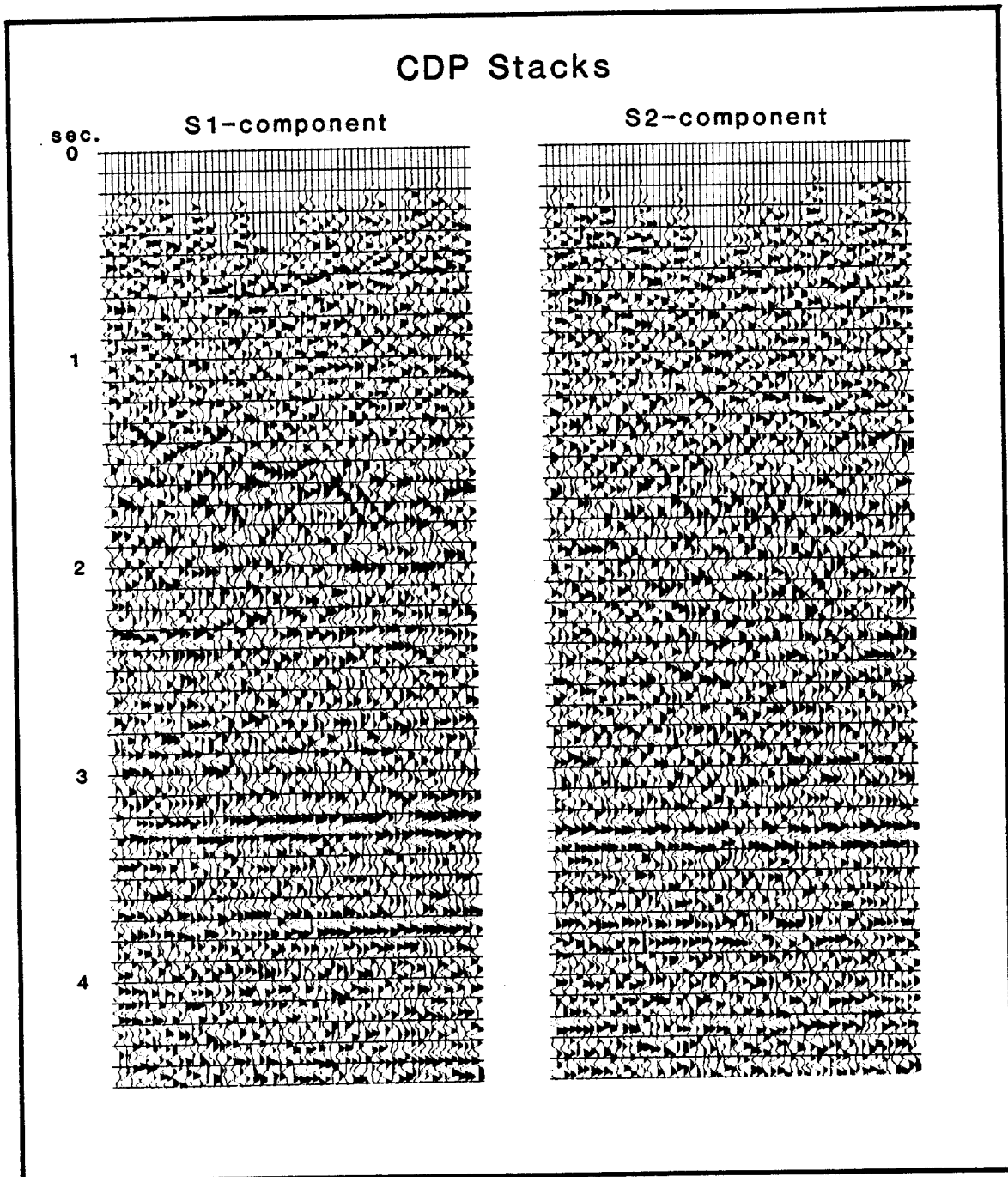


Figure 50. CDP line 94 stacks of S1- and S2-components. The same velocity function was used to stack both components.

FUTURE WORK

In this project, the source-receiver azimuth dependence of the shear wave polarization directions were studied. In the future, the source-receiver offset dependence of the shear wave polarization directions could be investigated (i.e. common offset stacks). According to Crampin (1989) shear waves "may suffer severe scattering at the free surface and by irregular topography within a wavelength or two of the recording site." Data corresponding to different source-receiver offsets will exhibit different scattering effects.

The acquisition of four-component shear wave VSP's, using oriented tools, would provide high-resolution information on any variation of the S1 polarization direction as a function of depth. The results of the rotation analysis from these VSP's could be compared with the surface seismic results.

Other four-component rotation algorithms could be developed and applied to the Silo Field data. The energy minimization algorithm is purely an amplitude analysis. Perhaps some approach could be developed that would examine the coherency of the principal components. When the coherency of the principal components is maximized, the data should be in the natural coordinate system.

For the rotation analysis in this project, it was assumed that the shear wave polarization directions remained constant in an east-west direction along each geophone line. In the future, a more comprehensive rotation analysis could be

performed to determine if there is some spatial variation in the S1 and S2 polarization directions along the geophone lines.

Another possibility for future study is the calculation of the combined 3-D source and receiver array response. If the 3-D array response were known for the entire Silo Field survey area, then perhaps some azimuth-dependent filter could be applied to the data to attenuate groundroll.

The energy minimization algorithm will determine the principal axes orientation for vertically fractured media. If the fractures are not vertical the energy minimization algorithm will give inaccurate results. If synthetic seismograms could be created corresponding to different fracture dips, then the rotation angle errors resulting from the application of the energy minimization algorithm could be quantified.

CONCLUSIONS

It can be concluded that the four-component energy minimization algorithm used in this rotation analysis is an effective, low-cost technique for determining shear wave polarization directions over a vertically fractured reservoir. The algorithm employed here, derived by Murtha (1988), is far less computer-intensive than performing four-component rotation for the 90 possible rotation angles. The algorithm also allows a precise determination of the rotation angle, to within the noise level of the data. Hodograms can also be used to calculate the principal axes orientation, albeit less robustly.

The effect of random noise, different x- and y-component source radiation patterns, or different x- and y-component geophone coupling on four-component rotation analysis is minimal. The calculated rotation angle for data which is contaminated by random noise, with a signal-to-noise ratio near two, has an error which is on the order of only a few degrees. Differences in source radiation patterns or geophone coupling also result in a rotation angle error of only a few degrees.

On the other hand, coherent noise such as groundroll can significantly degrade the quality of four-component rotation analysis. Because the presence of groundroll in the data can result in an error as high as $40^\circ - 45^\circ$, only sectors free of groundroll can be used in 3-D shear wave rotation analysis. Source and receiver

arrays for future 3-D shear wave surveys should be designed to attenuate groundroll in all sectors. Field tests should be conducted to test for the presence of groundroll in different source-receiver azimuths.

There are two main advantages to using source-receiver azimuth stacks for the rotation analysis of 3-D split shear wave data. First, if the rocks exhibit a pattern of orthorhombic anisotropy, then polarization information will not be lost due to the smearing of shear waves with different polarization directions. Second, if the shear wave data is contaminated with groundroll, then perhaps some sectors can be found that have no groundroll. If azimuth stacks are not used, it is impossible to avoid groundroll in the rotation analysis (i.e. frequency-domain filters can't be used in rotation analysis).

Finally, it can be concluded that at the survey location within the Silo Field the faster S1 split shear wave mode is polarized parallel to vertical fractures striking approximately N 58° W, for all source-receiver azimuths.

REFERENCES CITED

- Alford, R.M., 1986, Shear data in the presence of azimuthal anisotropy: Dilley, Texas: Presented at the 56th Annual SEG Meeting, Houston.
- Cameron, J., 1988, Shear waves in an anisotropic earth: Presented at the AAPG Meeting, Houston.
- Crampin, S., 1978, Seismic-wave propagation through a cracked solid: polarization as a possible dilatancy diagnostic: *Geophys. J.R. astr. Soc.*, v. 53, p. 467-496.
- Crampin, S., 1984, An introduction to wave propagation in anisotropic media: *Geophys. J.R. astr. Soc.*, 76, p. 17-28.
- Crampin, S., 1985, Evaluation of anisotropy by shear-wave splitting: *Geophysics*, v. 50, p. 142-152.
- Crampin, S., 1988, Nonparallel shear-wave polarizations in sedimentary basins: Presented at the 58th Annual SEG Meeting, Anaheim.
- Crampin, S., Liu, E., and Booth, D.C., 1989, Shear-wave splitting in cross-hole surveys: *Modelling: Geophysics*, v. 54, p. 57-65.
- Garotta, R. and P.Y. Granger, 1988, Silo Field II-Wyoming 3Cx3D project: CGG processing report of converted waves.
- Geoltrain, S., 1988, TRISO anisotropic modelling program, Center for Wave Phenomena, Colorado School of Mines, Golden, Colorado.
- Iverson, W.P., 1988, Reservoir characterization, Silo Field, Laramie County, Wyoming: University of Wyoming Report 1.
- Lewis, C., 1988, Azimuth dependence of shear wave polarizations and its application to rotation analysis in 3-D: Presented at Oct. 14 Silo II Consortium Meeting, Colorado School of Mines, Golden, Colorado.
- Love, A.E.H., 1944, *A Treatise on the Mathematical Theory of Elasticity* (4th ed.): Dover, New York, N.Y., 643 p.
- Lynn, H.B., and L.A. Thomsen, 1986, Shear wave exploration along the principal axis: Presented at the 56th Annual SEG Meeting, Houston.
- Martin, M.A., Davis, T.L., and O'Rourke, T.J., 1986, An integrated three-component approach to fracture detection: Presented at the 56th Annual SEG Meeting, Houston.
- Martin, M.A., and T.L. Davis, 1987, Shear-wave birefringence: A new tool for evaluating fractured reservoirs: *The Leading Edge*, v.6, p.22-28.

- Martin, M.A.**, 1987, Three-component seismic investigation of a fractured reservoir, Silo Field, Wyoming: Phd Thesis, Colorado School of Mines, T-3339, 99p.
- Murtha, P.E.**, 1988, Estimation of the rotation transformation angle for shear wave data acquired in azimuthally anisotropic regions: Presented at the AGU/SEG Chapman Conference on Seismic Anisotropy of the Earth's Crust, Berkeley, California.
- Naville, C.**, 1986, Detection of anisotropy using shear-wave splitting in VSP surveys: Requirements and applications: Presented at the 56th Annual SEG Meeting, Houston.
- Robertson, J.D. and D. Corrigan**, 1983, Radiation patterns of a shear-wave vibrator in near-surface shale: *Geophysics*, v.48, p.19-26.
- Stoneley, R.**, 1949, The seismological implications of aeolotropy in continental structure: *Monthly Notices, Royal Astronomical Society, Geophys. Suppl.*, v. 5, p. 343-353.
- Thomsen, L.A.**, 1986, Reflection seismology in azimuthally anisotropic media: Presented at the 56th Annual SEG Meeting, Houston.
- Thomsen, L.A.**, 1988, Reflection seismology over azimuthally anisotropic media: *Geophysics*, v. 53, p. 304-313.
- Vuillermoz, C., Chitwood, D., Bailey, W., and Wu, C.**, 1988, Reservoir Characterization Project - CGG second report - October 14, 1988.
- White, J.E. and F.A. Angona**, 1955, Elastic wave velocities in laminated media: *Jour. Acoust. Soc. Am.*, v. 27, p. 310-317.
- Willis, H., Rethford, G., and Bielanski, E.**, 1986, Azimuthal anisotropy: The occurrence and effect on shear wave data quality: Presented at the 56th Annual SEG Meeting, Houston.

APPENDIX A

Derivation of Four-Component Energy Minimization Algorithm

Let i be the trace index and j be the time sample index.

The rotated cross-components for the i th trace and j th sample are:

$$xy'(i,j) = xy(i,j)\cos^2\theta - xx(i,j)\sin\theta\cos\theta + yy(i,j)\sin\theta\cos\theta - yx(i,j)\sin^2\theta$$

$$yx'(i,j) = yx(i,j)\cos^2\theta - xx(i,j)\sin\theta\cos\theta + yy(i,j)\sin\theta\cos\theta - xy(i,j)\sin^2\theta.$$

Let the space-time window be represented by traces 1- m , and time samples 1- n .

1.) Set the derivative of the cross-component energy equal to zero

$$\frac{\partial}{\partial\theta} \left[\sum_{i=1}^m \sum_{j=1}^n (yx'(i,j)^2 + xy'(i,j)^2) \right] = 0$$

2.) Pull summations out of derivative expression

$$\sum_{i=1}^m \sum_{j=1}^n \left[2yx'(i,j) \frac{\partial}{\partial\theta} yx'(i,j) + 2xy'(i,j) \frac{\partial}{\partial\theta} xy'(i,j) \right] = 0$$

3.) For clarity, drop summation signs and i, j variables until end of derivation

$$2yx' \frac{\partial}{\partial \theta} yx' + 2xy' \frac{\partial}{\partial \theta} xy' = 0$$

4.) Simplify

$$yx' \left[(xx - yy)\cos 2\theta + (xy + yx)\sin 2\theta \right] + xy' \left[(xx - yy)\cos 2\theta + (xy + yx)\sin 2\theta \right] = 0$$

5.) Simplify

$$\left[(yy - xx)\sin 2\theta + (xy + yx)\cos 2\theta \right] \left[(xy + yx)\sin 2\theta + (xx - yy)\cos 2\theta \right] = 0$$

6.) Simplify

$$(xx - yy)(xy + yx)\cos 4\theta + \left[(xy + yx)^2 - (xx - yy)^2 \right] \frac{1}{2}\sin 4\theta = 0$$

7.) Simplify and bring back i, j variables

$$\tan 4\theta = \frac{A}{B}$$

where

$$A = xx(i, j)yx(i, j) - xy(i, j)yy(i, j) - yx(i, j)yy(i, j) + xx(i, j)xy(i, j)$$

$$B = \frac{1}{2} \left[xx(i, j)^2 - xy(i, j)^2 - yx(i, j)^2 + yy(i, j)^2 \right] - \left[xx(i, j)yy(i, j) + xy(i, j)yx(i, j) \right]$$

8.) Bring summation signs back and solve for θ

$$\theta = \frac{1}{4} \tan^{-1} \left[\frac{\sum_{i=1}^m \sum_{j=1}^n A}{\sum_{i=1}^m \sum_{j=1}^n B} \right]$$

APPENDIX B

Rotation Analysis Results (in degrees measured counterclockwise from east)

S1 Polarization Directions for Pierre Interval
Using Total Energy Minimization Algorithmwindow used for analysis: $3.1 < t < 3.5$ seconds

	sector									
	1	2	3	4	5	6	7	8	9	10
line 1										
S1 direction	126	133	130	145	147	151	144	125	131	119
line 2										
S1 direction	136	147	133	155	152	168	154	126	149	150
line 3										
S1 direction	148	151	140	139	151	102	148	150	155	146
line 4										
S1 direction	145	148	143	136	162	108	134	142	157	150
line 5										
S1 direction	150	143	143	148	141	139	142	137	92	156
line 6										
S1 direction	152	147	144	139	146	176	163	145	152	155
line 7										
S1 direction	156	151	146	169	179	178	91	168	155	151
line 8										
S1 direction	144	150	122	154	177	178	99	173	155	159

S1 Polarization Directions for Pierre Interval Using Trace-by-trace Energy Minimization Algorithm

window used for analysis: $3.1 < t < 3.5$ seconds

	sector									
	1	2	3	4	5	6	7	8	9	10
line 1										
S1 direction	124	132	133	139	133	154	137	140	129	124
standard deviation	10.0	11.7	17.4	24.0	26.2	14.8	19.1	19.7	13.2	16.2
line 2										
S1 direction	135	127	144	150	150	140	128	132	122	130
standard deviation	3.7	27.5	17.9	20.6	9.4	32.5	28.0	28.7	23.0	25.2
line 3										
S1 direction	149	141	133	133	133	140	149	141	157	134
standard deviation	14.0	17.1	8.8	22.9	22.7	33.0	15.5	24.8	15.4	24.5
line 4										
S1 direction	151	150	144	128	163	125	148	143	157	155
standard deviation	14.8	6.3	6.9	16.4	15.0	24.7	18.5	12.6	9.6	13.2
line 5										
S1 direction	139	137	144	130	138	144	142	145	137	159
standard deviation	23.9	21.5	9.2	26.5	24.2	12.6	12.6	16.2	33.5	8.8

**S1 Polarization Directions for Pierre Interval Using
Trace-by-trace Energy Minimization Algorithm
(continued)**

	sector									
	1	2	3	4	5	6	7	8	9	10
line 6										
S1 direction	139	144	137	136	142	152	142	137	152	157
standard deviation	24.7	6.2	18.5	15.4	19.8	27.0	19.7	23.0	16.4	8.3
line 7										
S1 direction	150	154	137	142	142	139	138	168	150	152
standard deviation	12.5	15.4	23.7	28.9	42.5	40.8	38.9	8.4	13.3	6.6
line 8										
S1 direction	144	152	131	147	143	138	130	147	155	155
standard deviation	17.3	9.3	18.0	14.6	37.7	40.3	40.1	31.3	13.5	20.4

**S1 Polarization Directions for Niobrara Interval
Using Total Energy Minimization Algorithm**

window used for analysis: $3.6 < t < 4.0$ seconds

	sector									
	1	2	3	4	5	6	7	8	9	10
line 1										
S1 direction	125	134	139	140	115	173	176	136	126	118
line 2										
S1 direction	135	148	174	144	164	94	148	149	138	100
line 3										
S1 direction	148	133	131	142	101	91	114	138	115	140
line 4										
S1 direction	147	131	143	151	173	180	137	144	164	153
line 5										
S1 direction	134	144	138	121	119	147	135	138	159	164
line 6										
S1 direction	148	152	156	134	91	176	168	151	146	160
line 7										
S1 direction	96	162	156	172	90	93	91	97	165	147
line 8										
S1 direction	176	153	127	158	98	104	92	170	166	164

S1 Polarization Directions for Niobrara Interval Using Trace-by-trace Energy Minimization Algorithm

window used for analysis: $3.6 < t < 4.0$ seconds

	sector									
	1	2	3	4	5	6	7	8	9	10
line 1										
S1 direction	125	130	136	138	120	143	123	128	133	141
standard deviation	10.4	10.5	24.1	13.7	30.9	27.1	37.0	18.9	17.9	26.7
line 2										
S1 direction	132	141	148	132	153	132	149	130	137	129
standard deviation	16.9	18.2	25.7	18.7	30.3	43.5	18.0	35.3	11.3	32.1
line 3										
S1 direction	145	123	129	133	135	150	131	117	134	147
standard deviation	12.5	16.4	3.7	27.5	24.3	36.9	19.3	22.8	30.7	24.9
line 4										
S1 direction	147	135	134	148	136	134	137	152	142	149
standard deviation	18.4	19.7	22.7	14.6	31.5	38.6	29.7	15.8	26.6	11.7
line 5										
S1 direction	135	140	134	133	118	144	135	141	137	164
standard deviation	16.8	23.3	19.5	20.8	20.0	22.1	13.9	25.0	33.3	8.5

S1 Polarization Directions for Niobrara Interval Using
Trace-by-trace Energy Minimization Algorithm
(continued)

	sector									
	1	2	3	4	5	6	7	8	9	10
line 6										
S1 direction	135	153	150	120	117	132	134	146	122	146
standard deviation	23.6	6.9	18.7	18.6	34.0	35.1	21.1	16.1	27.1	21.8
line 7										
S1 direction	126	154	152	152	128	126	120	112	140	151
standard deviation	28.3	18.2	22.0	31.7	42.7	39.8	33.6	25.2	30.6	17.1
line 8										
S1 direction	131	137	134	153	98	116	134	159	151	140
standard deviation	24.7	27.6	23.4	10.6	6.1	33.9	40.3	19.6	31.3	34.2

APPENDIX C

Program Listings

```
**** This program calculates rotation angles for different
**** sectors.
**** The total cross-component energy (every sample
**** of every trace) is minimized.
**** The algorithm was derived by Patricia Murtha (1988).
```

```
      real s11(400,625),s12(400,625),s21(400,625),
& s22(400,625),num,nsam

      parameter(pi=3.14159265)

      write(6,*) 'enter number of sectors'

      read(5,*) nsect

      write(6,*) 'enter number of traces per sector, and
& samples per trace'

      read(5,*) ntsect,nsamp

      ntrace= ntsect*nsect

      open(unit=1,file='s11.dat',form='unformatted',
& status='unknown')

      open(unit=2,file='s12.dat',form='unformatted',
& status='unknown')

      open(unit=3,file='s21.dat',form='unformatted',
& status='unknown')

      open(unit=4,file='s22.dat',form='unformatted',
& status='unknown')

      open(unit=7,file='ang.dat',status='unknown')

      do 10 i=1, ntrace

      read(1) (s11(i,j), j=1,nsamp)

      read(2) (s12(i,j), j=1,nsamp)

      read(3) (s21(i,j), j=1,nsamp)

      read(4) (s22(i,j), j=1,nsamp)

10      continue

      write(7,*) 'sector, theta'

      write(7,*)

      do 60 l=1,nsect
```

```
nbegin= (1-1)*ntsect
tnum= 0.
tden= 0.

do 30 m=1,ntsect
i= m+nbegin
nsum= 0.
dsum= 0.

do 20 j=1,nsamp
v11= s11(i,j)
v12= s12(i,j)
v21= s21(i,j)
v22= s22(i,j)

num= (v11*v21- v12*v22- v21*v22+ v11*v12)
term1= 0.5*(v11**2- v12**2- v21**2+ v22**2)
term2= v11*v22+ v12*v21

den= (term1- term2)

nsum= nsum+ num
dsum= dsum+ den

20 continue

tnum= tnum+ nsum
tden= tden+ dsum

30 continue

theta= 0.25*180./pi*atan2(tnum,tden)
if(theta .lt. 0.) then
theta= theta+ 90.
end if

write(7,*) 1,theta
```

60 continue

 stop
 end

```

**** This program calculates rotation angles for different
**** sectors.
**** The cross-component energy of each trace is
**** minimized.
**** A rotation angle is calculated for every
**** trace in each sector, and then a mean angle and
**** standard deviation is calculated and output for each
**** sector.
**** The algorithm was derived by Patricia Murtha (1988).

```

```

      real s11(400,625),s12(400,625),s21(400,625),
& s22(400,625),num,nsum,theta(5)

      parameter(pi=3.14159265)

      write(6,*) 'enter number of sectors'

      read(5,*) nsect

      write(6,*) 'enter number of traces per sector, and
& samples per trace'

      read(5,*) ntsect,nsamp

      ntrace= ntsect*nsect

      open(unit=1,file='s11.dat',form='unformatted',
& status='unknown')

      open(unit=2,file='s12.dat',form='unformatted',
& status='unknown')

      open(unit=3,file='s21.dat',form='unformatted',
& status='unknown')

      open(unit=4,file='s22.dat',form='unformatted',
& status='unknown')

      open(unit=7,file='ang.dat',status='unknown')

      do 10 i=1, ntrace

      read(1) (s11(i,j), j=1,nsamp)

      read(2) (s12(i,j), j=1,nsamp)

      read(3) (s21(i,j), j=1,nsamp)

      read(4) (s22(i,j), j=1,nsamp)

10      continue

      write(7,*) 'sector, mean theta, standard deviation'

```

```
write(7,*)
do 60 l=1,nssect
nbegin= (l-1)*ntsect
do 30 m=1,ntsect
i= m+nbegin
nsum= 0.
dsum= 0.
do 20 j=1,nsamp
v11= s11(i,j)
v12= s12(i,j)
v21= s21(i,j)
v22= s22(i,j)
num= (v11*v21- v12*v22- v21*v22+ v11*v12)
term1= 0.5*(v11**2- v12**2- v21**2+ v22**2)
term2= v11*v22+ v12*v21
den= (term1- term2)
nsum= nsum+ num
dsum= dsum+ den
20 continue
theta(m)= 0.25*180./pi*atan2(nsum,dsum)
if(theta(m) .lt. 0.) then
theta(m)= theta(m)+ 90.
end if
30 continue
call stat(theta,ntsect,tmu,stdev)
write(7,*) l,tmu,stdev
60 continue
```

```
stop
end

subroutine stat(theta,ntsect,tmu,stdev)

real theta(5)

sum= 0.

do 10 k=1,ntsect

sum= sum+ theta(k)

10 continue

tmu= sum/ntsect

sum= 0.

do 20 k=1,ntsect

sum= sum+ (theta(k)-tmu)**2

20 continue

stdev= (sum/(ntsect-1))**.5

return
end
```

```
**** This program will perform 4-component rotation
**** by a user-specified rotation angle.
```

```
      real s11(400,625),s12(400,625),s21(400,625),
& s22(400,625),r11(400,625),r12(400,625),r21(400,625),
& r22(400,625)
```

```
      parameter(pi= 3.14159265)
```

```
      write(6,*) 'enter number of traces, and samples
& per trace'
```

```
      read(5,*) ntrace,nsamp
```

```
      write(6,*) 'enter rotation angle (degrees)'
```

```
      read(5,*) ang
```

```
      open(unit=1,file='s11.dat',form='unformatted',
& status='unknown')
```

```
      open(unit=2,file='s12.dat',form='unformatted',
& status='unknown')
```

```
      open(unit=3,file='s21.dat',form='unformatted',
& status='unknown')
```

```
      open(unit=4,file='s22.dat',form='unformatted',
& status='unknown')
```

```
      open(unit=7,file='r11.dat',form='unformatted',
& status='unknown')
```

```
      open(unit=8,file='r12.dat',form='unformatted',
& status='unknown')
```

```
      open(unit=9,file='r21.dat',form='unformatted',
& status='unknown')
```

```
      open(unit=10,file='r22.dat',form='unformatted',
& status='unknown')
```

```
      do 10 i=1, ntrace
```

```
        read(1) (s11(i,j), j=1,nsamp)
```

```
        read(2) (s12(i,j), j=1,nsamp)
```

```
        read(3) (s21(i,j), j=1,nsamp)
```

```
        read(4) (s22(i,j), j=1,nsamp)
```

```
10      continue
```

```
ang= ang*pi/180.
cang= cos(ang)
sang= sin(ang)
t1= cang**2
t2= sang**2
t3= cang*sang

call rot(s11,s12,s21,s22,ntrace,nsamp,
& r11,r12,r21,r22,t1,t2,t3)

do 20 i=1,ntrace

write(7) (r11(i,j), j=1,nsamp)
write(8) (r12(i,j), j=1,nsamp)
write(9) (r21(i,j), j=1,nsamp)
write(10) (r22(i,j), j=1,nsamp)

20 continue

stop
end

subroutine rot(a11,a12,a21,a22,ntrace,nsamp,
& b11,b12,b21,b22,csq,ssq,cs)

real a11(400,625),a12(400,625),a21(400,625),
& a22(400,625),b11(400,625),b12(400,625),
& b21(400,625),b22(400,625)

do 20 i= 1,ntrace

do 10 j= 1,nsamp

s11= a11(i,j)
s12= a12(i,j)
s21= a21(i,j)
s22= a22(i,j)

b11(i,j)= s11*csq+s21*cs+s12*cs+s22*ssq
b22(i,j)= s11*ssq-s21*cs-s12*cs+s22*csq
```

```
b12(i,j)= -s11*cs-s21*ssq+s12*csq+s22*cs
```

```
b21(i,j)= -s11*cs+s21*csq-s12*ssq+s22*cs
```

```
10     continue
```

```
20     continue
```

```
return
```

```
end
```

```

**** This program performs 4-component rotation
**** for all 90 possible rotation angles.
**** For each sector and each rotation angle it
**** calculates the ratio of the total
**** principal component energy to the total
**** cross-component energy.
**** In addition, it calculates the deflection
**** of the energy ratio curves, where the
**** deflection is measured as the ratio of the
**** maximum value of the energy ratio curve to
**** the minimum value of the curve.

```

```

      real s11(400,625),s12(400,625),s21(400,625),
& s22(400,625),d11(30,625),d12(30,625),d21(30,625),
& d22(30,625),rd11(30,625),rd12(30,625),rd21(30,625),
& rd22(30,625),t1(90),t2(90),t3(90),ratio(90),
& theta(80),sharp(80)

```

```

      parameter(pi= 3.14159265)

```

```

      write(6,*) 'enter number of sectors'

```

```

      read(5,*) nsect

```

```

      write(6,*) 'enter number of traces per sector, and
& samples per trace'

```

```

      read(5,*) ntsect,nsamp

```

```

      ntrace= ntsect*nsect

```

```

      open(unit=1,file='s11.dat',form='unformatted',
& status='unknown')

```

```

      open(unit=2,file='s12.dat',form='unformatted',
& status='unknown')

```

```

      open(unit=3,file='s21.dat',form='unformatted',
& status='unknown')

```

```

      open(unit=4,file='s22.dat',form='unformatted',
& status='unknown')

```

```

      open(unit=7,file='ratio.dat',status='unknown')

```

```

      open(unit=8,file='sharp.dat',status='unknown')

```

```

      do 10 i=1, ntrace

```

```

        read(1) (s11(i,j), j=1,nsamp)

```

```

        read(2) (s12(i,j), j=1,nsamp)

```

```
read(3) (s21(i,j), j=1,nsamp)
read(4) (s22(i,j), j=1,nsamp)
10  continue

do 25 i=1,90

ang= i*pi/180.
cang= cos(ang)
sang= sin(ang)
t1(i)= cang**2
t2(i)= sang**2
t3(i)= cang*sang

25  continue

do 40 l=1,nssect

nbegin= (l-1)*ntsect

do 35 m=1,ntsect

i= m+nbegin

do 33 j=1,nsamp

d11(m,j)= s11(i,j)
d12(m,j)= s12(i,j)
d21(m,j)= s21(i,j)
d22(m,j)= s22(i,j)

33  continue

35  continue

write(7,*) 'sector ',l

write(7,*)

do 38 k=1,90

call rot(d11,d12,d21,d22,ntsect,nsamp,
& rd11,rd12,rd21,rd22,t1(k),t2(k),t3(k))

call rat(rd11,rd12,rd21,rd22,ratio(k),ntsect,nsamp)

38  continue
```

```

      call defl(ratio,sharp(1),theta(1))

      n=0

      write(7,*) n,ratio(90)

      do 39 n=1,90

      write(7,*) n,ratio(n)

39      continue

      write(7,*)

40      continue

      write(8,*) 'sector, rotation angle, max/min'

      write(8,*)

      do 50 i=1,nsect

      write(8,*) i,theta(i),sharp(i)

50      continue

      stop
      end

      subroutine rot(d11,d12,d21,d22,ntsect,nsamp,
& rd11,rd12,rd21,rd22,csq,ssq,cs)

      real d11(30,625),d12(30,625),d21(30,625),
& d22(30,625),rd11(30,625),rd12(30,625),
& rd21(30,625),rd22(30,625)

      do 20 i= 1,ntsect

      do 10 j= 1,nsamp

      s11= d11(i,j)

      s12= d12(i,j)

      s21= d21(i,j)

      s22= d22(i,j)

      rd11(i,j)= s11*csq+s21*cs+s12*cs+s22*ssq

      rd22(i,j)= s11*ssq-s21*cs-s12*cs+s22*csq

      rd12(i,j)= -s11*cs-s21*ssq+s12*csq+s22*cs

```

```
rd21(i,j)= -s11*cs+s21*csq-s12*ssq+s22*cs
10  continue
20  continue

return
end

subroutine rat(a,b,c,d,er,ntsect,nsamp)
real a(30,625),b(30,625),c(30,625),d(30,625)

prin= 0.
cross= 0.

do 40 i=1,ntsect
psum= 0.
csum= 0.

do 30 j=1,nsamp
pterm= a(i,j)**2+ d(i,j)**2
psum= psum+ pterm
cterm= b(i,j)**2+ c(i,j)**2
csum= csum+ cterm
30  continue

prin= prin+ psum
cross= cross+ csum
40  continue

er= prin/cross

return
end

subroutine defl(ratio,steep,ang)
real ratio(90),min,max

ang= 1.

min= ratio(1)
```

```
max= ratio(1)
do 20 i=2,90
if(ratio(i) .gt. max) then
    max= ratio(i)
    ang= i
end if
if(ratio(i) .lt. min) then
    min= ratio(i)
end if
20 continue
steep= max/min
return
end
```

```
**** This program calculates the rotation angle
**** errors, for a given S1 polarization
**** direction, for different
**** x- to y-component source displacement
**** amplitude ratios.
**** The amplitude ratios used are integers
**** varying from 1 to 10.
```

```
real num, left

parameter (pi= 3.14159265)

write(6,*) 'enter S1 direction (degrees)'

read(5,*) ang

theta= ang*pi/180.

cos2= (cos(theta))**2

sin2= (sin(theta))**2

sincos= sin(theta)*cos(theta)

i= 1

error= 0.

write(1,*) i, error

do 10 i= 2, 10

xxf= cos2*i

xys= sin2*i

yyf= sin2

yys= cos2

xyf= sincos*i

xys= -sincos*i

yxf= sincos

yxs= -sincos

term1= (xxf-yyf)*(yxf+xyf)

term2= (xys-yys)*(yxs+xys)

num= term1+ term2
```

```
left= 0.5*(xxf**2+yyf**2-xyf**2-yxf**2)
right= xxf*yyf+ xyf*yxf
term1= left- right
left= 0.5*(xxs**2+yys**2-xys**2-yxs**2)
right= xxs*yys+ xys*yxs
term2= left- right
den= term1+ term2
ptheta= 14.32394488*atan2(num,den)
if (ptheta .lt. 0.) then
    ptheta= ptheta+ 90.
end if
error= abs(ang- ptheta)
write(1,*) i, error
10 continue
stop
end
```